INVESTIGATIONS INTO QUASI-TWO-DIMENSIONAL ACTIVE MATTER SYSTEMS USING COLLOIDAL PROBES

by

David P. Rivas

A dissertation submitted to The Johns Hopkins University in conformity with the requirements for the degree of Doctor of Philosophy.

Baltimore, Maryland

December, 2020

Abstract

Active matter research is a relatively new and exciting field of study that often merges concepts from non-equilibrium soft matter physics and biology. Active matter systems are composed of individual units that consume energy locally to produce collective phenomena that can lead to rich and complex behavior. Examples of experimentally studied active matter systems include bacteria suspensions, artificial swimmers, and collections of biopolymers driven by molecular motors. Investigations of these systems have the potential to provide important insights into the workings of these biologically relevant systems, as well as to serve as model systems for studies of non-equilibrium physics. In particular, many active systems of biological importance exist in viscoelastic environments, yet little work so far has studied the interplay of activity and viscoelasticity in these systems. The work in this thesis focuses on investigating the dynamical and material properties of two quasi-two-dimensional interfacial viscoelastic active matter systems, a biofilm-forming bacterial suspension and a microtubule-based "active nematic" film, which is an out-of-equilibrium liquid crystal. In chapters 3 and 4, results are presented in which magnetic micro-sized

ABSTRACT

colloidal rods and disks are employed that couple hydrodynamically to the active nematic film. This coupling enabled the investigation of the dynamical and material properties of the film, and also the local manipulation and ordering of the otherwise chaotic flows. In addition, sufficiently large applied hydrodynamic stresses produced by rotating the disks drove the formation of +1 charge topological vortices through the merger of two +1/2 defects. Chapter 5 presents a comprehensive experimental study of the dynamics and rheology of an oil-water interface during biofilm formation by the bacteria strain Pseudomonas Aeruginosa, PA14. The evolution of the system is studied during this transition using both passive and active microrheology in parallel with differential-dynamic-microscopy to characterize the motion of the bacteria at the interface. The passive microrheology demonstrates a dependence on size of the colloidal probes at late ages that is significantly greater than that expected in a homogeneous system in equilibrium, indicating either length-scale-dependent rheology of the biofilm or widely different effects of the bacteria activity on the motion of the spheres.

This work was conducted under the supervision of Prof. Robert L. Leheny and Prof. Daniel H. Reich.

Primary Reader: Professor Robert L. Leheny

Secondary Reader: Professor Daniel H. Reich

Acknowledgments

I have been very fortunate to have had exceptional mentors, both during my time as an undergraduate and as a PhD student, who have shown intentive interest in my development as a scientist. I would like to thank Professor Leheny for his mentorship and guidance. His patience, constructive advice, and enthusiasm were of monumental value. I would also like to thank Professor Reich for his guidance and unfailing willingness to provide beneficial advice. I am also grateful to Professor Serra and Professor Reich for their generous lending of laboratory equipment and general assistance. Additionally, I am thankful for the contributions and enthusiastic and insightful discussions provided by our collaborator, Tyler Shendruk.

I have worked with many other talented people who have shown generous willingness to provide their time and assistance. Of instrumental value, the assistance, generous help, and time provided by former graduate students Kui Chen and Prasenjit Bose is greatly appreciated. The experimental techniques they imparted to me was of great value. I am also grateful for the help and camaraderie of other graduate students in the department, including Dan Allan, Yu Shi, Wai Ting Hung (Carol), and Alvin

ACKNOWLEDGMENTS

Modin, as well as undergraduates in the Leheny group, including Bilyana Tzolova and Olivia Gebhart. I would also like to thank former postdoctoral researchers, Ramona Mhanna and Tagbo Niepa for their assistance. In addition, I greatly enjoyed working with the talented high school students Nathan Hedgecock and Robert Henry who I would also like to thank for their contributions to this work.

Contents

List of Figures

Chapter 1

Introduction

1.1 Active Matter

1.1.1 What is Active Matter?

A central topic of this thesis dissertation is the physics of active matter. Active matter can generally be categorized as any system whose constituent particles' mobility arises due to the consumption of stored or local external energy sources [20, 80, 88, 106]. Due to the perpetual injection of energy into the system, active matter is inherently out of thermodynamic equilibrium. In active matter systems, the energy cascades from small scales up to the macroscale. This energy flow is unlike some other out-of-equilibrium systems where, for example, the energy is introduced at the boundaries and then propagates through the system, such as in a fluid that

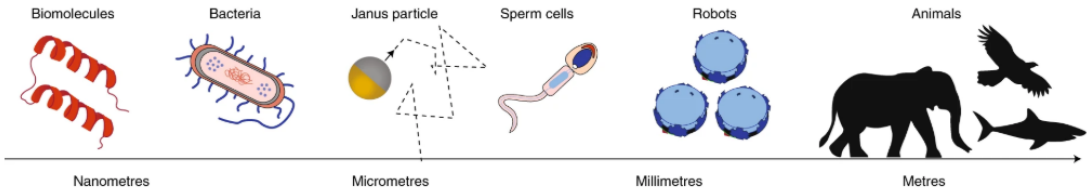

Figure 1.1: Active matter systems range from microscopic molecules to macroscopic herds of animals. Figure from [19].

is under shear stress or that is heated. Experimental examples of active matter include bacteria suspensions [28], self-propelled Janus colloids [99], vibrated granular rods [86], collections of cytoskeletal filaments [117], and interacting robots [46]. Much of the research in active matter involves understanding the unique properties that emerge as a result of the self-propelled motion of the constituent particles. The range of topics researched on such systems includes collective motion [28, 130], transport and mixing [138], phase separation [48], rheology and material properties [116], and non-equilibrium statistical mechanical properties [168].

Due to their out-of-equilibrium nature, active matter systems can exhibit intriguing behavior not seen in their equilibrium counterparts. Examples include motility induced phase separation [15], giant number fluctuations [80, 104], reduced or negative viscosity [76, 128], and production of net positive work [55, 127, 154]. The unique properties of active matter have led to ideas of applying them for functions that are not possible in equilibrium systems.

The earliest work in active matter involved modeling collective motion of animal flocks, such as flocks of starlings. A seminal paper in 1995 presented a theoretical

model for collective motion of individual self-propelled particles, known now as the Vicsek model, which tracks each particle's position and updates its velocity vector based on that of its neighbors while including random noise [153]. The model predicts collective motion of the particles for sufficient density and sufficiently low noise. Continuum models were later developed to describe the collective motion in active matter systems [106]. Such continuum theoretical models typically draw from passive liquid crystal theories while incorporating additional elements to account for the active stresses in the system [73]. Experimental systems demonstrating collective motion of self-propelled particles include artificial swimmers, bacteria swarms, and robots [120].

From this early work on collective motion in biological systems, much of the continued research in active matter has maintained a similar common thread; namely one that involves creating or studying systems that could shed light on those found in nature, but often could also serve to address fundamental questions in physics. Many active matter system are composed of living organisms or biologically derived components, therefore investigating these systems often has biological relevance. For example, systems of active biofilaments can produce dynamics reminiscent of cytoplasmic streaming and, therefore, studies of these systems may provide insight into the mechanics of this cellular process while also addressing questions of non-equilibrium dynamics. Another example is studies of suspensions of bacteria that can provide insight into the dynamical behavior of these organisms that addresses questions in

microbiology and the statistical physics of systems far from equilibrium.

Some active matter systems can serve as simple models to better understand how the statistical mechanical and thermodynamic laws that govern equilibrium systems can be applied to non-equilibrium systems [136]. For example, the enhanced motion of bacterial suspensions can sometimes be thought of as being analogous to an equilibrium system at a larger effective temperature. This will be discussed in more detail in chapter 5. Therefore, active matter systems are useful for better understanding non-equilibrium phenomena, such as determining if there exist well defined fundamental thermodynamic parameters like temperature and pressure. There is also a question as to whether there exists an equation of state in active matter systems [45].

This dissertation presents experimental studies of two important examples of active matter. This first is active nematic films. As described below, nematic liquid crystals are fluids characterized by preferred alignment of the long axes of the anisotropic liquid-crystal molecules. This orientational order can be described by a vector field called the director $\vec{n}(\vec{r})$. In active nematics, the rod-like constituents are driven into a state of perpetual flow due to an internal energy source. Just as conventional liquid crystals have provided productive insights into key problems in condensed matter physics near equilibrium – such as the connections among collective behavior, symmetry breaking, excitations, and topological defects – active nematics are promising models for exploring such issues in out-of-equilibrium contexts. A major challenge in the study of active nematics, which is addressed in this dissertation, is how to couple

to the nematic externally to interrogate its properties and potentially manipulate its behavior.

The second active-matter system studied in this dissertation is bacterial suspensions that form biofilms at oil-water interfaces. Biofilms dominate microbial life. Indeed, it has been estimated that 99% of all bacteria on earth reside within biofilms. From the perspective of bacteria suspensions as active matter, biofilm formation presents the interesting opportunity to investigate an active system within a medium that is developing viscoelastic properties. The common thread linking the work reported in this dissertation on active nematic films and bacterial biofilms is the application of colloidal particles, and magnetically actuated colloidal particles in particular, to probe and manipulate the active systems.

1.1.2 "Wet" and "Dry" Active Matter

Theoretical models of active matter systems are often classified based on whether hydrodynamics need to be considered or, instead, if frictional damping dominates. The former case is known as "wet" active matter while the latter is classified as "dry" active matter. Examples of active matter systems where hydrodynamics can be ignored include cells crawling on a substrate or robots moving on a solid surface. Whereas, a suspension of self-propelled colloidal particles is an example where hydrodynamics plays an important role in the dynamics of the system. Both the active nematic films and biofilm-forming bacterial suspensions can be considered examples

of wet active matter.

1.1.3 Active Force Dipoles

The majority of experimental active matter systems that have been studied consist of individual dipolar units. Each active particle acts as a force dipole that exerts no net force on the medium [106]. The force dipoles can be classified as either positive or negative, corresponding to extensile or contractile stresses on the medium, respectively. Fig. 1.2 displays the direction of fluid flow created by each type of force dipole. The distinguishing characteristics of these stresses derive from the direction of the forces relative to the polar axis of the particle. For example, a bacteria such as E. coli swim by pushing on the fluid behind and in front of them. These types of swimmers are known as a "pushers" and they exert an extensile stress dipole on the fluid. An organism such as Chlamydomonas reinhardtii that makes breast-stroke-like motion with its flagella moves by pulling the fluid in front of it toward itself, which also results in the fluid behind it being pulled toward the cell. This type of swimmer is known as a "puller". This motion creates a force dipole that is contractile. The flow field created by force dipoles decays as $1/r^2$, unlike the $1/r$ scaling created by a force monopole, such as a sphere driven through a fluid by an external force [64]. The flow field created by force dipoles results in torques generated on neighboring dipoles that can lead to a preference towards alignment or anti-alignment (a relative orientation of 90 degrees) in the extensile and contractile cases, respectively [64].

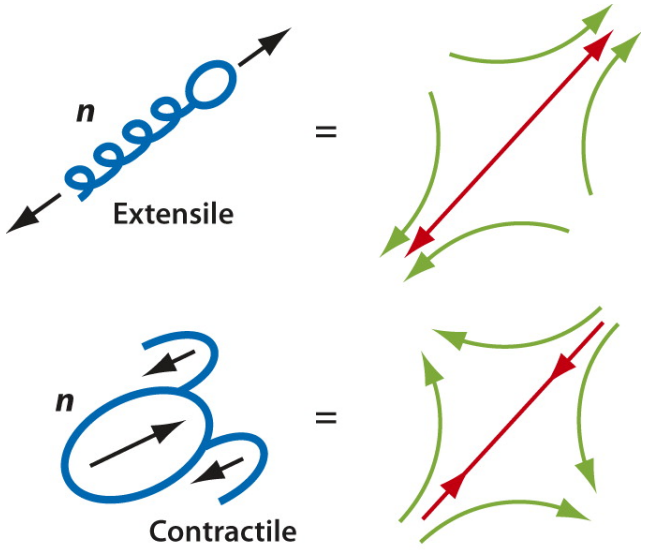

Figure 1.2: Extensile and contractile flow fields created by pusher-type (top) and puller-type (bottom) swimmers. Here $\boldsymbol{n}$ represents the primary axis of the swimmer. Figure taken from [105].

1.2 Liquid Crystals

As mentioned above, a major subject of this dissertation is active nematic films. Here, this section provides background into the liquid-crystal physics relevant to these studies. A liquid crystal is a phase of matter with order intermediate between a crystalline solid and an isotropic liquid. In a crystalline phase, the constituent particles of the material are ordered spatially in a lattice, thus breaking translational symmetry. In contrast, in a liquid no long-range positional or translational order exists. There are many intermediate phases of a liquid crystal in which symmetry is broken along certain spatial or orientational directions, known as mesophases. These liquid crystal phases are less ordered than a crystalline solid while also being more ordered than an isotropic liquid. One such mesophase, the nematic phase, occurs in liquid

crystals and is associated with the breaking of rotational symmetry. In materials that form nematic phases, the constituent subunits of the liquid crystal, known as the nematogens, are elongated and preferentially align about their long axis. The direction of this alignment is called the director and is denoted by the unit vector, $\hat{\mathbf{n}}$. Figure 1.3 displays the phase sequence of a system of rod-like particles from crystalline, to nematic, to isotropic liquid at low, intermediate, and high temperatures, respectively. Such phase behavior as a function of temperature is associated with thermotropic liquid crystals. As an example, the molecular structure of the molecule 4-Cyano-4'-pentylbiphenyl (5CB), which is a thermotropic liquid crystal, is shown in Fig. 1.4. Other liquid-crystalline substances, known as lyotropic liquid crystals, undergo phase transitions as a function of both concentration and temperature. An example of a mesophase with greater order is the Smectic-A phase, in which the elongated molecules, in addition to being aligned nematically, are spatially ordered into layers along the direction normal to the director.

1.2.1 The Order Parameter

To describe the orientational order in the nematic phase, a second-rank, symmetric and traceless tensor is defined, $\hat{Q}_{i,j}(\mathbf{r}) = \langle \hat{\mathbf{e}}_i \hat{\mathbf{e}}_j \rangle - \frac{1}{3}\delta_{i,j}$, where $\hat{\mathbf{e}}$ is the unit vector associated with each particle specifying its orientation, the subscripts refer to the components along each Cartesian coordinate, and the brackets represent an average over molecules in a local region around the position $\mathbf{r}$. Note that in the isotropic

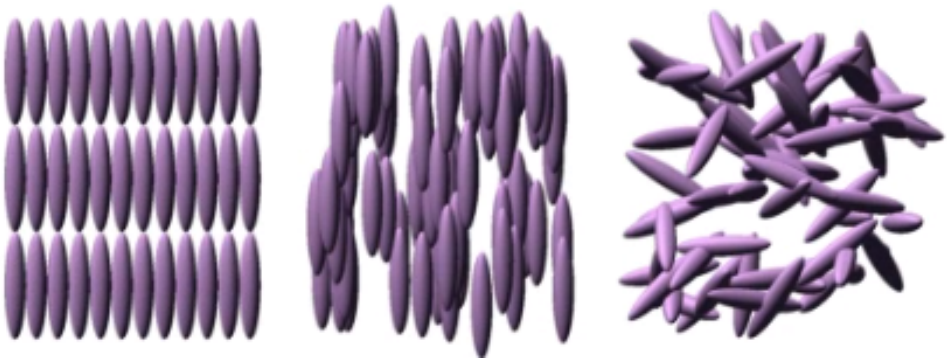

Figure 1.3: An example of the translational and orientational order of a thermotropic liquid crystal from low to high temperature (from left to right). The constituent elongated molecules contain both translational and orientational order at low temperature, the crystal phase, but only orientational order at intermediate temperatures, the nematic liquid-crystal phase. At higher temperatures, the molecules are orientated and distributed isotropically. Image from [96].

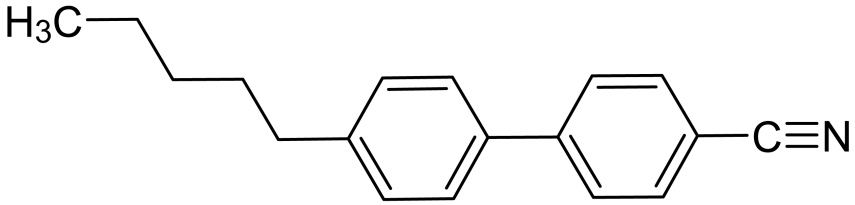

Figure 1.4: The molecular structure of the elongated molecule 5CB, a thermotropic liquid crystal.

phase, the components of $\hat{Q}$ are zero. One can define the director $\hat{\mathbf{n}}$ as the unit vector parallel to the eigenvector of $\hat{Q}$ with the largest eigenvalue. The eigenvalue is the scalar order parameter and is equal to $S = \frac{1}{2}(3\langle cos^2(\theta)\rangle - 1)$, where θ is the angle between each nematogen and the director. The scalar order parameter characterizes the degree of local alignment of the molecules. If the system is isotropic then $S = 0$, whereas for perfect alignment, $S = 1$.

1.2.2 Theoretical Models

The first-order transition from the isotropic to the nematic phase in liquid crystals has been described successfully, at least partially, by theoretical models. One of these models, relevant for lyotropic systems, is the Onsager hard-rod model which considers the free energy change of the system that results from differences in entropy in the aligned versus unaligned state. In this model, the nematogens are rod shaped and cannot overlap. The principle behind the transition lies in the fact that the excluded volume of particle centers-of-mass is reduced when the rods align, therefore increasing the positional entropy of the system. At sufficiently large density, this positional entropy increase outweighs the orientational entropy decrease caused by the orientational ordering of the rods. Although providing a clear and insightful explanation for the isotropic to nematic transition, the model is unable to explain thermotropic liquid crystal phase transitions.

Another model, formulated by Maier and Saupe, considers the contribution of the inter-molecular interaction energy to the free energy. In this theory, the interaction is modeled as dipolar and provides an energetically favorable alignment of the molecules. Therefore, at sufficiently low temperature, the molecules tend to align due to this interaction energy, whereas at higher temperatures entropy becomes the dominant factor and leads to disorder. This theory provided a significant quantitative improvement with experiments, while also capturing the isotropic to nematic phase transition's temperature dependence.

Aside from these molecular-based theories of the nematic phase transition in liquid crystals, a purely phenomenological theory, the Landau-de-Gennes approach, has proved quite successful. In this theory, the free energy is written as an expansion of the order parameter while considering the symmetries of the system. Because the microscopic details are absent, this mean-field theory is applicable to a broad range of systems.

1.2.3 The Frank-Oseen Free Energy Density

Distortions of a nematic liquid crystal from its equilibrium state result in an increase in the energy of the system. In order to determine this energy cost, one can express the strains in the system in terms of spatial derivatives of the director. Assuming a slowly varying director field on the scale of molecular distances, and invoking symmetries of the nematic, an estimate of the distortion free energy density can be found [40]. This elastic distortion energy cost is called the Frank-Oseen elastic free energy density, and it consists of four terms: splay, twist, bend, and saddle-splay. Since the saddle-splay term is a total derivative, an integral of the term over volume can be rewritten as a surface term through Stokes' theorem, and hence it is often neglected. Considering the three remaining fundamental distortions, the Frank-Oseen energy density is

$$\mathcal{F}_d = \frac{1}{2}K_1(\nabla \cdot \hat{\mathbf{n}})^2 + \frac{1}{2}K_2(\hat{\mathbf{n}} \cdot \nabla \times \hat{\mathbf{n}})^2 + \frac{1}{2}K_3(\hat{\mathbf{n}} \times \nabla \times \hat{\mathbf{n}})^2 \tag{1.1}$$

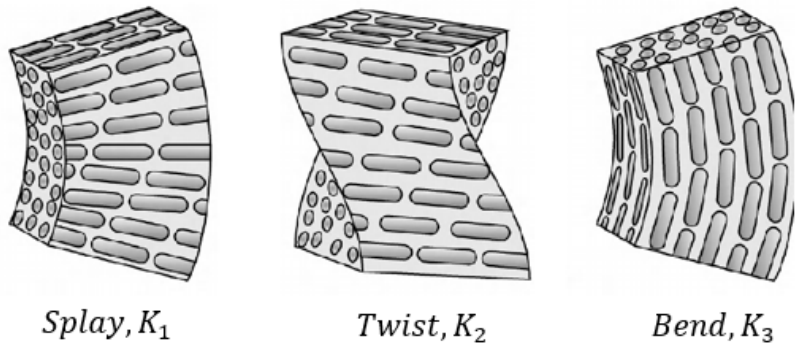

Figure 1.5: The three types of distortion associated with the three Frank elastic energy and their associated elastic constants, splay (K_1), twist (K_2), and bend (K_3). Adapted from [42].

The coefficients – K_1, K_2, and K_3 of the splay, twist, and bend terms, respectively – are the Frank constants and are material properties of the specific nematic system. Figure 1.5 shows an sketch of the distortions associated with each of these constants.

In a two-dimensional nematic, like the active nematic films investigated in the dissertation, only splay and bend distortions are present. For simplicity, an approximation is often made that the three constants are equal. This reduces the free energy density to

$$\mathcal{F}_d = \frac{1}{2}K((\nabla \cdot \hat{\mathbf{n}})^2 + (\nabla \times \hat{\mathbf{n}})^2) \tag{1.2}$$

In a two-dimensional system, one can write $\hat{\mathbf{n}}$ in terms of its orientation with respect to the x-axis, θ, so that $\hat{\mathbf{n}} = (\cos\theta, \sin\theta)$. In this case, the free energy further simplifies to,

$$\mathcal{F}_d = \frac{1}{2}K(\nabla\theta)^2 \tag{1.3}$$

1.2.4 Topological Defects

Topological defects exist in many systems across diverse areas of physics, including quantum systems, cosmology, particle physics, and hard and soft condensed matter. They play a critical role in the behavior and properties of many systems. Topological defects in a nematic liquid crystal are singular regions where the director field is ill-defined. Topological defects can be classified according to their winding number, or "charge". An example of defects of three different values of charge is shown in Fig. 1.6. The orientation of the local director is indicated by the solid lines. The angle of the director with respect to the x-axis around a defect can be written in the idealized form, $\theta = m\phi + \phi_0$, where θ is the angle of the director with respect to the x-axis, ϕ is the polar angle, also measured from the x-axis, m is the winding number, or charge, of the defect, and ϕ_0 is a phase angle that is equal to the orientation of the director at $\phi = 0$. (For all the examples in Fig. 1.6, $\phi_0 = 0$.) Topological charge is analogous to electric charge. For example, in electrostatics, the net charge within a volume of space can be inferred from the flux of the electric field through any enclosing surface. Similarly, by measuring the change of the director along a bounding surface enclosing topological defects, the net enclosed topological charge can be found. As a simple example, imagine drawing a circle around the -1/2 defect in the right-most panel of

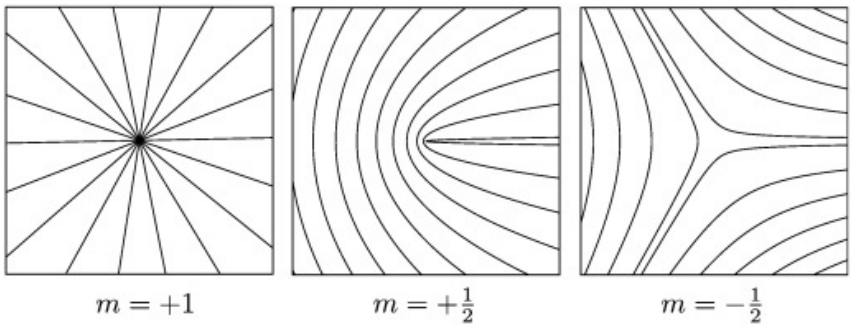

Figure 1.6: Schematics of topological defects with charge +1, +1/2, and -1/2 from left to right. The solid lines indicate the orientation of the local director, from [5].

Fig. 1.6 and measuring how the orientation of the director changes as one goes around the circle. Doing this, one finds that the angle rotates by π. Thus, the charge of the defect is given by this change in angle divided by 2π, while the sign depends upon whether the director changed in a clockwise or anti-clockwise fashion. For the -1/2 defect, going around the circle clockwise one measures an anti-clockwise rotation of the director. Since the two rotation directions are opposite, the defect is said to have a negative charge.

Since the director field in regions around defects is distorted, the defects have an associated elastic free energy cost. Plugging in $\theta = m\phi + \phi_0$ into Eq. (1.3) and integrating over space gives the energy cost of the distortions. Near the singularity, the elastic energy density becomes very large. Therefore, over a small region known as the defect core, it is energetically favorable for the nematic to convert to the isotropic phase rather than to support the great amount of distortion energy cost. Therefore, within the core, the order parameter S is zero, and the material has effectively melted.

Thus, the core size sets a lower limit on the integral over the elastic distortion, and the result is an elastic energy cost equal to $\pi K m^2 ln(R/r_c)$, where R is the size of the distorted regions (approximately the defect-defect spacing), and r_c is the radius of the defect core. Note that this energy scales quadratically with the charge of the defect. The total energy cost of a defect is the sum of this distortion energy cost and the energy cost of melting the core. The distortions around defects further lead to an interaction energy between them such that like-charged defects repel whereas opposite-sign defects attract [140].

The energy cost associated with the distortions created by the existence of defects in a liquid crystal results in the equilibrium state being one in which the number of defects is minimized. However, the topology of the system or boundary constraints may force the system to maintain a total non-zero topological charge. For example, a liquid crystal placed on the surface of a sphere must have a net topological charge of +2. This can be easily imagined by considering lines of latitude on a sphere with each of the two poles hosting a +1 defect. Although this is an energetically favorable state, other arrangements or the existence of many more defects are topologically allowed so long as net charge is equal to +2. For instance, the two +1 defects on the surface of a sphere can split to form four +1/2 defects. This topological property is known as the Euler characteristic and is invariant no matter how the shape is bent. It is +2 for a sphere, +1 for a two dimensional disk, and 0 for a torus.

1.2.5 Active Nematics

Unlike their passive counterparts, active nematics are liquid crystalline systems that are driven out-of-equilibrium through the continual local consumption of an internal energy source. Energy is consumed locally, rather than being pumped into the system externally from, for example, electric or magnetic fields. Active nematics are perpetually flowing, and these non-equilibrium flows spontaneously generate and annihilate pairs of defects, destroying long-range order and creating a chaotic state that is referred to as active turbulence [143]. Examples of active nematics include epithelial monolayers [119], bacterial biofilms [164], and vibrated granular rods [87].

Active nematics can also be engineered using biopolymer systems [60, 117]. One realization of a biopolymer-based active nematic, which is the subject of work in this dissertation, is a quasi-2D system composed of microtubule bundles that are driven by kinesin molecular motors at an oil-water interface [117]. Microtubules are rod-like polymers consisting of tubulin dimer proteins. As part of the cell cytoskeleton, they play a critical role in the function of cells by acting as a track, or substrate, for the transportation of cargo by molecular motors as well as functioning in cell mitosis. They are up to tens of micrometers in length and roughly 23 nm in diameter. The tubulin dimers consist of α and β subunits that connect end-to-end. The α tubulin proteins are exposed on one end of the microtubule, known as the negative end, while the opposite end, where the β tubulin proteins are exposed, is known as the positive end. Therefore, the microtubule is a polar filament. Cargo transport

on microtubules takes place via kinesin and dynein molecular motors which "walk" along the microtubules in a certain direction while carrying cargo. Kinesin molecular motors move from the negative end of the microtubule towards the positive end, whereas the direction of motion is reversed for dynein. In an analogous fashion to kinesin and microtubules, myosin molecular motors translate along polymeric actin filaments. Myosin and actin function in processes such as muscle contraction and cell crawling. Kinesin, dynein, and myosin molecular motors are all powered via the hydrolysis of Adenosine Tri-Phosphate (ATP). Therefore, the concentration of ATP in solution sets the activity level of the biopolymer-based active nematics [68].

In the microtubule-based active nematic films, a pair of kinesin molecular motors are attached to one another, allowing them to walk along two microtubules at the same time. Depending upon the polar arrangement of the adjacent microtubules, these pairs of kinesin motors either walk along the two microtubules in the same direction, or there is a conflict in the preferred direction of propagation. In this latter case, the motors produce a force on the two microtubules that acts to slide the two microtubles along one another. Fig. 1.7a provides an illustration of the process. Another key component in the experimental system is poly(ethylene glycol) (PEG) polymers that produce an attractive depletion force between the microtubules, resulting in them forming bundles of aligned filaments. This leads to an overall enhancement of the kinesin/microtubule contacts, and hence the activity. The microtubules are stabilized from polymerizing and depolymerizing by GMPCPP, leading to a length

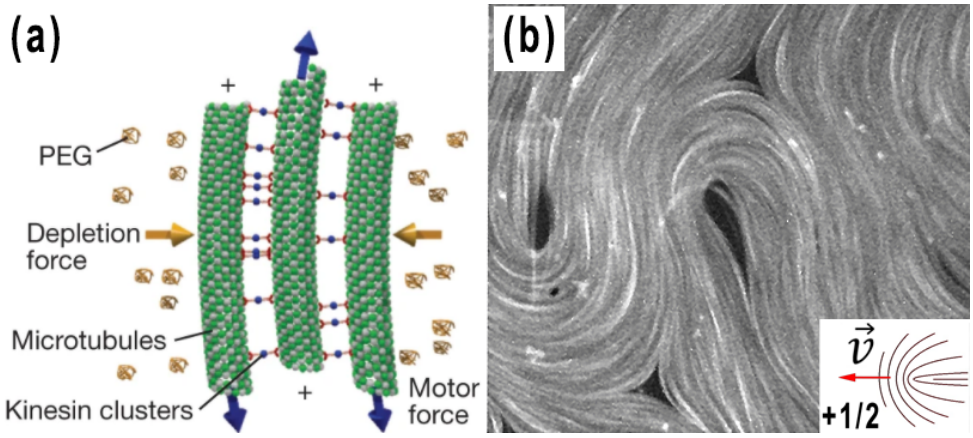

Figure 1.7: (a) In a microtubule-based active nematic system, kinesin molecular motors create sliding forces along adjacent microbule filaments which leads to extensional flows and drives active turbulance (taken from [117]). (b) An image of a quasi-2D layer of an active nematic showing the local nematic alignement of the microtubule bundles and the proliferation of positive and negative charge 1/2 defects.

of approximately 2 μm. An ATP regeneration system which converts ADP back into ATP is used in the system, therefore maintaining a fairly consistent level of ATP on the order of hours. Activity is essential in producing the nematic order, as otherwise the kinesins form cross-links with the microtubules, creating an isotropic gel.

The sliding of the microtubular bundles along one another creates extensional flows that results in the self-propulsion of charge +1/2 defects. As shown in the inset of Fig. 1.7, a +1/2 defect is propelled in the direction of its "head", while the symmetry of a -1/2 defect results in a zero net propulsion. Therefore, the +1/2 defects act as the drivers of the system dynamics, while the -1/2 defects behave as passive particles that are pushed around by hydrodynamic and elastic stresses present in the film. As an example of the defect dynamics, Fig. 1.8 displays the measured mean-squared-displacement of +1/2 and -1/2 defects within an active nematic film. As expected,

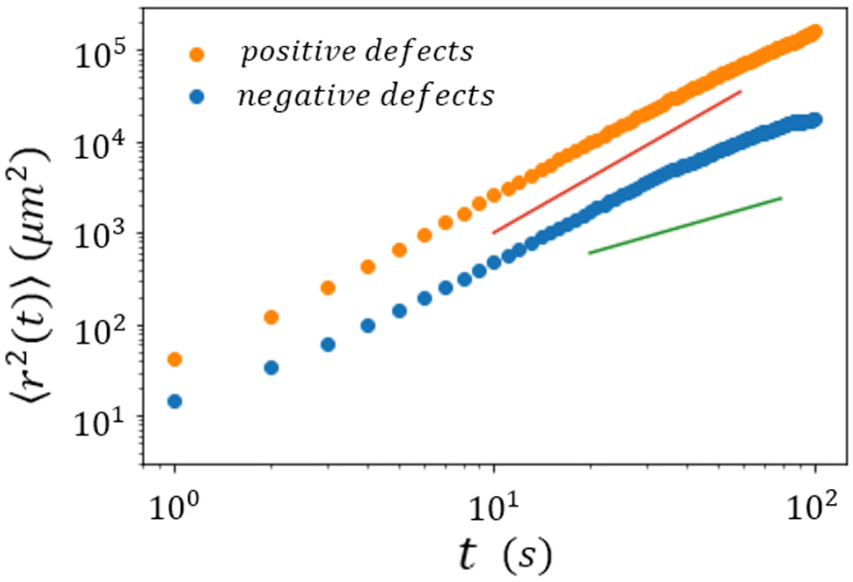

Figure 1.8: The mean-squared displacement of +1/2 defects (orange) and -1/2 defects (blue) as a function of lag time. The red solid line indicates a power-law slope of 2 and the green solid line indicates linear scaling.

the positive defects have greater mobility due to their self-propelled motion. As can also be seen, their mean-squared-displacement is nearly ballistic on the time scale of the measurement, *i.e.* with a slope of 2. The -1/2 defects also display ballistic motion at short lag times, but cross over to diffusive motion, *i.e.* with a slope of 1, at larger lag times.

Experimental work has investigated the effects on the properties of the film due to varying the elasticity or activity. For example, the ratio of actin and microtubule filaments in the active nematic layer were tuned to produce varying degrees of bend elasticity [167]. The shape of +1/2 defects was shown to depend on the ratio of bend to splay elastic constants. Systems with a relatively larger bend energy cost have more V-shaped +1/2 defects, while systems with a relatively lower bend energy cost

have +1/2 defects with a more U-shape. The bend instability of an extensile active nematic film results in an effective decrease in the free energy cost to bend distortions, which was indicated by the change of the morphology of +1/2 defects from V to more U shaped as the level of activity was increased [60].

The stresses within the active nematic film create characteristic flow fields around +1/2 and -1/2 defects, as shown in Fig. 1.9, which displays simulated fluid velocity and normalized vorticity, as indicated by the black arrows and color map, respectively. The white lines correspond to the director field. The vorticity is defined as the curl of the velocity field, $\boldsymbol{\omega} = \nabla \times \mathbf{u}$ and characterizes the local circulation of the flow. For example, for solid-body rotation, a negative vorticity corresponds to clockwise flow and positive vorticity to counter-clockwise flow, with the magnitude of the vorticity equal to one-half of the rotation rate. For circular flows that fall off as $1/r$, the vorticity is zero. Counter-clockwise flows that fall off slower than $1/r$ have positive vorticity, while for flows that fall off with distance faster than this, the sign of the vorticity reverses. In active nematic films, the flows on the left side of a +1/2 defect have positive vorticity and those on the right side have negative vorticity, as indicated in Fig. 1.9.

Theoretical models used to describe active nematic dynamics typically use the constitutive equations for passive nematics, such as those of Beris-Edwards nemato-hydrodynamics, but include an additional contribution to the stress on the fluid from the activity. This "active stress" has the form $-\zeta\hat{Q}$, where ζ is a measure of the

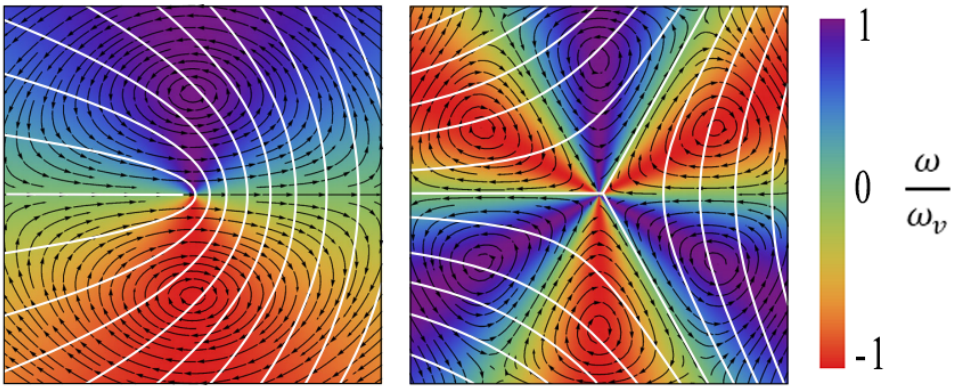

Figure 1.9: Normalized vorticity (color map) and fluid flow field (black arrows) in the frame of reference of a +1/2 defect (left panel) and a -1/2 defect (right panel) in an active nematic film. The white lines indicate the director field. Figure adapted from [47].

strength of the activity and $\hat{Q}$ is the tensor order parameter. A positive value of ζ represents extensile active forces, while a negative value corresponds to a contractile system.

1.3 Rheology

Rheology is the study of flow. It involves studying and modeling how a material responds to applied stress, or what stresses the material imposes under an applied deformation. Put in another way, rheology is a study of how a material stores or dissipates mechanical energy [157]. In the following sections, some of the important concepts of rheology measurements, particularly those that are used in the work of this dissertation, will be discussed.

1.3.1 Stress and Strain

The stress on a material can be represented as a tensor, $\hat{\sigma}$, with nine components, $\sigma_{i,j}$, where i specifies the direction of the applied force and j the surface upon which it acts. The diagonal elements give the normal stresses on the surface of the material, while the off-diagonal elements provide the shear stresses. The strain tensor, $\hat{\epsilon}$, is also composed of nine components, $\epsilon_{i,j} = \frac{1}{2}(\partial_j u_i + \partial_i u_j)$, where $\partial_j u_i$ represents the derivative of the displacement in the direction x_i with respect to the coordinate x_j.

The simplest types of materials are those with a linear relation between stress and strain, or stress and strain rate. The former describes the response of a linear elastic solid material while the latter characterizes a Newtonian viscous fluid. As an example, if a shear stress, τ, is applied to a material, as shown in Fig. 1.10, then a linear elastic material will deform until the material imposes an elastic restoring stress that balances the applied shear stress. Specifically, $\tau = G\gamma$, where G is the elastic shear modulus and γ is the shear strain, which is twice the normal strain ϵ and is equal to $\frac{du}{dy}$. Many elastic materials contain a region of linear response at stresses below a critical value of stress called the yield stress, but transition into a non-linear regime at larger stresses due to plastic deformation. Newtonian fluids flow when subject to an applied shear stress such that the strain rate is linear in the stress, $\tau = \eta\frac{d\gamma}{dt}$, where η is the shear viscosity. Materials whose response to stress involves both elastic and viscous components are known as viscoelastic materials. These will be discussed in more detail in section 1.3.3. Examples of non-Newtonian fluids include

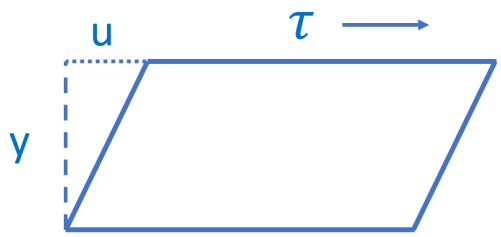

Figure 1.10: Sketch of the shear stress, τ, on a material undergoing a deformation, u, as a function of height, y.

shear-thinning and shear-thickening materials, whose viscosity decreases or increases with shear rate, respectively.

1.3.2 Fluid Dynamics

Fluid flow can be modeled by considering the forces acting on an infinitesimal element of the fluid and applying Newton's second law. For an incompressible Newtonian fluid, this leads to the Navier-Stokes equation,

$$\rho\left(\frac{\partial \mathbf{u}}{\partial t} + (\mathbf{u}\cdot\nabla)\mathbf{u}\right) = \eta\nabla^2\mathbf{u} - \nabla p \tag{1.4}$$

where $\mathbf{u}$ is the fluid velocity, ρ is the mass density, and p is the pressure. The left-hand-side of the equation involves inertial terms, which are negligibly small when the dimensionless quantity known as the Reynolds number is very small. The Reynolds numberRe is a measure of the ratio of inertial to viscous forces and is given by

$$Re = \frac{\rho u L}{\eta} \tag{1.5}$$

where L is the characteristic length scale of the system. For example, for a sphere translating in a fluid, L is approximately the sphere's radius. Since much of the work presented in this thesis involves micrometer-scale colloids or bacteria that are moving in water at velocities of no more than 20 μm/s, $Re \sim 10^{-5}$, and therefore inertial effects can safely be ignored. Fluid flow in this limit is known as Stoke's flow. In the case in which the pressure is zero, the Navier-Stokes equation reduces to Laplace's equation,

$$\nabla^2 \mathbf{u} = 0 \tag{1.6}$$

As an example relevant to some of the work in this dissertation, for a disk rotating in two dimensions (2D), Eq. (1.6) becomes $\frac{1}{r}\frac{d}{dr}(\frac{1}{r}\frac{du}{dr}) = 0$, where u is the azimuthal velocity of the fluid as a function of distance from the center of the disk. If one takes the velocity to be zero at infinity and ωR at the edge of the disk, where ω is the rotational rate of the disk and R is its radius, then the solution is $u(r) = \frac{\omega R^2}{r}$. Taking the fluid velocity at the surface of an object to be equal to the velocity of the surface is known as the no-slip boundary condition, and is a widely used approximation for viscous fluids. It is interesting to compare the $1/r$ dependence of the velocity around a rotating disk in 2D with some other examples. For instance, a rotating sphere in three dimensions creates a flow field that falls off as $1/r^2$. The velocity field falls off as $1/r$ around a sphere translating in a three dimensional fluid. Interestingly, a disk translating in 2D fluid does not yield a solution, a result known as the Stokes

paradox [10]. If the 2D fluid is an interfacial film, this unphysical result can be resolved by including viscous dissipation in the surrounding bulk fluids, in which case the flow field falls off logarithmically with distance [115].

A similar analysis provides the deformation of an 2D elastic film in mechanical equilibrium subject to shear strain imposed by the disk. Assuming the same no-slip condition at the disk edge and zero displacement at infinity, and given that the disk rotates to an angle $\Delta\theta$, yields the solution $u(r) = \frac{\Delta\theta R^2}{r}$, where here $u(r)$ is the azimuthal displacement of the elastic sheet as a function of distance. The similarity of the results is due to the similar dependence of the stress to the strain, with only a time derivative distinguishing the linear elastic case from that of the Newtonian fluid.

1.3.3 Viscoelastic Materials

Materials that have both a restoring, elastic, component, as well as a dissipative, viscous behavior are known as viscoelastic materials. Two simple models of viscoelastic materials are the Maxwell and the Kelvin-Voigt models. These consider the material's response to be that of a simple mechanical system composed of an arrangement of springs and dashpots. These two models are shown in Fig. 1.11, where G and η are the spring constants and viscosities of the springs and dashpots, respectively. The Maxwell model consists of a spring and dashpot in series whereas in a Kelvin-Viogt system, the spring and dashpot are in parallel. Therefore, the strain is recovered in a Kelvin-Voigt system whereas it is partially lost in a Maxwell system. Because of

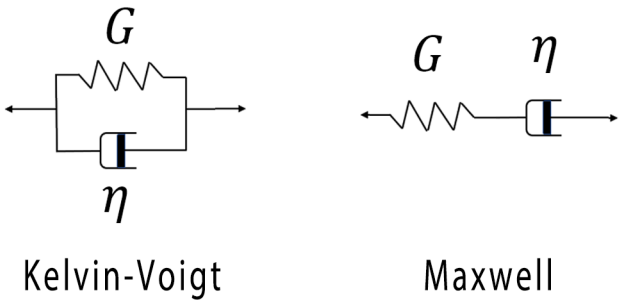

Figure 1.11: Sketch of the Kelvin-Voigt and Maxwell viscoelastic models.

these distinctions, a Maxwell viscoelastic material is known as a viscoelastic liquid whereas a Kelvin-Voigt viscoelastic material is known as a viscoelastic solid.

An example of the creep-compliance, which is proportional to the MSD via equation (2.2), of these two materials is shown in Fig. 1.12 as well as their relaxation once the stress is removed. For the Maxwell fluid, the strain initially increases instantaneously due to the compression of the spring element, followed by a linear response due to the dashpot. Upon removal of the stress, the spring goes back to its equilibrium state while the dashpot remains unchanged. In the Kelvin-Voigt system, an applied stress results in an exponentially asymptotic strain followed by an exponential decay upon removal of the stress. The mean-squared displacement of a particle is unbounded in a Maxwell viscoelastic material but, via equation (2.2) saturates to a value equal to $\langle r^2(t=\infty)\rangle = \frac{dk_BT}{3\pi RG}$ for a spherical particle in a Kelvin-Voigt viscoelastic solid.

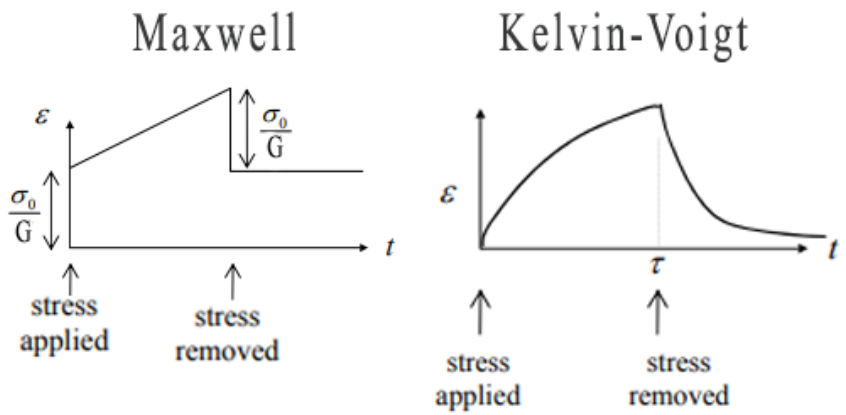

Figure 1.12: The strain response of a Maxwell Fluid (left) and a Kelvin-Voigt Fluid (right) to a constant stress followed by relaxation with the stress removed. Adapted from [57].

1.3.4 Langevin Equation

Colloidal spheres in a fluid undergo the so called "Brownian motion" due to collisions with molecules which causes the spheres to move stochastically. The Langevin equation describes the sphere's motion in terms of the random forces, $\mathbf{f}(t)$, which originates from the molecular collisions,

$$m\dot{\mathbf{v}} = \zeta m\mathbf{v} + \mathbf{f}(t) \tag{1.7}$$

where m is the mass of the colloid, $\mathbf{v}$ is its velocity, and ζ is the drag coefficient. Due to its stochastic nature, the Langevin equation is often most useful when considering average values of quantities in which the random force acts many times. For example, taking the time average of both sides of Eq. (1.7), and assuming that the mean force is zero, shows that the average velocity decays exponentially with a time constant

of $\tau = \zeta^{-1}$. For a typical 1 μm sphere in water, $\tau \approx 10^{-7}s$, therefore the average velocity of the sphere decays to zero effectively instantaneously compared to typical observational time scales of video microscopy measurements, such as those conducted in this thesis.

Further, by employing the equipartition theorem, i.e. $m\langle \mathbf{v}^2 \rangle = k_B T$, and taking the random forces to be decorrelated in time, $\langle \mathbf{f}(t) \cdot \mathbf{f}(t+t') \rangle = \lambda \delta(t-t')$, it is possible to solve for the mean-squared-displacement of the particle as a function of time,

$$\langle \mathbf{r}^2(t) \rangle = 2dD \left(t - \tau \left(1 - e^{-t/\tau} \right) \right) \tag{1.8}$$

where d is the number of dimension and D is the diffusion constant which is equal to $D = \frac{k_B T}{\zeta m}$. One also finds that $\lambda = 2\zeta m k_B T$, thus relating the fluctuating forces to the drag force on the particle. Because τ is typically much smaller than the time scale of the measurement, for $t \gg \tau$ one recovers the result for simple linear diffusion, $\langle \mathbf{r}^2(t) \rangle = 2dDt$.

1.4 Biofilms

Suspensions of motile bacteria are a well studied model of an active-matter system. A common practice of bacteria in suspension is to form biofilms, which are materials consisting of biopolymers, nucleic acids, polysaccharides, lipids, proteins, and other extracellular polymeric substances (EPS). Microorganisms form these films

by adhering to a surface or adsorbing to an interface and then secreting the EPS, thereby encasing themselves in the matrix. The biofilm matrix is a heterogeneous cross-linked gel that protects the enclosed organisms from external threats such as desiccation, shear forces, and antibiotics [38, 101]. From the perspective of active matter, biofilm-forming bacteria hence provide an interesting perspective of an active system existing within a medium with evolving viscoelastic properties [9]. While the majority of studies of bacteria as active matter has focused on swimmers in viscous liquids, cell motion within viscoelastic media is salient to a number of important problems beyond biofilms including bacteria swimming in mucus, cells interacting with extracellular matrix, cancer cell migration in healthy tissue, and growth of bacterial colonies in food products [102]. Chapter 5 of this dissertation describes an experimental study to characterize the evolution in dynamical and mechanical properties of an interface of a bacteria suspension with oil during biofilm formation at the interface.

Beyond serving as a model for exploring the physics of active matter, bacterial biofilms have mechanical properties that are themselves directly important since they dictate the responses of the film, such as resistance to fracture or cohesive failure as well as spreading and the formation of streamers, under externally applied shear stresses like those imposed by fluid flow [12, 101]. The precise properties of a particular film depend upon the bacterial strain as well as the environmental and growth conditions [9, 14, 122, 148]. Despite this variability, it has been found that biofilms generally behave as viscoelastic fluids with very long characteristic response times

of around 20 minutes and upwards, hence allowing the films to adapt to fluid shear stress and unload internal stored elastic energy [122].

The robustness of biofilms to mechanical, chemical, and other threats, also makes them difficult to remove in undesirable settings. Biofilms can be problematic in industrial and medical environments, for example, where their presence can lead to damage to equipment or infections of hospital patients. It has been estimated that the majority of treated human infections are due to biofilms [43]. Therefore, these concerns makes understanding the material properties of biofilms of significant relevance, which is one of the goals of the research presented in Chapter 5 of this thesis.

Investigations of the material properties of biofilms have involved rheology, microrheology, atomic-force-microscopy (AFM), shear flow, and other techniques [14]. For example, measurements of the adhesion of biofilms to surfaces was conducted using a centrifuge that imposed a force on the film in a direction normal to the surface [92]. By varying the rotation rate, the force required to detach the biofilm from the substrate was determined. AFM has been be used not only to image the biofilm surface but also gain information about adhesion forces by measuring force on the tip upon extraction after indentation of the film [8, 35]. The rheological properties of biofilms can be examined with the use of a standard rheometer. However, placing the biofilm within a rheometer disturbs the film and, for biofilms on solid surfaces, changes its adhesion to the substrate. Microrheological measurements are therefore

advantageous in this respect, but the heterogeneity of the biofilm must be considered when comparing the results to the macroscopic material properties of the film. Another method has used shear flow of fluid over a biofilm to create shear stress on the film, thus allowing for *in situ* measurements of the strain-strain response and creep [135]. However, the shear stress in such measurements is not known with precision and likely varies over the sample. In Chapter 5, the results of microrheology experiments on interfacial biofilms are presented in which "active" and "passive" microrheological methods are compared in order to gain a firmer understanding of the information provided by each methods. In addition, results employing differential dynamic microscopy (DDM) to study the dynamics of the bacteria within the film, provide a more comprehensive picture of the dynamical and mechanical properties of the interface during biofilm formation. To our knowledge, these studies are the first to apply DDM to these systems.

Chapter 2

Experimental Techniques

2.1 Microrheology

Microrheological experiments involve either actuating a small colloid with an externally applied force or tracking its passive motion caused by thermal fluctuations within a material to obtain information about the material's mechanical properties. These two types of microrheological methods are called active microrheology and passive microrhelogy, respectively. Because of the colloidal probes' small size, they are typically imaged using microscopy techniques, but other techniques such as dynamic light scattering have also been employed in microrheology. Microrheology possesses benefits over conventional macro-scale rheology in cases where the samples are inherently too small for conventional rheometry tools, where it is of interest to probe material properties on the micrometer length scales of the probe, or where the fragility

of the sample requires minimal disturbance. Microrheology also avoids potential issues with conventional rheometry, such as slip of the material on the measurement tool, that lead to misleading results. If the material contains heterogeneities or texture on the length scale of the probe or larger, then microrheological and macro-scale rheological measurements will likely give different results, in which case the methods can provide complementary information.

Active microrheology is typically performed using magnetic or electric field actuation, while passive microrheology involves imaging colloids and measuring their motion with particle-tracking analysis. This motion can then be related to the material properties of the system, as is discussed in the next section.

2.1.1 Fluctuation Dissipation Relations

The principles of passive microrheology are based on extensions of the pioneering work of Einstein, Sutherland, and Smoluchowski that revealed a connection between the dissipative processes that lead to the viscous drag on a particle and the fluctuations that cause it to undergo Brownian diffusive motion. The Einstein relation states that for a particle in a fluid in thermal equilibrium,

$$D = \mu k_B T \tag{2.1}$$

where D is the diffusion coefficient of the particle, μ is its mobility, k_B is the Boltzmann constant, and T is the temperature. The diffusion constant is defined via

the mean-squared-displacement $\langle \Delta r^2 \rangle$ of the particle undergoing Brownian motion, $\langle \Delta r^2(t) \rangle = 2dDt$, where d is the number of spatial dimensions, and t is the lag time over which the displacement is measured. The mobility μ, which is the inverse of the drag coefficient, is defined as the ratio of the force on the particle to its velocity under Stokes flow, $F_{drag} = -\frac{1}{\mu}v$. For a sphere, $\mu = (6\pi\eta R)^{-1}$, where R is the sphere radius, and η is the fluid velocity. Inserting this value for μ into Eq. (2.1 gives the famous Stokes Einstein Relation, which is an example of a fluctuation-dissipation relation that generally relates the thermal fluctuations of a system to the dissipation caused by linear response to a perturbation.

The basic idea of passive microrheology, as developed in the 1990's by Mason, Weitz, Schmidt and others [77, 84], is that such applications of the fluctuation-dissipation theorem can be extended to the positional (and rotational) motion of particles within viscoelastic materials in thermodynamic equilibrium. In this case, one obtains so-called Generalized Stokes Einstein Relations that for example relate the creep compliance of the material to the mean-squared-displacement of a spherical colloid within the material,

$$J(t) = \frac{3\pi R}{dk_B T}\langle r^2(t) \rangle \tag{2.2}$$

where the creep-compliance $J(t)$ is the normalized strain of the material at a constant stress.

2.1.2 Colloidal Drag Forces

As mentioned above, the expressions for the drag coefficients on a colloid are used to relate the motion of the colloid to material properties, such as viscosity or elasticity, in microrheological experiments. While the drag coefficient of a sphere in 3D, $\mu^{-1} = 6\pi\eta R$, is widely known, this dissertation deals with situations that are less familiar; therefore, we briefly review some key relevant results. Much of the work in the dissertation concerns quasi-2D interfacial films. The drag on an sphere translating in a 2D layer is more complicated than in 3D due to the lack of a solution of the Stokes equation in 2D. However, estimates of the drag have been made by considering the contributions of the surrounding bulk fluids, which results in,

$$F_{drag,2D} = \frac{4\pi\eta v h}{\ln(Bo) - \gamma} \tag{2.3}$$

where h is the thickness of the 2D layer, and $\gamma = 0.5772$ is the Euler constant. Bo is the Boussinesq number [115], which indicates the relative importance of 2D viscous forces to bulk viscous forces and is given by,

$$Bo = \frac{\eta_{2D}}{R(\eta_1 + \eta_2)} \tag{2.4}$$

where η_{2D} is the 2D viscosity of the layer, R is the sphere radius, and η_1 and η_2 are the viscosities of the bulk fluid phases above and below the layer. When $Bo \gg 1$, the interfacial viscous forces dominate over the bulk dissipation. Equation 2.3 is applicable only in this regime.

As described in Chapters 4 and 5, the drag on a cylindrical, rod-shaped colloid

figures prominently in many results in this dissertation. The drag force on a rod translating in a 3D viscous fluid along its long and short axes was found by Tirado and de la Torre to be,

$$F_{drag,\parallel} = \frac{2\pi L\eta v}{\ln(\frac{L}{d}) - 0.20} \tag{2.5}$$

$$F_{drag,\perp} = \frac{4\pi L\eta v}{\ln(\frac{L}{d}) + 0.84} \tag{2.6}$$

where L is the length of the rod and d is its diameter [147]. This result was obtained by calculated the drag due to a collection of spherical particles that together form the shape of a cylinder. In a similar fashion, the rotational drag torque on a rod rotating at an angular frequency ω in a 3D viscous fluid was approximated as,

$$\Gamma_{drag} = \frac{\pi L^3 \eta \omega}{3ln(L/d) - 2} \tag{2.7}$$

[95]. In addition, the rotational drag torque on a rod rotating in a 2D layer can be approximated as,

$$\Gamma_{drag,2D} = 1.48\eta L^2 \omega \tag{2.8}$$

which is valid for at large values of Bo [70]. In a similar vein as the derivation of the previous two equations, this result was found by determining the drag on many thin disks that form the shape of a rod.

2.2 Ferromagnetic Colloid Fabrication

A major component of the research presented in this dissertation involves particle-tracking and microrheology studies employing custom, microscale magnetic particles. The methods to fabricate these particles are described here.

2.2.1 Ferromagnetic Disk Fabrication

Nickel ferromagnetic disks were fabricated using photolithography techniques. Glass slides were cleaned by sonicating in 1% Hellmanex, followed by acetone, followed by isoproponal alcohol (IPA). The sonication time was approximately 10-15 minutes. The slides were rinsed well with DI water after each sonication process was complete. A sacrificial layer of PMMA (Poly methyl methacrylate) was spin-coated at 1000 RPM for 45 seconds onto the glass slides. This is followed by a hard bake at 180° C for 1 minute and 15 seconds.

Initially, nickel was deposited onto the slides via thermal evaporation. However, we found that subsequent etching was unable to remove a thin layer of material that inter-connected the disks. We found that acetone was also ineffective at removing the material and that increasing the developing times of the photoresist did not prove successful. Therefore, we concluded that the presence of the material was not due to the incomplete removal of the nickel or of the resist. Instead, we associate the material with a composite of nickel and PMMA created during the thermal evapo-

ration process, leading to a connecting layer that is impervious to both acid etching and dissolving in organic solvents. Therefore, to circumvent this issue, we employed sputtering rather than thermal evaporation. The nickel was applied to a thickness of approximately 300 nm and was then covered with a layer of positive photoresist, Microposit S1813, by spin coating at 2000 rpm for 1 minute and soft baking at 115° C for 1 minute. The photoresist was then exposed to UV light for 4.5 seconds. A photomask was used to selectively shield circular regions of the resist, which results in these regions becoming insoluble to the developer following the UV exposure.

We developed the slides in Microposit 351 developer for 15 seconds then rinsed the slides with DI water. The slides were then etched in a 1:2 solution of nitric acid to DI water which removes the nickel layer except in those regions coated by the resist. Once the slides became transparent due to the removal of the nickel layer, which typically occurs after about 4 minutes, the slides were removed from the etchant and rinsed with DI water. The glass slides were then cut into smaller pieces which were placed in glass vials containing acetone. The acetone dissolved the remaining resist as well as the PMMA sacrificial layer, thus freeing the disks from the glass substrate. The glass was removed from the vial using tweezers, and the acetone was poured out while holding the disks in place using a permanent magnet. IPA was then added and removed approximately three to four times to rinse. Disks that were stored in IPA kept their shape over time, whereas disks that were stored in DI water tended to curl over time, folding partially into a taco-shape.

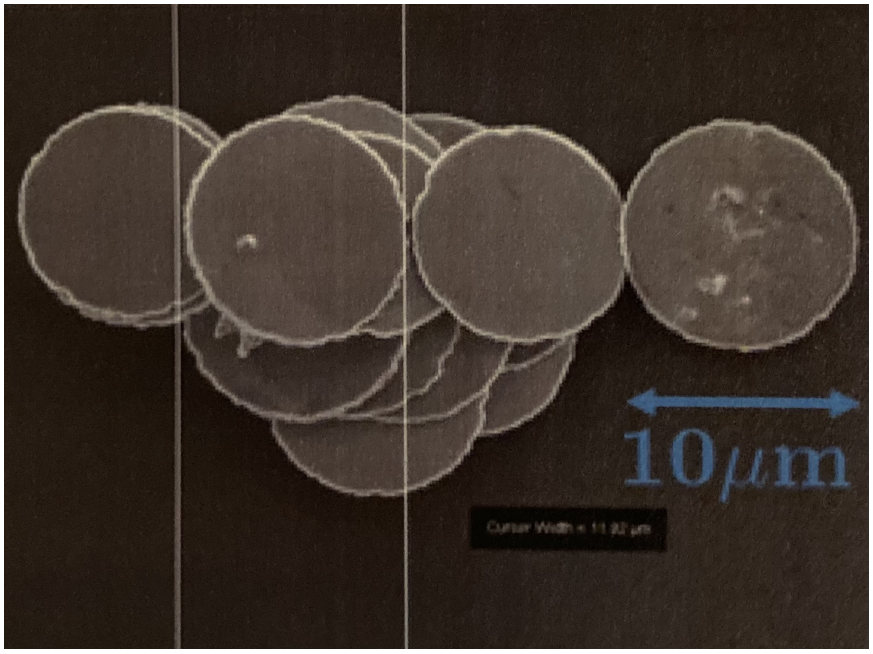

Figure 2.1: Scanning electron microscopy image of ferromagnetic nickel disks. Image acquired from [110].

Photolithography masks were made by first creating a photomask design in Autocad software. Mylar masks were made by a company called Fineline Imaging. Aside from solid disk shapes, several other designs were also constructed in order to allow for tracking of the disk's angle of rotation. For example, one of these designs consisted of a 40 μm diameter disk with two 8 μm diameter holes separated from the edges and from each other by 8 μm. A similar process to that described above was used to transfer the mylar photomask onto a chrome mask. The chrome mask provides more consistent results and therefore is preferred over the mylar mask. The transfer process was repeated until a satisfactory result was obtained in which the features and edges of the disks were well defined. An example scanning electron microscopy image of ferromagnetic disks that were made using the above procedures is shown in

Fig. 2.1.

2.2.2 Ferromagnetic Rod Fabrication

Ferromagnetic nickel colloidal rods, that are typically 370 nm in diameter and about 30μm in length, were fabricated using electrodeposition techniques. The wires were made by electrodepositing nickel onto a porous alumina membrane. The membranes (Whatman Inc), were 47 mm in diameter and had a nominal pore size of 0.2 μm. The pores narrowed on one end while being larger and more uniform on the other. A thin ($\sim 400nm$) layer of copper was sputter coated onto the side of the membrane with the narrower pore size and this acted as a conducting surface for the deposition. The copper layer was kept thin to promote easy removal of the layer from the ends of the wires after the deposition. The membrane was placed copper-side down on a conducting copper plate, which was first cleaned well with sand paper and DI water to improve its conductivity at the surface. A teflon container with a cylindrical cavity was placed atop the membrane and a rubber o-ring was used to seal the bottom of the container. The container was clamped onto the copper plate, holding the plate, membrane, and container firmly together. The teflon container was filled with DI water to test for leaking. The water was poured out and a copper electrolyte solution consisting of 125 g/L $CuSO_4 \cdot 5H_2O$ (copper sulfate pentahydrate), 30 g/L H_3BO_3 (Boric Acid), and 20 g/L NaCl in DI water was added. A platinum electrode was placed inside the copper solution after cleaning the end with a torch.

The voltage between the copper substrate and the platinum electrode was controlled by a potentiostat. A reference electrode was also used to ensure accurate readings of the potential. A potential difference of -0.2 V was used for the copper deposition. Approximately 1-1.5 Coulombs results in 1 μm of copper thickness. The copper layer was deposited to a total thickness of 2-5 μm, thus filling the narrower regions of the pores leaving the region of larger, more uniform pore diameter to be deposited with nickel. The copper solution was poured out and the container was rinsed several times with DI water. Then, a nickel electrolyte solution consisting of 514 g/L $Ni(SO_3NH_2)$, 20 g/L $NiCl_2 \cdot 6H_2O$, and 20 g/L H_3BO_3 in DI water was added. A potential difference of -1 V was set between the copper plate and the platinum counter-electrode. Approximately 3 Coulombs of nickel results in 1 μm thickness on the membrane. Once the desired amount was deposited, the electrolyte was poured out and the cylindrical cavity was rinsed well with DI water. The section of the membrane onto which the nickel and copper was deposited was cut away from the rest of the membrane using a razor. A copper etchant of 33.3 g/L $CuCl_2$ in 1 M HCl was used to remove the copper layer. This was done by rubbing the surface of the membrane with a cotton q-tip soaked in the etchant. Once the template turns a dark color, the copper had been removed and the wires were then freed from the remaining alumina membrane by soaking overnight in 0.5 M KOH at 60° C. The KOH solution was then sonicated for 10 minutes, and the solution was poured out while holding the wires in place using a magnet. New KOH was added and the wires are again soaked for several hours.

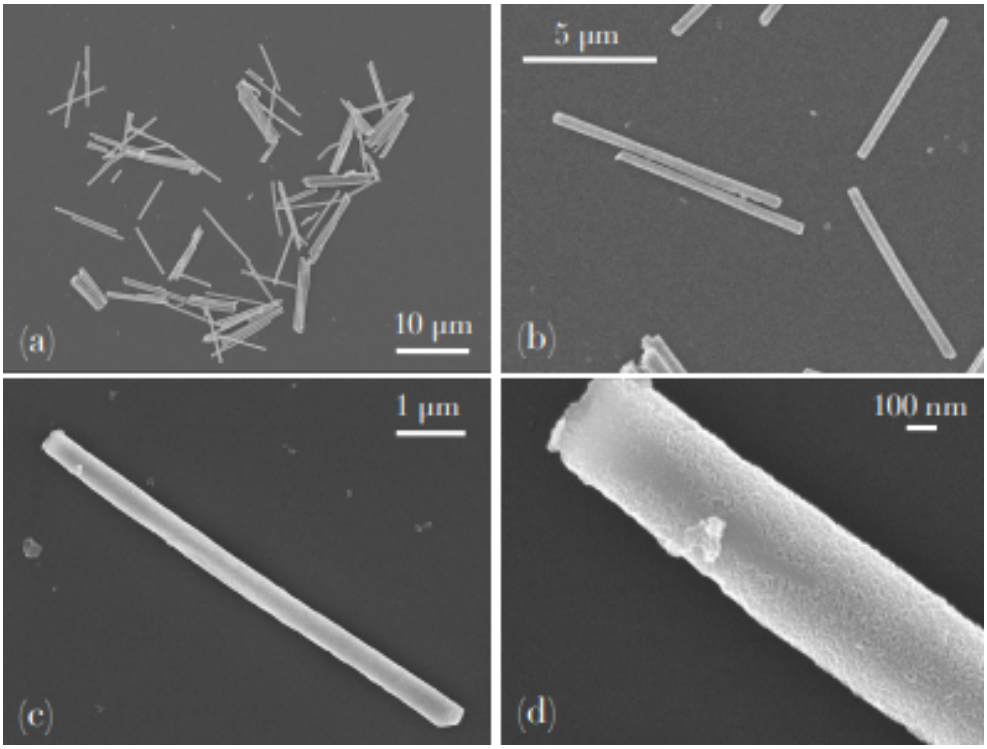

Figure 2.2: Scanning electron microscopy images of ferromagnetic nickel rods. Image acquired from [36].

Finally, the solution was sonicated again, followed by rinsing with DI water, acetone, and then storing in isopropanol. An example of SEM images of nanowires that were made using the techniques described above is shown in Fig. 2.2.

2.3 Magnetic Tweezers

Magnetic torques were applied to colloidal disks and rods during video microscopy measurements using an array of magnetic solenoids, as shown in Fig. 2.3. The solenoids contain soft magnetic cores and are mounted on the stage of an inverted optical microscope . Two sets of four solenoids positioned symmetrically above and

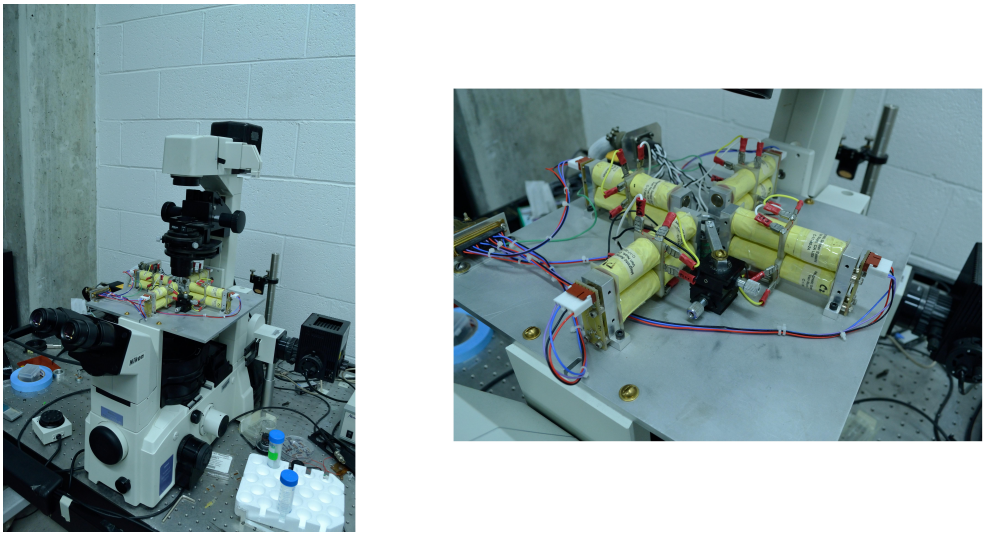

Figure 2.3: Photos of the array of magnetic solenoids mounted on the microscope, allowing for *in-situ* application of magnetic torques on colloids in fluids during imaging.

below the sample position allowed for application of fields in arbitrary direction up to 200 Gauss. The feedback-regulated current to the coils was computer controlled using custom Labview software, as described elsewhere [66].

2.4 Image Analysis

2.4.1 Determination of the director field in active nematics

Many of the results in this dissertation rely on accurate characterization of the time-dependent nematic director field of active nematic films from video microscopy. Prior to determining the director field in an image of an active nematic film, the image

was first processed to make the algorithm more accurate. For bightfield images, this often was done by calculating the median image intensity for a particular video, then subtracting this from each image of the video. This resulted in small artifacts being removed, such as dust, as well as larger-scale intensity variations. For both fluorescent and brightfield images, typically the image was blurred using a Gaussian kernel with a width of approximately 1 pixel. The blurring decreased the effect of noise on the image intensity gradients, and therefore tended to give more accurate results for the director.

The images were then partitioned into square regions-of-interest (ROI) that were typically approximately 20×20 μm^2, which was small enough to provide a nearly uniform director within the ROI while also being large enough to limit the effects of noise. Adjacent ROIs often are made to overlap somewhat, providing improved resolution. The orientation of the director within each ROI was determined by computing the 2×2 matrix, H with components $H_{xx} = (\partial I/\partial y)^2$, $H_{yy} = (\partial I/\partial x)^2$, $H_{xy} = H_{yx} = -(\partial I/\partial y)(\partial I_y/\partial x)$, where I is the image intensity. The orientation of the director is determined by the eigenvector of this matrix with the largest eigenvalue. An example of the director field calculated in this way is shown in Fig. 2.4.

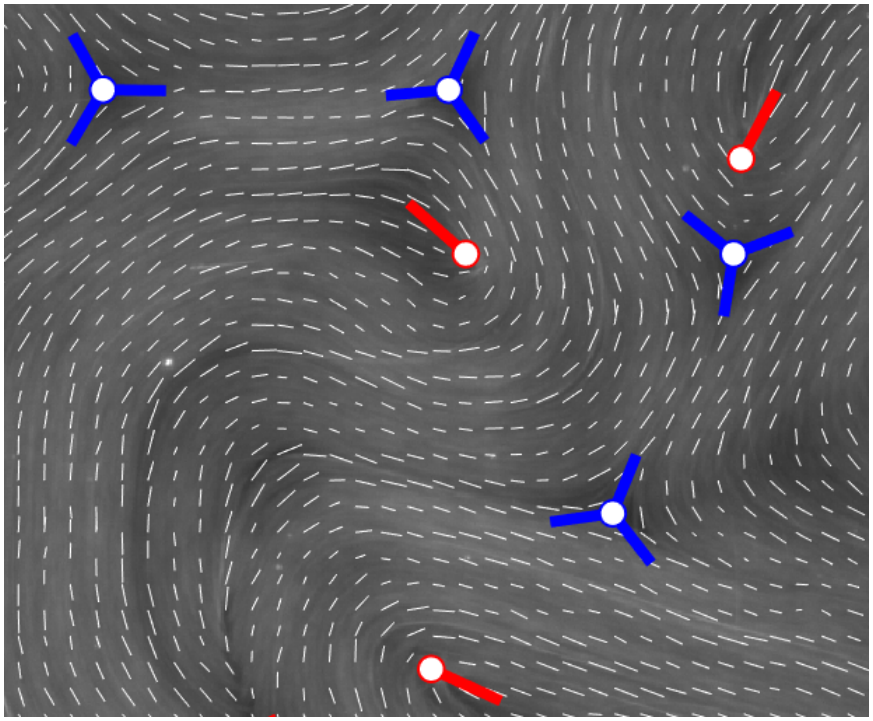

Figure 2.4: Example of a fluorescent image of an active nematic film with the director indicated by the white lines. The locations and orientations of the positive and negative defects are given by the red and blue markers, respectively.

2.4.2 Determining the Location and Orientation of Topological Defects

As described in section 1.2.4, topological defects are regions in which the director is spatially discontinuous. The presence of a defect within any enclosing boundary can be determined by calculating the change of the director's orientation in terms of the angle it makes with some axis while going around the boundary. If the net change in the angle is zero, then the region enclosed by the boundary contains no net topological charge. We employ this method to determine the existence of topological defects within square regions-of-interest in the images. For example, in Fig. 2.4, the director was calculated in a small region of the image which we will refer to as a sub-ROI. In the image shown, for example, there are 26 x 34 sub-ROIs. The change in orientation of the director in a square area enclosing a 4×4 grid of these sub-ROIs was used to determine the existence and sign of defects present within the region. This calculation is performed over all such 4×4 grids within the field of view. Because a single defect will be detected multiple times, a clustering algorithm is used to distinguish one defect from another, and the centroid of each cluster was taken as the location of the defect core.

The director field around a +1/2 defect has a polar configuration, and it is customary to denote the defect orientation by a vector that goes from the core towards the "tail". For -1/2 defects, an orientation can be assigned only up to the three-fold

symmetry of of the director around it. To identify defect orientations of both types of defects, one can introduce a polar coordinate system with the defect at the origin and define position-dependent angle ϕ as the angle between the director and the radial direction. One can then determine the directions along which $\phi = \theta$. These directions with respect to the defects in Fig. 2.4 are denoted by the red and blue lines for the +1/2 and -1/2 defects, respectively. For the +1/2 defects, these lines coincide with the vector directions customarily assigned to the defects.

Tracking of defects was performed in Python using the link function of the code "trackpy" [3], which takes the coordinates of the defect cores and determines their trajectories based on an algorithm developed by Crocker and Grier [23].

2.4.3 Tracking the position and orientation of rods at an interface

To track the position of micrometer-sized nickel rods at an interface, the center of the rods was found after performing a thresholding to each image, which zeroed all but the darkest pixels in the image. Then, the largest connected region of non-zero pixels was found, and all other non-zero pixels were zeroed. The center of mass (COM) of the image was then calculated and identified with the center of the rod. The grey-scale intensity of the image was used as an effective mass for the computation of the COM.

The orientations of the rods in each image were determined by computing the inertia tensor of the rod after performing a thresholding, as described elsewhere [4]. The eigenvector with the largest eigenvalue of the inertial tensor was computed, and its direction was identified as the long axis of the rod. This method was used in passive rotational diffusion measurement of rods when precise determination of the rod's angle was required, as well as active rotational measurements whenever the rod could be adequately separated from the background. For rods at bacterial interfaces in which the background had a varying intensity that made it difficult for the thresholding to cleanly separate the rod from other dark areas of the image, a different algorithm was used that was less sensitive to varying background intensity. The algorithm used the Hough voting procedure to determine the line through the image that contains the darkest pixels. This procedure used the Python code HoughLines from the OpenCV library and gives the orientation of the rod within a small range of angles, which was typically sufficient. However, the result was made further precise by binning of pixels in the image and finding the bins which contained a certain threshold number of dark pixels. The bins were then filtered to keep approximately only those that are along the rod, then these remaining bin centers were fit to a line, and the slope of the line was used to determine the rod's orientation. This second method of determining the orientation of a rod was employed when the inertial method described above failed, which sometimes occurred, for example, for rods within a biofilm.

2.4.4 Tracking of Colloidal Spheres

Colloidal spheres of diameter from 1-15 μm were imaged then identified and tracked using Python code called trackpy [3] developed by Daniel Allan, a former graduate student in the Leheny/Reich group. The code first identifies the center of the spheres using a thresholding followed by a weighted averaging of the pixel intensity to find the centroid of each sphere, thus, depending on the amount of noise in the image, locating the center of the sphere to potentially sub-pixel accuracy. The coordinates of the spheres are then linked from frame to frame using trackpy's linking algorithm, which is based on an algorithm developed by Crocker and Grier [23]. The trajectories of the spheres were then used to determine their mean-squared displacement, Van Hove correlation, or other quantities of interest that were used to determine the properties of the environment, as described in Chapter 5.

2.5 Statistical Properties of the MSD

An important quantity in passive microrheology is the mean-squared displacement (MSD), which is often a used to characterize the dynamics of an object or to determine rheological properties of the environment in which the object moves. It is therefore of substantial importance to understand the statistical properties of MSD in order, for example, to quantify properly the uncertainty in a measurement that is determined from the MSD or to optimally determine the MSD value itself. The next two sections

briefly summarize the relevant statistical properties of the MSD calculated for the simple case of diffusive motion in a Newtonian fluid, mostly following the work of [85].

2.5.1 Uncertainties in the MSD

The MSD of a particle undergoing a random walk is given by $\langle r^2 \rangle = \langle (\sum_{i=1}^{n} \Delta r_i)^2 \rangle$, where Δr_i is the displacement of the particle in the ith step, n is the total number of steps, and the average is over many realizations of the random walk. For a 1D random walk this is equal to $\langle (\sum_{i=1}^{n} \Delta x_i)^2 \rangle = \langle \sum_{i=1}^{n} (\Delta x_i) \sum_{j=1}^{n} (\Delta x_j) \rangle = \sum_{j=1}^{n} \sum_{i=1}^{n} \langle \Delta x_i \Delta x_j \rangle$. Assuming that the random walk is unbiased, i.e. $\langle \Delta x \rangle = 0$, terms where $i \neq j$ are equal to zero. Therefore, the MSD simplifies to $\sum_{i=1}^{n} \langle \Delta x_i^2 \rangle = n \langle \Delta x_i^2 \rangle = n\sigma^2$, where σ^2 is the variance of the displacement in one step. For simplicity, I will restrict the analysis below to only the 1D case, although the results can be trivially extended to a 2D or 3D random walk.

If the Brownian particle is tracked over N images, then the MSD of the random walk as a function of n is given by,

$$\bar{\rho_n} = \frac{1}{K} \sum_{i=1}^{K} |x_{n+i} - x_i|^2 \tag{2.9}$$

where $K = N - n$. The variance of the MSD is given by,

$$\sigma_n^2 = \langle \bar{\rho_n}^2 \rangle - \langle \bar{\rho_n} \rangle^2 \tag{2.10}$$

where the average is taken over many iterations of the random walk. The second term of this equation is equal to $(n\sigma^2)^2$. Evaluating the first term is less straightforward

(see [85] for the computation in 2D). The final result is

$$\sigma_n^2 = \begin{cases} 2\sigma^4 \frac{n}{6K^2}(2K + n + 4n^2K - n^3) & n \leq K \\ 2\sigma^4 \frac{1}{6K}(K^3 + 4n - 4K^2n + 6n^2K - K) & n \geq K \end{cases} \tag{2.11}$$

The two domains of the solution given above, $n \leq K$, and $n \geq K$, are regions in which the calculated MSD contain partially independent data and entirely correlated data, respectively. As an example of this, if $n = 2$ and $N = 5$, then three values of the squared-displacement between frame pairs are averaged to find the MSD: ((1,3),(2,4), and (3,5)), with two of them ((1,3) and (3,5)) being statistically independent. Whereas if $n = 3$, then there are no statistically independent values and the averaged MSD only contains correlated data.

For an ensemble average over the independent trajectories of P particles, the variance given above can simply be divided by P. The results can also be multiplied by the number of dimensions to extend the applicability to higher dimensional random walks.

The measured position of a particle is uncertain due to effects such as image noise and the motion of the particle during the exposure time of the captured image. These localization uncertainties are referred to as static error and dynamic error, respectively [118]. Localization uncertainty has the effect of shifting the measured MSD vertically by $d\left(2\epsilon^2 - \frac{Dt_e}{3}\right)$, where the first term is due to image noise and the second is due to dynamic error, with t_e the exposure time of the image and d the number of dimensions. The image noise results in a positive shift of the MSD due

to the uncertainty in the particle's position leading to a larger measured squared displacement of the particle on average. The negative contribution from dynamic error can be understood if one assumes that the measured position of the particle during an exposure is the average of the particle's position during the exposure time. In this case, the measured MSD is smaller than the true value since the average position of the particle undergoing a random walk tends to be closer to its initial position than its actual final position. Typically, the dynamic error is small compared to the static error so that the former can be ignored, and the adjusted measured MSD can be written as

$$\bar{\rho_n} = \frac{1}{K}\sum_{i=1}^{K} |x_{n+i} + \chi_{n+i} - x_i - \chi_i|^2 \tag{2.12}$$

where x is the actual position of the particle and χ is a random variable with mean of zero and variance of ϵ^2 that represents the static localization uncertainty in each image. Accounting for the static localization uncertainty leads to the following variance of the measured MSD,

$$\sigma_n^2 = \begin{cases} 2\sigma^4 \frac{n}{6K^2}(2K + n + 4n^2K - n^3) + \frac{4\epsilon^2}{K^2}(3\epsilon^2 K - n\epsilon^2 + 2n\sigma^2 K) & n \leq K \\ 2\sigma^4 \frac{1}{6K}(K^3 + 4n - 4K^2 n + 6n^2 K - K) + \frac{8\epsilon^2}{K}(\epsilon^2 + n\sigma^2) & n \geq K \end{cases} \tag{2.13}$$

One method that can be employed to determine the static localization uncertainty is to video a colloid that is spatially fixed. The measured MSD will then be due to noise alone and therefore equal to a constant, $2\epsilon^2$. Another method is to conduct a linear fit to the MSD and use the intercept as an approximation to this value.

2.5.2 Optimal Linear-Least-Squares Fitting

A particle undergoing diffusion in a homogeneous, Newtonian fluid will have a MSD that scales linearly with time. The diffusion coefficient D is proportional to the slope of this line and can be estimated by conducting a linear fit to the MSD. Because there are more frame pairs over which to average at smaller values of n, it is preferable to conduct the fit by giving more weight to the smaller lag times. In practice, often 10% of the data at the lowest lag times is used in the fit, with the highest 90% not used. The optimal number of data points to use in the fit is based upon the diffusion rate and the amount of image noise. Specifically (see [85]), the optimal number of MSD data points to use in the fit of the MSD is given by the empirical formula,

$$p = 2 + 2.7\sqrt{\frac{\epsilon^2}{D\Delta t}} \tag{2.14}$$

The ratio, $\epsilon^2/D\Delta t$, is the y-intercept of the MSD divided by the mean-squared-displacement between adjacent frames. It is also equivalent to the ratio of the intercept to the slope times the frame rate. Note that in the case in which the localization uncertainty is zero, the optimal number of MSD points to use in the fit is just 2. For a video of 1000 frames, using 10% of the data would be a large overestimation of the optimal number, leading to potentially very significant inaccuracies in the fit parameters.

The linear least-squared problem involves finding a line that passes through a set of data such that the squared-deviations between the data and the line are minimized.

If $\mathbf{y} = \hat{x}\boldsymbol{\beta} + \boldsymbol{\epsilon}$, where $\mathbf{y}$ is the observation vector, $\boldsymbol{\beta}$ is the parameter vector, $\hat{x}$ is the design matrix, and $\boldsymbol{\epsilon}$ is the residual, then the least-squares problem involves finding a value for $\boldsymbol{\beta}$ that minimizes the squared deviation, $\|\mathbf{y} - \hat{x}\boldsymbol{\beta}\|$. Assuming that $\hat{x}^T\hat{x}$ is invertible, a unique solution to this problem is given by $\overline{\boldsymbol{\beta}} = (\hat{x}^T\hat{x})^{-1}\hat{x}^T\mathbf{y}$, where $\overline{\boldsymbol{\beta}}$ is the best estimate of $\boldsymbol{\beta}$ [65].

In the case in which the data is correlated, however, the best-linear-unbiased estimate (BLUE) of the parameter $\boldsymbol{\beta}$ is determined by the generalized-least-squares (GLS) method [2]. The correlation of the data results in a modified equation, $\mathbf{y}^* = \hat{x}^*\boldsymbol{\beta} - \boldsymbol{\epsilon}^*$, with $\mathbf{y}^* = \hat{C}^{-1}\mathbf{y}$, $\hat{x}^* = \hat{C}^{-1}\hat{x}$, and $\boldsymbol{\epsilon}^* = \hat{C}^{-1}\boldsymbol{\epsilon}$. The matrix $\hat{C}$ is determined via the relation $\hat{\Omega} = \hat{C}\hat{C}^T$, where $\hat{\Omega}$ is the covariance matrix of the residual vector $\boldsymbol{\epsilon}$. The residual vector of the modified linear equation is uncorrelated. In the special case in which the off-diagonal entries of the covariance matrix are zero, the GLS method reduces to a weighted linear-least-squares method.

The optimal value for $\boldsymbol{\beta}$ is given by a least-squares solution to this modified equation [11]. Therefore, the optimal value for $\boldsymbol{\beta}$ is equal to,

$$\overline{\boldsymbol{\beta}} = (\hat{x}^T\hat{\Omega}^{-1}\hat{x})^{-1}\hat{x}^T\hat{\Omega}^{-1} \tag{2.15}$$

The uncertainties in the fit parameter can be determined from the covariance matrix of the fit parameter, $\overline{\boldsymbol{\beta}}$, which is given by,

$$cov(\boldsymbol{\beta}) = (\hat{x}^T\hat{\Omega}^{-1}\hat{x})^{-1} \tag{2.16}$$

To apply the generalized least-squares method to MSD data, it is necessary to use

the covariance of the measured MSD, $\sigma^2_{n,m} = \langle \rho_m \rho_n \rangle - \langle \rho_m \rangle \langle \rho_n \rangle$ (see [85]),

$$\sigma^2_{n,m} = \begin{cases} \sigma^4 \frac{m}{3K_n K_m}(1 - m^2 - m(6n^2 - 6nN - 1) - m^3) \\ \quad + \frac{8\epsilon^2}{K_m}\left(\left(1 - \frac{m}{2K_n}\right)\epsilon^2 + m\sigma^2\right) + \frac{4\epsilon^4}{K}\delta_{m,n} & n + m \leq N \\ \sigma^4 \frac{1}{3K_m}(K_n^3 - 4mK_n^2 + 6m^2N - N - 6m^3 + 4m + n) \\ \quad + \frac{4\epsilon^2}{K_m}(\epsilon^2 + 2m\sigma^2) + \frac{4\epsilon^4}{K}\delta_{m,n} & n + m \geq N \end{cases} \tag{2.17}$$

where $K_n = N - n$ and $K_m = N - m$. This covariance matrix is equal to $\hat{\Omega}$ and, therefore, can be used to find $\boldsymbol{\beta}$ from Eq. (2.15).

In order to test these different fitting methods, simulations of a random walk of $N = 1000$ total steps were performed. The variance of the random step length, σ^2 was set to 30 and the variance of the random noise, ϵ^2, was set to 45. The slope and intercept were compared using three different fitting methods. A linear fit using the first 5 percent of the data points, or 50 total points, was taken, as well as a linear fit using the optimal number of data points given by Eqn. 2.14, which is 7 in this case. The generalized-least-squares method was performed also. An example of the result from one random walk is shown in Fig. 2.5 along with each of these three fits.

In this case, the linear fit to the first 5% of the data does the poorest job (estimated slope of 36.2±0.2 and intercept of 70±6), while the linear fit using the optimal number of 7 MSD points (estimated slope of 33.3 ± 0.9 and intercept of 94 ± 4) and the GLS method (estimated slope of 32±3 and intercept of 98±7) give more accurate estimates of the true slope of 30 and intercept of 90. It is of particular interest that in the case

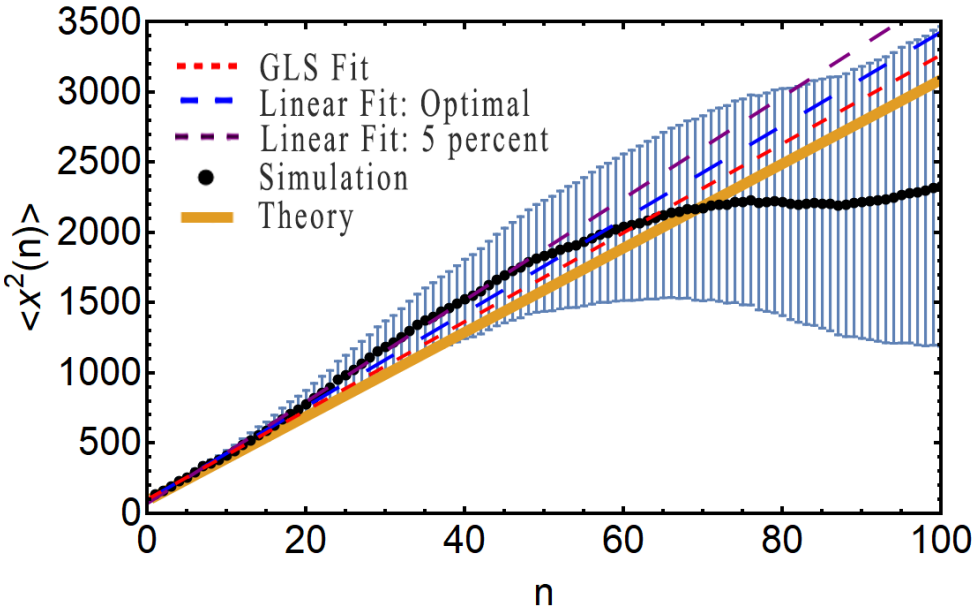

Figure 2.5: Calculated MSD from a simulated random walk with a Gaussian-distributed step length of mean zero and variance equal to 30. The random walk includes a Gaussian-distributed random noise, χ, of mean zero and a variance of 45. The random walk consists of 1000 total steps. The error bars on the MSD are derived from Eq. (2.13). The orange solid line represents the theoretical value, $\langle x^2(n)\rangle = 90 + 30n$, i.e. the result that would be obtained after averaging an infinite number of trajectories. Three fits to the data were performed, as indicated by the dashed lines. The purple-dashed line is found from a fit to the first 50 data points, or 5 percent of the total length of the MSD. The blue-dashed line shows the result of a linear fit to the first 7 data points, which is the optimal number of fit points according to Eq. (2.14). The red-dashed line is from a generalized-least-squares fit to the data.

of the linear fits, the estimated uncertainty in the slopes, if taken literally, would indicate that the result is statistically significantly different from the true slope of 30. However, the uncertainty determined via the GLS method gives a more accurate, larger value, due to the consideration of the correlation in the data.

To compare the accuracy of the determined slope from each of the three fitting methods, 2500 simulations were performed and the standard deviation of the estimated slopes from each of these methods was determined. It was found that the linear fit to the first 5% of the data points resulted in a standard deviation of the slope of 8.2 ± 0.1. The linear fit using the optimal number of data points gave a standard deviation of 3.49 ± 0.05, while the GLS method produced a standard deviation of 3.15 ± 0.05. Therefore, the latter two methods are considerably more precise than the fit to the first 5% of the data. The difference between the GLS method and the method that used the optimal number of data points is quite small, therefore either method will generally suffice in producing a relatively precise estimation of the diffusion coefficient.

In practice, it is often sufficient to reduce the covariance matrix, $\hat{\Omega}$, to a much smaller size due to the relative statistical insignificance of the data points at large values of n. This decreases the computational time and produces nearly identical results if a sufficient number of points is used. With large noise, more of the MSD data should be used in the fit, as indicated by Eqn. 2.14.

Chapter 3

Driven Topological Transitions in Active Nematic Films

3.1 Introduction

The following work was conducted in collaboration with Tyler Shendruk in the Interdisciplinary Centre for Mathematical Modelling and Department of Mathematical Sciences at Loughborough University. The results of this chapter have been published in the journal *Soft Matter* [109].

Topological defects in the ordered states of physical systems can play critical roles in determining their properties. In condensed matter, examples include magnetic flux lines penetrating type-II superconductors, dislocations in crystalline solids, and singular regions in the magnetization of ferromagnetic thin films [1, 16, 37]. These

structures, which possess a conserved topological charge, have non-local effects on the order within the systems, whose dynamics can often be described in terms of the defects' quasi-particle-like motion and interactions. Further, the ability to control defect behavior is essential for applications.

Particularly intriguing topological defect dynamics occur in active nematic films, which are quasi-two-dimensional (2D) fluids composed of rod-like constituents that possess the orientational order of nematic liquid crystals but flow spontaneously due to an internal energy source [81, 89, 116]. Examples include cell cultures [26, 56, 119, 164, 166], bacteria suspensions [29, 33, 58, 91, 161], granular media [87], and engineered systems composed of dense solutions of microtubule or actin biopolymers adsorbed at oil-water interfaces and driven by molecular motors [60, 117]. In the microtubule films, the local orientation of the microtubules defines the nematic director field $\mathbf{n}(\mathbf{r})$. Activity induced by the molecular motors causes the microtubules to slide along one another, creating extensional strains that drive bend instabilities in $\mathbf{n}(\mathbf{r})$ that lead to the perpetual creation and annihilation of pairs of defects with topological charges $\pm 1/2$. The extensional strains further propel the $+1/2$ defects, leading to striking, turbulence-like flows [32, 68, 138].

In the case of traditional liquid crystals, much of the technological importance derives from the ability to address and reconfigure the order locally and dynamically through a combination of patterned boundary conditions and applied fields. Progress toward achieving comparable manipulation of active nematics requires control of the

dynamic defects. Recent experiments have demonstrated passive approaches to affect defect behavior via spatially resolved alignment of the director through confining boundary conditions [49,50,94] that can be considered analogous to surface anchoring. However, the ability to couple actively and tunably to local active nematic behavior, and to defect motion in particular, through applied fields has not been realized. Here, we report combined experiments and simulations in which we demonstrate and model local, dynamic influence over the flow properties and director field structure in active nematic films through stress fields created by rotating disk-shaped colloids in proximity to the films. The hydrodynamic stresses produced by the disks alter the behavior of the active nematic by steering the motion of the topological defects, which allows us to infer anomalous viscoelastic properties of the active films. Most notably, we find that above a threshold applied stress, a rotating disk can entrain two $+1/2$ defects and induce their fusion into a single vortex structure with topological charge $+1$. In overcoming the innate repulsion between like-charged topological objects, which ordinarily is a critical determining factor in the dynamics of multi-defect states, this defect merger illustrates the degree of control of topological properties that can be achieved in active systems.

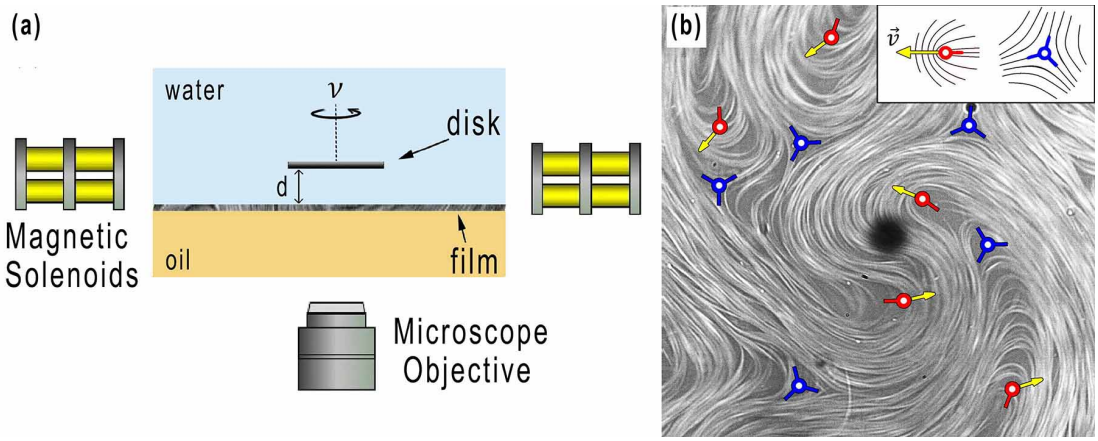

Figure 3.1: Experimental design for imposing stress locally on active nematic films. (a) A 40-μm-diameter ferromagnetic Ni disk positioned a height $d = 15 - 40$ μm above a film is rotated at a frequency ν by a magnetic field created by a set of four pairs of solenoids (two shown) mounted an inverted fluorescence microscope. (b) Example image of a disk rotating counterclockwise above a film composed of fluorescently labeled microtubule bundles. The nematic film is populated with $-1/2$ (blue) and $+1/2$ (red) topological defects. The instantaneous velocities of the mobile $+1/2$ defects are indicated by the yellow arrows, and their orientation vectors are indicated by red arrows.

3.2 Materials and Methods

Active nematic films, composed of a dense layer of fluorescent microtubule bundles driven by kinesin molecular motors, were formed at oil-water interfaces [117] using materials provided by the Brandeis University Materials Research Science and Engineering Center Biological Materials Facility, as detailed in the Appendix. As part of the film formation, 40-μm-diameter ferromagnetic nickel disks, introduced into the aqueous phase, became positioned at a height d = 3-8 μm above the film with the disk faces parallel to the film. This height appeared to be set by a thin, dilute layer of unadsorbed microtubules adjacent to the film upon which the disks rested.

Observations of the disks and films were made on an inverted microscope (Nikon TE2000) using a Flare CameraLink camera (IOIndustries), as described in the Appendix. Four pairs of solenoids mounted on the microscope [66] generated rotating magnetic fields of specified magnitude and frequencies up to $\nu = 120$ Hz in the plane of the film. A schematic of the experiment is given in Fig. 5.1a. The magnetic moments of the disks lie in the disk plane, hence the magnetic torque from the applied fields caused the disks to rotate about their axes also at frequency ν. When rotated, the disks rose to a greater height above the film. For instance, at $\nu = 80$ Hz, the disks typically reached d = 15-40 μm. We identify this rise with a possible normal force due to the non-Newtonian character of the dilute suspension of unadsorbed microtubules between the disk and film [63]. Figure 5.1b shows an image of a rotating disk above an active nematic film where the +1/2 and -1/2 defects are labeled. The orientation

vectors $\hat{\psi}$ of the $+1/2$ defects [140, 155] and the directions of the instantaneous velocities of their self-propelled motion, which is approximately antiparallel to $\hat{\psi}$, are further indicated.

3.3 Results

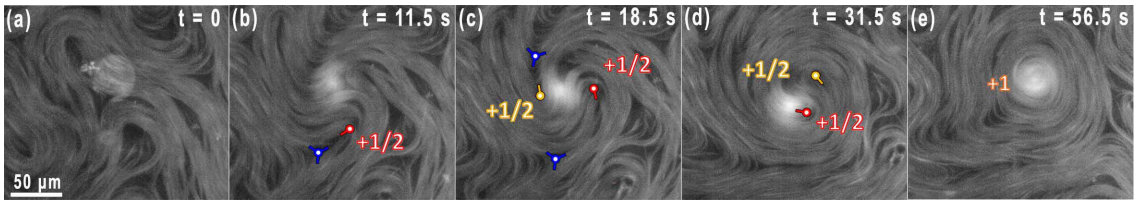

Figure 3.2: Fluorescence micrographs showing topological vortex formation in an active nematic film. (a) A non-rotating disk (bright circle) sits atop the active nematic film just prior to application of a magnetic field rotating at 80 Hz. (b) A $\pm 1/2$ defect pair is created in proximity to the disk. (c) A second $\pm 1/2$ defect pair forms near the disk, while the stresses imposed by the disk cause the positive defects to orient and circle the disk. (d) The $+1/2$ defects spiral in towards the disk center. (e) The two $+1/2$ defects fuse to form a $+1$ topological vortex, thus conserving the overall charge of the system.

3.3.1 Topological vortex formation and decay.

When the applied magnetic field was zero and the disk was not rotating, it had no observable effect on the active nematic; however, the disk was carried along with the flow of the film, indicating the thin aqueous layer between disk and film provided a strong hydrodynamic coupling between the disk and film. Consequently, when a disk

rotated, it imposed significant hydrodynamic stresses on the film, influencing the local nematic order and active flows. A quantitative estimate of the stresses is provided in the Appendix. Above a threshold ν, typically 60-120 Hz, the stresses were sufficient to drive topological transitions in the nematic order, wherein topological vortices with +1 topological charge were created from the fusion of two +1/2 defects. Figure 3.2 shows a series of images of a film during creation of a topological vortex. Since total topological charge must be conserved, vortex creation necessitated a change in the total topological charge of the population of 1/2-charged defects existing in the film. For instance, in Fig. 3.2, two +1/2 and -1/2 defect pairs are created in the vicinity of the disk (Figs. 3.2b and c). The +1/2 defects spiral inward toward the disk until they merge to form the +1 vortex defect (Fig. 3.2e), leaving the -1/2 defects behind to eventually annihilate with other +1/2 defects in the film. The vicinity of the rotating disk was a frequent location for formation of 1/2-charged defect pairs, likely due to the tendency of the director to align azimuthally in response to the external flow coupled with the hydrodynamic bend instability of the active nematic [107, 125], and hence formation of topological vortices commonly involved the merger of +1/2 defects that were created near the disk as in Fig. 3.2. However, the +1/2 defects involved in topological vortex formation sometimes originated far from the disk and became captured as they passed in proximity to the disk.

To explore further the merger of +1/2 defects into a topological object of charge +1, we conducted simulations of active nematic films coupled to rotating disks by

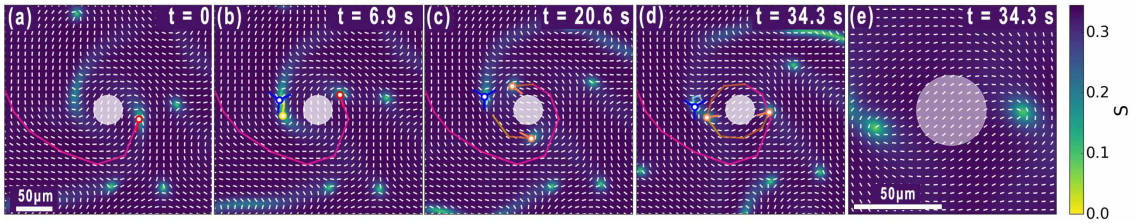

Figure 3.3: Simulation of the merger of two +1/2 defects into a +1 topological structure by a rotating disk. (a) A +1/2 defect (trajectory in red) begins circling the disk. (b) A defect pair is created near the disk. (c) The two +1/2 defects circle the disk. (d) The +1/2 defects orient in a radial manner to create a metastable bound state. (e) Magnified view of the +1 topological structure in panel d. The white lines display the director field and the color map indicates the scalar order parameter S. The disk-to-film coupling is $\zeta_{\text{d-f}} = 0.03$, and the alignment parameter is $\lambda = 0.3$.

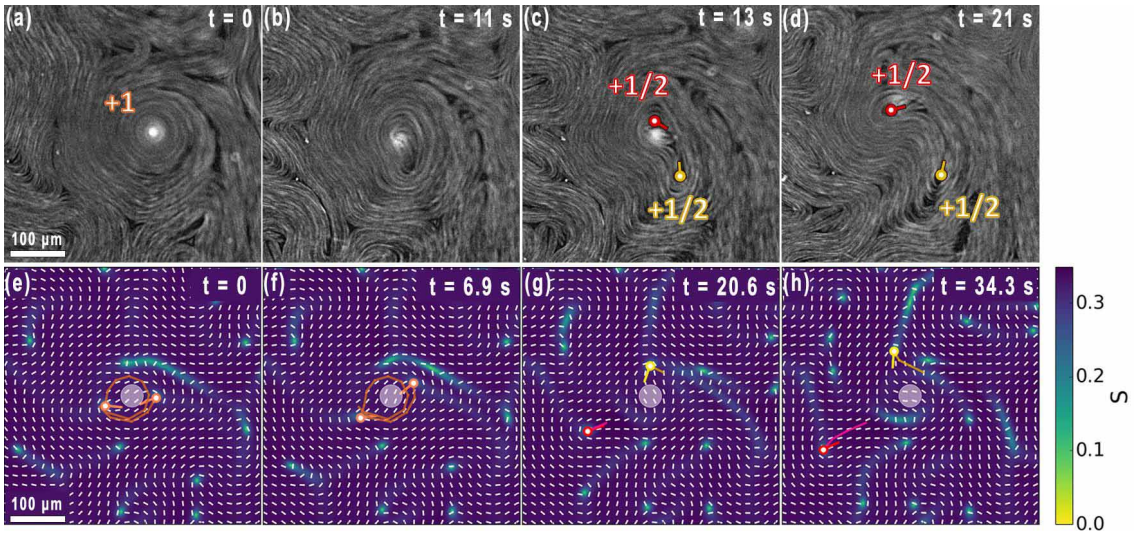

Figure 3.4: Topological vortex decay. (a-d) Fluorescence micrographs showing the +1 topological structure dividing into two +1/2 defects that then propagate away from each other. (a) shows a +1 topological vortex created by a rotating disk (seen as a bright spot in the image). (b) shows the initial instability of the azimuthally oriented director about the vortex. A short time later in (c), two clearly separated +1/2 defects are apparent. In (d) the defects continue to propagate away from each other. (e-h) Simulations (with $\zeta_{\text{d-f}} = 0.03$ and $\lambda = 0.3$.) showing the decay of a +1 topological structure. The white lines in (e-h) display the director field and the color map indicates the scalar order parameter S.

solving the Beris-Edwards formulation of nematohydrodynamics, employing a Lattice-Boltzmann (LB) algorithm for the flow field and finite difference for the orientation tensor [39, 82, 124, 141]. Details regarding the simulations are provided in the Appendix. Simulation parameters were chosen to optimize agreement with spatial and temporal correlations in vorticity in the experiments, thereby setting the length and time scales for the simulation. The disk in the simulations was subjected to a constant torque to drive rotation. The coupling between disk and active nematic film, which we interpret as a viscous coupling through the thin aqueous layer between disk and film in the experiment, was modeled in the simulations by a drag coefficient $\zeta_{\text{d-f}}$, whose magnitude served as a proxy for effective rotation rate. Similarly, the nematic orientation is coupled to velocity gradients within the film by an alignment parameter λ (see Appendix).

Figure 3.3 illustrates a defect merger event in a simulation that mirrors the topological vortex formation in the experiments. A +1/2 defect was drawn from the surrounding bulk turbulence into orbit about the rotating disk and proceeded to spiral toward the disk with $\hat{\psi}$ oriented azimuthally (Fig. 3.3a). A second +1/2 defect appeared in the vicinity of the disk by a pair creation event (Fig. 3.3b), and the two +1/2 defects began orbiting the disk on opposites sides from each other. As they orbited, the defects re-oriented so that each $\hat{\psi}$ pointed radially inward thereby forming a bound pair that constituted a +1 topological complex (Figs. 3.3c and d). The +1 topological objects formed in the experiments and simulations hence differed in their

core structure. While in the simulations the core contained two distinguishable +1/2 defects linked by a well defined local director field (Fig. 3.3e), in the experiments the +1/2 defects merged fully to form a singular, point-like core like in Fig. 3.2e (see also Fig. 3.4a below). We identify the complete merger in the experiments with a nonlinear rheological response of the active nematic films described below.

Such fusion of like-charge topological defects as in Fig. 3.2 is unusual in nature. Like-charge defects typically interact through long-range repulsion [140, 155]. Furthermore, a +1 topological vortex in a nematic has higher energy than two +1/2 defects [24], so the merger requires input of energy, While these restrictions make such defect mergers rare in passive liquid crystals, the internal energy source driving the flows in active nematics can under appropriate conditions, such as under confinement [49], facilitate defect merger. We see further here how locally applied external fields, in this case hydrodynamic stresses, in conjunction with the activity can drive defect mergers.

As high-energy quasi-particles, the topological vortices were susceptible to decay. Further, since deformations of the director field in the vicinity of the +1 defect are pure bend, sustaining the configuration required suppressing the hydrodynamic instability intrinsic to the active nematic films that drives flow normal to the director in regions of bend and leads to amplification of the bend distortion [107, 125]. In the experiments, the stresses from the rotating disk could nevertheless stabilize the +1 defect for extended periods, longer than 6 minutes in one measurement, a time

scale far exceeding the intrinsic correlation time of the active nematic, which was approximately 30 s (see Appendix). However, fluctuations in the disk position or local nematic order would eventually lead the vortex to decay into a pair of lower-energy +1/2 defects that then propagated away from one another (Figs. 3.4a-d). The +1 topological structures in the simulations decayed similarly (Figs. 3.4e-h). The lifetimes of the +1 topological objects in the simulations depended on the alignment parameter λ. Increasing the parameter from $\lambda = 0.3$ into the flow aligning regime, $\lambda = 0.7$, decreases the rate of topological vortex decay events for $\zeta_{\text{d-f}} = 0.03$. If either the coupling is increased to $\zeta_{\text{d-f}} = 0.07$ or the alignment is increased to $\lambda = 0.9$, only a single merger event is observed and the resulting +1 topological structure persists for the duration of the simulation. The sensitivity of the lifetime to the film parameters in the simulations reflects the coupling of the orientation field to the hydrodynamic stress. As seen in Figs. 3.3e or 3.4e, the +1/2 defects in the simulations orient such that the hydrodynamic stresses binding them within the +1 complex must maintain balance with the active stresses that would otherwise propel the +1/2 defects radially outward.

The speed of the +1/2 defects formed in a vortex decay reached their intrinsic, self-propelled speed essentially immediately and showed no dependence on separation, implying any effects of elastic interactions [140, 155] between the defects were overwhelmed by their activity-driven motion [121] (see Appendix). Once a vortex decayed, the stresses from the rotating disk would drive creation of a new vortex, so

that the process repeated. The time scale for new vortex formation could vary from a few seconds to upwards of a minute, as dictated by the time to entrain two new +1/2 defects and develop the non-linear, shear-thinned state in the film described below. This variation and the varied lifetimes of the topological vorticies reflect a stochastic element to the process that results from the close contact between the region of the film under strong influence of the disk and the surrounding sea of active turbulence.

This vortex decay into a defect pair is distinct from the behavior observed in other recent experiments on active nematics that tracked the emergence of active turbulence from ordered director fields. In those cases, where the ordering was imposed by passive confinement [49] or was prepared over large areas [83,131], the return to turbulent flow was initiated by bend instabilities intrinsic to the active nematic with a characteristic wave length set by the film properties. In contrast, the +1 defect decay in Fig. 3.4 has a quasi-particle-like nature in that the decay produces two, clearly identifiable +1/2 point defects that are in close proximity to the parent +1 point defect and that have subsequent trajectories that are easily tracked. We attribute this quasi-particle nature to the ability of the controlled stresses imposed by the disk to strongly and locally alter the active nematic ordering and dynamics.

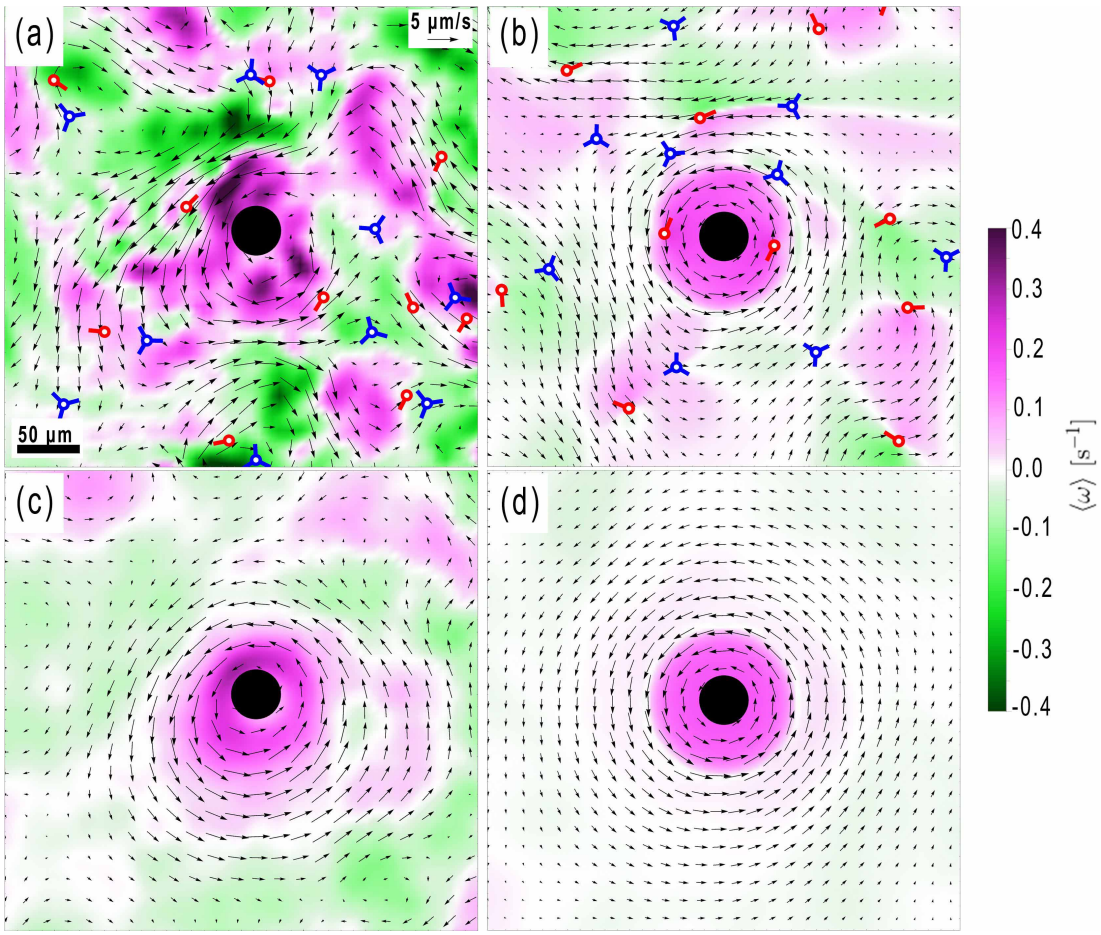

Figure 3.5: Instantaneous and time-averaged properties of the active nematic flows. (a) Map of the instantaneous vorticity (color scale) and velocity field (arrows) in an active nematic film in the presence of a disk rotating counterclockwise at 120 Hz. Red and blue markers indicated the +1/2 and -1/2 defects, respectively. (b) The same instantaneous quantities taken from LB simulation with coupling $\zeta_{\text{d-f}} = 0.07$ and alignment parameter $\lambda = 0.3$. (c) Map of the vorticity and velocity averaged over 300 s in the experiment. (d) Corresponding time-averaged quantities in the simulation.

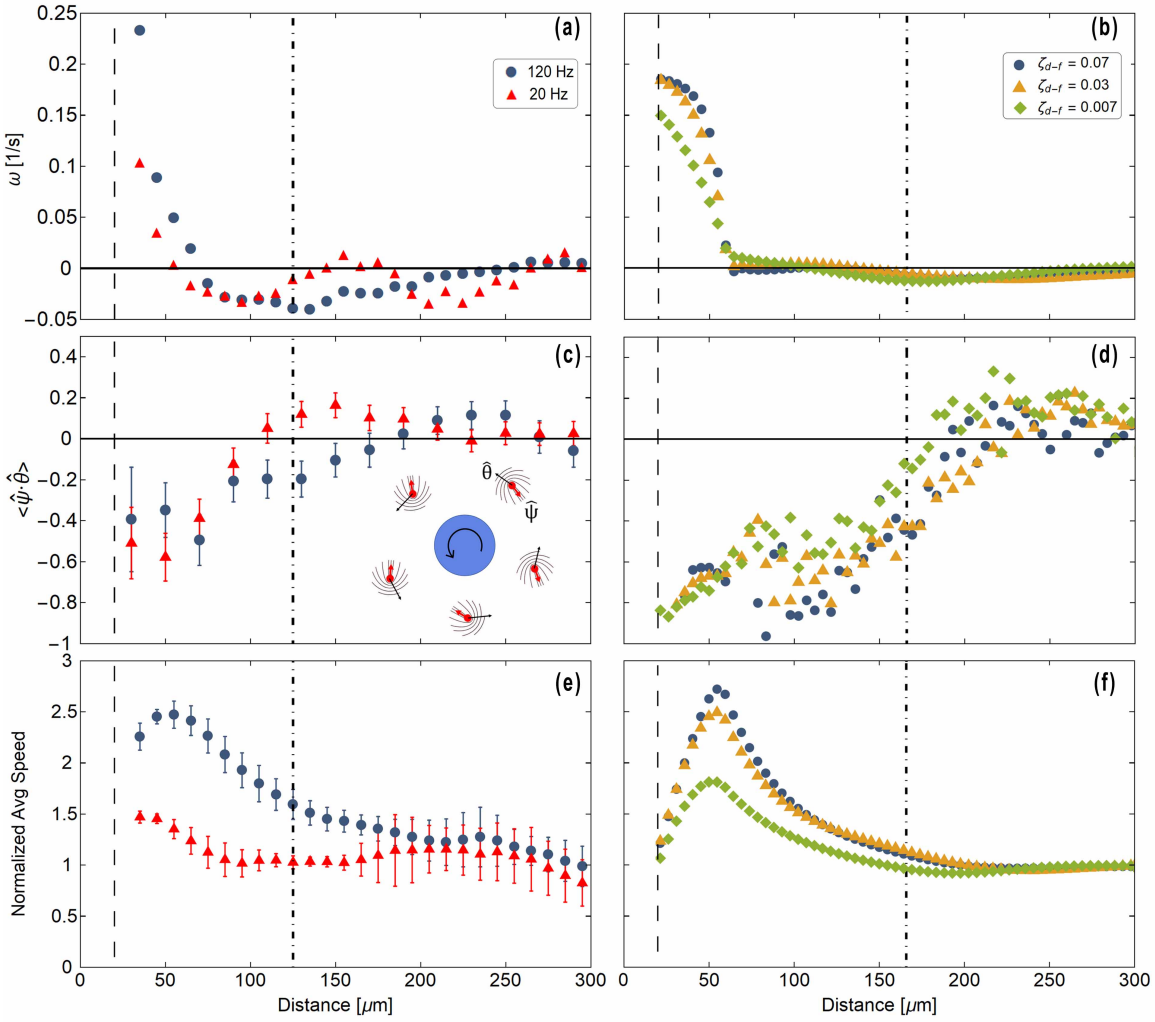

Figure 3.6: Characterization of the nematic order and flow in the vicinity of a rotating disk in the absence of a +1 topological vortex. (a) The time and azimuthally averaged vorticity measured in experiment as a function of distance from the disk center at two disk rotation rates. (b) The same quantity obtained in the absence of the +1 topological vortex from simulations at different disk-film couplings. (c) The experimental and (d) the simulated average azimuthal component of the unit orientation vector, $\hat{\psi}$, of the +1/2 defects as a function of distance from the center of a disk. The negative values near the disk indicate a tendency for the defects to circulate about the disk in its direction of rotation, as shown schematically in the inset in (c). (e) experimental and (f) simulated speed of the film, normalized by the average speed due to the activity far from the disk. The vertical dashed lines indicate the radius of the disk, 20 μm, and the vertical dot-dashed lines indicate the nematic correlation lengths. The alignment parameter in the simulations was $\lambda = 0.7$.

3.3.2 Effects of imposed stress on active nematic structure and flow.

In addition to the striking formation of a high-energy +1 topological vortex through defect merger, the hydrodynamic stresses from the rotating disk imposed more subtle effects on the nematic order and active flows. For example, Fig. 3.5 displays maps of the flows in the vicinity of a disk rotating at 120 Hz during a period in which no +1 topological vortex has formed (see Appendix for image analysis details). Figure 3.5a shows the instantaneous velocity field and the magnitude of the instantaneous vorticity, $\vec{\omega} = \vec{\nabla} \times \vec{v}$, in the flow. Active nematics intrinsically possess regions of non-zero flow vorticity [68], and the regions of positive and negative vorticity in Fig. 3.5a reflect this structure. The instantaneous flows in the simulation show similar structure, as illustrated in Fig. 3.5b, and further show how the propagating +1/2 defects are accompanied on either side by regions of clockwise and counter-clockwise local vortices in the flow [47]. In fact, in Fig. 3.5b one sees the two +1/2 defects nearest the center of the disk oriented such that their counter-clockwise flow vortices co-rotate with the flow vorticity created by the disk.

Figures 3.5c and d display the same quantities averaged over 300 seconds. Due to the active turbulence of the flow, the structure at a fixed position ordinarily decorrelates on a time scale of approximately 30 seconds (see Appendix); so in the absence of the rotating disk, both quantities in Figs. 3.5c and d would be essentially zero when

averaged over 300 seconds. The non-zero values hence illustrate the ability of the stresses from the rotating disk to compete with the active stress and influence locally the flow of the active nematic.

This influence is apparent even at disk rotation rates well below the threshold for creating a topological vortex. For example, Fig. 3.6 shows a set of quantities characterizing the time-averaged and azimuthally averaged nematic order and flow as a function of distance from the disk center in the absence of a +1 topological object. The experimental data is shown for disk rotation rates of both 120 Hz (during periods when no topological vortex forms) and 20 Hz, a rate below the threshold for topological vortex formation. Figure 3.6a shows the time-averaged flow vorticity which is positive near the disk and negative at intermediate distances. Simulations also show large positive vorticity near the disk and near-zero negative values at larger distance (Fig. 3.6b). In the simulations, the region of time-averaged negative vorticity is reproduced only when a small drag term [31,142] is included to account for viscous dissipation in the thin oil layer below the film (Fig. 5.1a), illustrating the importance of such dissipation to the properties of the active flows in experiments [49,51].

Orientational ordering of the defects is shown in Figs. 3.6c and d, which display the time-averaged and azimuthal-averaged component of the +1/2 defect orientation vector $\hat{\psi}$ along the azimuthal direction $\hat{\theta}$ with respect to the disk center. The +1/2 defects in close vicinity to the rotating disk tend to orient so that $\left\langle \hat{\psi} \cdot \hat{\theta} \right\rangle < 0$, as illustrated in the inset of Fig. 3.6c, while farther from the disk $\left\langle \hat{\psi} \cdot \hat{\theta} \right\rangle > 0$. In

the unperturbed active nematic, the extensional flows cause the +1/2 defects to move anti-parallel to $\hat{\psi}$. Thus, one might interpret the region with $\left\langle \hat{\psi} \cdot \hat{\theta} \right\rangle < 0$ as a tendency for the self-propelled defects to orient in order to co-circulate in the net flow seen in Fig. 3.5c. However, additional LB simulations of rotating disks near passive films and active nematic films with contractile active stresses, in which the direction of self-propelled motion of the +1/2 defects flips, also show defects co-circulate in the disk's flow with $\left\langle \hat{\psi} \cdot \hat{\theta} \right\rangle < 0$. We hence conclude that the torque orienting a +1/2 defect in orbit about the disk is not activity-induced but is related to coupling of $\mathbf{n}(\mathbf{r})$ near the defect with the disk-induced stress field.

We further interpret the region farther from the disk in which $\left\langle \hat{\psi} \cdot \hat{\theta} \right\rangle > 0$ as a preference for defects in that region to orient anti-parallel to those closer to the disk since such anti-parallel orientation minimizes the elastic energy of defect interactions [**?**,156] and allows favorable constructive overlap of the vorticities in the flows around the defects. Indeed, the tendency for near-neighbor +1/2 defects in active nematics to align anti-parallel has been observed in simulations [25] and experiment [60] (see also Fig. 3.9 in the Appendix). Our simulations in Fig. 3.6d also show a small, intermediate-distance peak, which represents the slowing of +1/2 defects that are oriented such that they move against the disk's counter-clockwise rotation. This peak due to increased sampling of counter-moving defects is not discernible in the experimental data of Fig. 3.6c.

Figure 3.6e displays the time-averaged and azimuthal-average speed of the micro-

tubule bundles in the film, which becomes enhanced over the average activity-induced speeds near the disk. The maximum peak beyond the disk radius is reproduced in LB simulations (Fig. 3.6f) by use of an effective hydrodynamic disk size to account for the effect of the near-disk flows on the film.

Each experimentally measured quantity in Fig. 3.6 shows similar trends at $\nu =$ 20 Hz and 120 Hz; however, the influence of the disk is larger and extends farther at the higher rate, implying this difference in influence is a factor in whether or not the stresses from the rotating disk can drive topological vortex formation. (To set the scale, the nematic correlation length, defined in the Appendix, is demarcated by the dash-dotted line in Fig. 3.6.)

3.3.3 Shear thinning of the active nematic.

Accompanying topological vortex formation, as in Fig. 3.2, the velocity of the microtubule bundles in the vicinity of the disk increased significantly, as illustrated in Fig. 3.7, which shows the velocity as a function of distance from the disk center in the presence of a topological vortex and prior to the vortex formation. For reference, the average intrinsic speeds of the microtubules in the film and of the $+1/2$ defects far from the disk due to the activity are shown in Fig. 3.7 by the horizontal dashed-dotted and dotted lines, respectively. Some enhanced flow might be expected in vicinity to the vortex since the nematic director aligns with the shear flow, which

is the orientation in which a nematic typically offers the lowest viscous resistance to flow [24]. However, the large size of the increase in flow velocity that accompanies vortex formation suggests additional factors. Specifically, we interpret it as a nonlinear rheological response of the film, in which a local region with reduced viscosity is created in response to the shear stress. This interpretation is supported by the simulations, where the viscosity terms are not stress dependent and no comparably enhanced flow velocity is observed, suggesting a need to modify existing approaches to model active nematics to capture fully their response to external stress.

Another consequence of this nonlinear response is the high density of microtubule bundles in vicinity of the vortex, which as seen in Figs. 3.2e and 3.4a maintains a value characteristic of the film as a whole, leading to a point-like core. In other cases where $\mathbf{n}(\mathbf{r})$ in active nematics has adopted an azimuthal orientation, which have involved confining the active nematic through boundary conditions [49, 94], the large bend distortion required of the microtubules has led to extended regions devoid of microtubules near the core. Specifically, one can identify such large empty cores of defects in the microtubule system with a regions in which the nematic order parameter is effectively reduced to zero. In conventional liquid crystals, the size of such a core region is set by a competition between the costs to the free energy of imposing large elastic distortions to the director versus converting the nematic to isotropic [24]. The large bend elastic constant of the microtubule system under ordinary conditions hence dictates that azimuthally oriented director configurations have a large empty region

at the center like those ordinarily seen in Refs. [49] and [94]. In contrast, we interpret the essentially singular, point-like structure of the cores of the topological defects created by the disk, like those in Figs. 3.2e and 3.4a, as evidence that the shear-thinned region of the active nematic created by the disk has a substantially reduced bend elastic constant.

To analyze this velocity profile, we modeled the experimental conditions in fluid-dynamics calculations in COMSOL (for details see the Appendix). The modeling characterized the low-Reynolds-number hydrodynamics due to a disk positioned at a height $d = 35$ μm above the film and rotating at $\nu = 80$ Hz to match the experimental conditions of Fig. 3.7. The model films behaved as quasi-2D fluids in which the velocity profile depended on the 2D viscosity η_{2D}. By varying η_{2D} to optimize agreement with the measured velocity profile, we arrived at the solid curve in Fig. 3.7, which corresponds to $\eta_{2D} = 1.3$ Pa·s·μm. Similar analysis of the velocity profiles around other topological vortices leads to an average viscosity for the films in the range $\eta_{2D} \approx$ 0.7-5.0 Pa·s·μm.

This range of viscosities is approximately two orders of magnitude below the range found in a previous study of microtubule-based active nematics in which η_{2D} was estimated from the variation in $+1/2$ defect speed with subphase viscosity [51]. Since we identify the region of the film in vicinity of the vortex with a shear-thinned state, we expect the viscosity to be reduced. However, the difference between the measured values could also point to the problematic nature of identifying a viscosity in

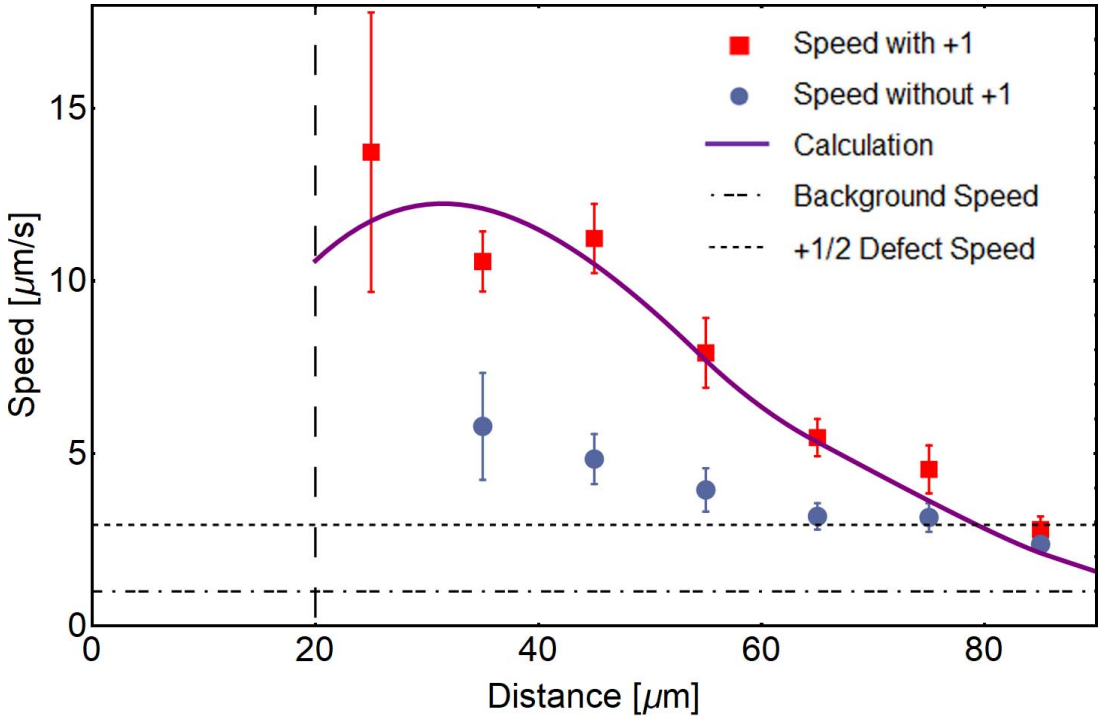

Figure 3.7: Effect of topological vortex formation on the flow speed of the film. The red squares display the speed in the presence of the vortex as a function of the distance from the center of the rotating disk, while the blue circles display the speed prior to vortex formation. The horizontal dashed-dotted line indicates the average speed of microtubules in the film far from the disk due to the activity, and the dotted line displays the average speed of the +1/2 defects far from the disk. The vertical dashed line shows the disk radius. The solid curve shows the result of a best fit to the measured speed in the presence of the vortex, from which a film viscosity of 1.3 Pa·s·μm was obtained. The disk rotation rate was 80 Hz.

these out-of-equilibrium active systems. As seen with suspensions of swimming bacteria [17, 128], and in contrast with conventional Newtonian fluids, different methods of measuring viscosity need not lead to the same result. We note that an additional complication in the interpretation of viscosity in active nematic films arises from the complex and not-yet fully understood coupling between activity, mechanical properties, and topological state of these systems.

3.4 Conclusion

In this work we have demonstrated an original method to couple to the hydrodynamics and nematic order in an active nematic film through application of controlled stress fields and thereby to manipulate defect dynamics. This capability has allowed us to characterize rheological properties of the active system, highlighting its anomalous response to external stress. Most dramatically, this response includes a change in the topological character of the nematic, as two like-charge $+1/2$ topological defects can be drawn together to merge into a singular, point-like defect with charge $+1$. One can envision expanding this approach, for example by investigating the effects of multiple rotating disks that are either free to move in response to interactions or fixed in place. Indeed, an array of such rotating disks arranged in a lattice and coupled to the active nematic film would combine parity-breaking of the induced rotational flows with microscopic irreversibility of the activity to potentially realize

novel functionalities, such as topological sound [132]. Further, when combined with approaches to affect active nematics through patterned boundary conditions [49] and other forces [83], this strategy for engineering the topology and dynamics through appropriately applied local stress fields should find application in other classes of active matter.

3.5 Appendix

3.5.1 Sample Preparation

3.5.1.1 Active Gel Fabrication

The active gel was fabricated by combining appropriate quantities of microtubules, ATP, and a premix solution that contained kinesin clusters, anti-bleaching agents, polyethylene glycol as a depletant, an ATP regeneration system, and buffer, as described in Ref. [25]. The microtubules and premix were provided by Marc Radilla from the Biological Materials Facility at Brandeis University. The final concentration of polyethylene glycol was 0.8% (w/v) and the final concentration of ATP was typically 1.4 mM. The microtubules were labeled with AlexaFluor 647 to enable video tracking of moving bundles using fluorescence microscopy. Prior to formation of an active nematic film, a dilute quantity of ferromagnetic nickel disks was added to the mixture. The disks (radius 20 μm, thickness 300 nm) were fabricated using photolithography

methods described elsewhere [111]. The disks had a permanent magnetic moment μ that was parallel to the disk face and had a magnitude of approximately 1.6×10^{-8} emu (at an applied field of 30 G), as determined from magnetically induced rotations of the disks at a bare oil-water interface.

3.5.1.2 Sample Cell Fabrication

Sample cells were fabricated from two glass slides approximately 1" $\times$ 0.5" that were first cleaned in hot water containing 1% Hellmanex (Hellma) solution and sonicated for $\sim$10 minutes. One slide was made hydrophilic by coating with polyacrylamide, and the other slide was hydrophobically treated using Aquapel (Pittsburgh Glass Works). The hydrophilic treatment involved first sonicating the cleaned glass in ethanol for ten minutes, then rinsing with deionized (DI) water and sonicating in 0.1 M KOH, also for approximately ten minutes. A solution of DI water and 2% w/v acrylamide was placed under vacuum for at least 15 minutes prior to adding 0.035% tetramethylethylenediamine and 0.7 g/L ammonium persulfate. The slides were soaked in a solution of 98.5% ethanol, 1% acetic acid, and 0.5% 3-(trimethoxysilyl) propylmethacrylate for roughly 15 minutes, rinsed again, and then soaked overnight in the acrylamide solution. The slides were rinsed in DI water and dried prior to use. The hydrophobic treatment involved coating the glass in Aquapel for approximately one minute then rinsing with DI water and drying. Thin strips of double-sided tape were placed on the surface of the hydrophobic slides to create two channels of ap-

proximate dimensions 2 cm $\times$ 0.2 cm in which two active nematic films were created. The hydrophilic slides were then laid on top and pressed down onto the tape.

Fluorinated oil (HFE 7500, RAN Biotechnologies) was pipetted into a channel via capillary action. The active gel containing a dilute dispersion of magnetic disks was immediately pipetted into the same channel displacing the oil except for a thin layer adjacent to the hydrophobic surface. The sides of the cell were then sealed with Norland Optical Adhesive 81 (Norland Products), and the cell was centrifuged for 10-15 minutes at 800 rpm (103 g) driving the microtubules to the oil-water interface and leading to formation at the interface of a dense film of microtubule bundles with nematic order. The centrifugation also caused the disks to go to the oil-water interface; however, they did not embed in the film but remained in the aqueous phase at a height $d = 3$ to 8 μm above the film and oriented with their faces parallel to the film, as depicted schematically in Fig. 5.1(a).

3.5.2 Video Microscopy Details

Observations of the disks and film were made with an inverted microscope (Nikon TE2000) and a 20X objective (Nikon, CFI LWD DL 20X). Disks selected for measurements were sufficiently isolated from other disks that the influence of other disks could be safely ignored. (As shown in Fig. 3.6, the effect of the rotating disks on the active nematic films extends at most about 300 micrometers from the disk center. For all the results presented in the paper, the distance between the disks employed

in measurements and any neighboring disks was many times greater than this length scale.) Videos were captured using a Flare CameraLink (IOIndustries) camera with a frame rate of 1 to 5 frames per second. An exposure time of one over the frame rate was typically used for fluorescent imaging. Image analysis was conducted using custom Python scripts, particle imaging velocimetry (PIV) in Matlab, and ImageJ.

In the experiments, magnetic fields $\vec{B}$ rotating in the plane of the film at angular frequency ν were applied. The fields caused the disks to rotate, also at angular frequency ν, with the disk faces parallel to the active nematic film. Specifically, as the field and disk rotated, the magnetic moment $\vec{\mu}$ of the disk lagged $\vec{B}$ by an angle θ such that the magnetic torque on the disk $\mu B \sin\theta$ was balanced by the drag torque on the disk from the surrounding fluid. Due the active turbulence in the nearby active nematic film, this drag torque could fluctuate so that θ fluctuated noticeably if the magnitude of the rotating field was too small. The magnitudes of the fields employed in the experiments were typically 80 to 120 G, which was large enough to ensure that the disks rotated at the prescribed rate, which varied over 20 Hz $\leq \nu \leq$ 120 Hz, without noticeable fluctuations.

We note that disks rotating with their faces at an angle to the film are unstable due to the asymmetry in the drag they experience, and as a result, such disks quickly flip sideways so that they rotate up on end much like a coin spinning on its edge. Occasionally, disks were observed to flip up on end in this way. Fluid-dynamics calculations in COMSOL of disks rotating in this geometry and found that the stress

they impose on the film includes both azimuthal and radial components. However, the radial component is periodic, reversing direction with a frequency of twice the disk rotation frequency. In the experiments, we found the rotating disks that flipped up on end affected the active nematic films in a manner that was qualitatively like the rotating disks whose faces were parallel to the film, including driving the formation of topological vortices. However, all results presented in the paper were obtained from measurements in which the disk face remained parallel to the film.

Measurements of the heights of the disks relative to the films involved adjusting a motorized z-stage on the microscope between positions at which the film and the disk were in focus. An objective with lower depth of field (Nikon, CFI Plan Fluor ELWD 40X) was employed in these measurements for more precise determination of the height, and we estimate the precision of the height measurements to be ± 2 μm. Once a rotating disk reached a steady-state height, its height showed no measurable variation with time; therefore, we consider the disk height to be essentially fixed.

3.5.3 Simulation Details

3.5.3.1 Active Nematohydrodynamics

The ATP-powered microtubule-bundles/kinesin-complexes mixture at an oil/water interface is simulated as a 2D active nematic film. Simulations numerically solve the incompressible active nematohydrodynamics equations of motions [82, 144] for the

local velocity $\vec{u}(\vec{r};t)$ and nematic order $Q(\vec{r};t)$ fields, which obey the coupled Navier-Stokes and Beris-Edwards equations

$$\partial_t \rho + \cdot(\rho\vec{u}) = 0 \tag{3.1}$$

$$\rho D_t \vec{u} = \cdot\Pi - \gamma\vec{u} + \vec{g} \tag{3.2}$$

$$D_t Q - \mathcal{S} = \Gamma H. \tag{3.3}$$

Sufficiently small Mach number ensures near incompressibility, making $\partial_i u_i = 0$ and ρ constant.

The second equation (Eq. 3.2) is the Navier-Stokes equation, in which $D_t = \partial_t + u_k\partial_k$ is the material derivative and Π_{ij} are the components of the stress. The term g_i represents the external force density due to the rotating disk (see Section 3.5.3.2). The Brinkman term γu_i introduces a friction coefficient γ into the film flows [142], which arises from a lubrication approximation for the dissipation within the thin viscous oil layer between the active film and the bottom boundary [13]. The friction coefficient screens hydrodynamic flows over distances much larger than $\sim \sqrt{\eta/\gamma\rho}$, where η is the viscosity of the film. We define the strain rate $E_{ij} = (\partial_i u_j + \partial_j u_i)/2$, vorticity $\mathcal{W}_{ij} = (\partial_i u_j - \partial_j u_i)/2$, and $\mathcal{Q}_{ij} = Q_{ij} + \delta_{ij}/3$. The stresses within the film have four contributions [27]:

1. The Newtonian viscous stress $\Pi_{ij}^{\text{visc}} = 2\eta E_{ij}$.

2. The hydrostatic pressure $\Pi_{ij}^{\text{press}} = -P\delta_{ij}$, which is taken to be constant.

3. The nematic contribution, which itself has symmetric and antisymmetric contributions.

   (a) The symmetric terms are $\Pi_{ij}^{\mathrm{LC,symm}} = 2\lambda \mathcal{Q}_{ij} Q_{kl} H_{lk} - \lambda H_{ik} \mathcal{Q}_{kj} - \lambda \mathcal{Q}_{ik} H_{kj} - \partial_i Q_{kl} \frac{\delta F}{\delta(\partial_j Q_{lk})}$, where H_{ij} is the molecular field and F is the free energy. The alignment parameter λ acts to mix upper and lower convective derivative terms.

   (b) The antisymmetric contribution is $\Pi_{ij}^{\mathrm{LC,anti}} = Q_{ik} H_{kj} - H_{ik} Q_{kj}$.

4. The active stress is directly proportional to the liquid crystaline order $\Pi_{ij}^{\mathrm{act}} = -\zeta Q_{ij}$. The activity ζ is positive for extensile active nematics, such as the microtubule/kinesin-based films, and negative for contractile active nematics.

The final equation (Eq. 3.3) models the evolution of the nematic order tensor. The left-hand side of Eq. 3.3 describes the generalized material derivative accounting for the co-rotational advection, $\mathcal{S}_{ij} = (\lambda E_{ik} + \mathcal{W}_{ik}) \mathcal{Q}_{kj} + \mathcal{Q}_{ik} (\lambda E_{kj} - \mathcal{W}_{kj}) - 2\lambda \mathcal{Q}_{ij} Q_{kl} \partial_k u_l$. The ΓH_{ij} term describes the relaxation of the order parameter towards the free energy minimum, where Γ is a collective rotational diffusivity. The molecular field

$$H = -\frac{\delta F}{\delta Q} + \frac{I}{3} \frac{\delta F}{\delta Q} \tag{3.4}$$

is symmetric and traceless and is related to the functional derivative of the free energy F. The free energy is the sum of two contributions $F = \int d^3 r \left[f^{\mathrm{LdG}} + f^{\mathrm{el}} \right]$, a Landau-de Gennes bulk free energy density $f^{\mathrm{LdG}} = A Q_{ij} Q_{ji}/2 + B Q_{ij} Q_{jk} Q_{ki}/3 +$

$C\left(Q_{ij}Q_{ji}\right)^2/4$ and an elastic deformation free energy $f^{\mathrm{el}} = K\partial_k Q_{ij}\partial_k Q_{ij}$ assuming a single elastic Frank coefficient K.

3.5.3.2 Hybrid Lattice Boltzmann Simulation Details

The equations of motion (Eq. 3.1-3.3) are solved using a hybrid lattice Boltzmann/finite difference scheme [82]. The Navier-Stokes equation (Eq. 3.2) is solved using the lattice Boltzmann algorithm on a D3Q15 grid. On the other hand, Eq. 3.3 is solved using a finite difference predictor-corrector algorithm.

Simulations are performed on a two-dimensional domain of size 400×400 with periodic boundary conditions for 1.5×10^5 time steps. The discrete space and time steps define the simulations units (su; see Section 3.5.3.3), which are used in this section. The density is $\rho = 1$ and the hydrostatic pressure is $P = 1/4$. The Landau–de Gennes coefficients used are $A = 0$, $B = -0.3$, and $C = 0.3$, while the rotational diffusivity is $\Gamma = 0.34$, consistent with our previous works [124]. The dynamic viscosity is $\eta = 2/3$. The friction coefficient is $\gamma = 3 \times 10^{-4}$. The Frank elasticity is $K = 0.1$, while the activity is $\zeta = 5 \times 10^{-3}$ unless otherwise stated. Three values of the alignment parameter are considered, $\lambda = \{0.3, 0.7, 0.9\}$. Simulation parameters were chosen to ensure that the disk size in simulation units was large compared to the discrete lattice spacing.

To account for the stresses on the nematic film due to the ferromagnetic nickel colloidal disk, we model the rotation resulting from constant external magnetic torque.

For simplicity, the disk is fixed in place above the film. The density of the disk is chosen to be 100 times that of the film. In addition to the magnetic torque, the dissipative drag is $-\zeta_{\mathrm{aq}}\Omega$, where Ω is the resulting rotation rate of the disk and $\zeta_{\mathrm{aq}} = 10$ is the rotational drag coefficient of the disk in the aqueous solution. The chosen values ensure that the disk's dynamics are over damped. The rotation of the disk is hydrodynamically coupled to the active flows within the film. We model the effect to be local with coupling only occurring directly below the effective hydrodynamic radius of the disk. The hydrodynamic radius $R^{\mathrm{H}} = 25.2$ is taken to be three times the geometric radius of the disk, which accurately captures the experimentally measured position of the maximum average velocity of the film. The hydrodynamic drag imposed by the rotating disk on the film, which in the experiments is mediated by the viscous coupling through the intervening aqueous layer, is modeled as a force density proportional to the differences in velocity, $\vec{g} = \zeta_{\text{d-f}}\left[\vec{v}\left(\vec{r},t\right) - \vec{u}\left(\vec{r},t\right)\right]$, where the velocity of each element of the disk is $\vec{v}\left(\vec{r},t\right) = \Omega\left(t\right)\hat{z}\times\vec{r}$. The equal and opposite force density on the disk produces a torque on the disk that slightly modifies the rotation rate.

3.5.3.3 Simulation Units

In this study, care has been taken to match simulation units (su) to the physical conditions of the experimental system. Numerical simulations are unitless and appropriate parameters must be chosen to identify possible scalings to convert nu-

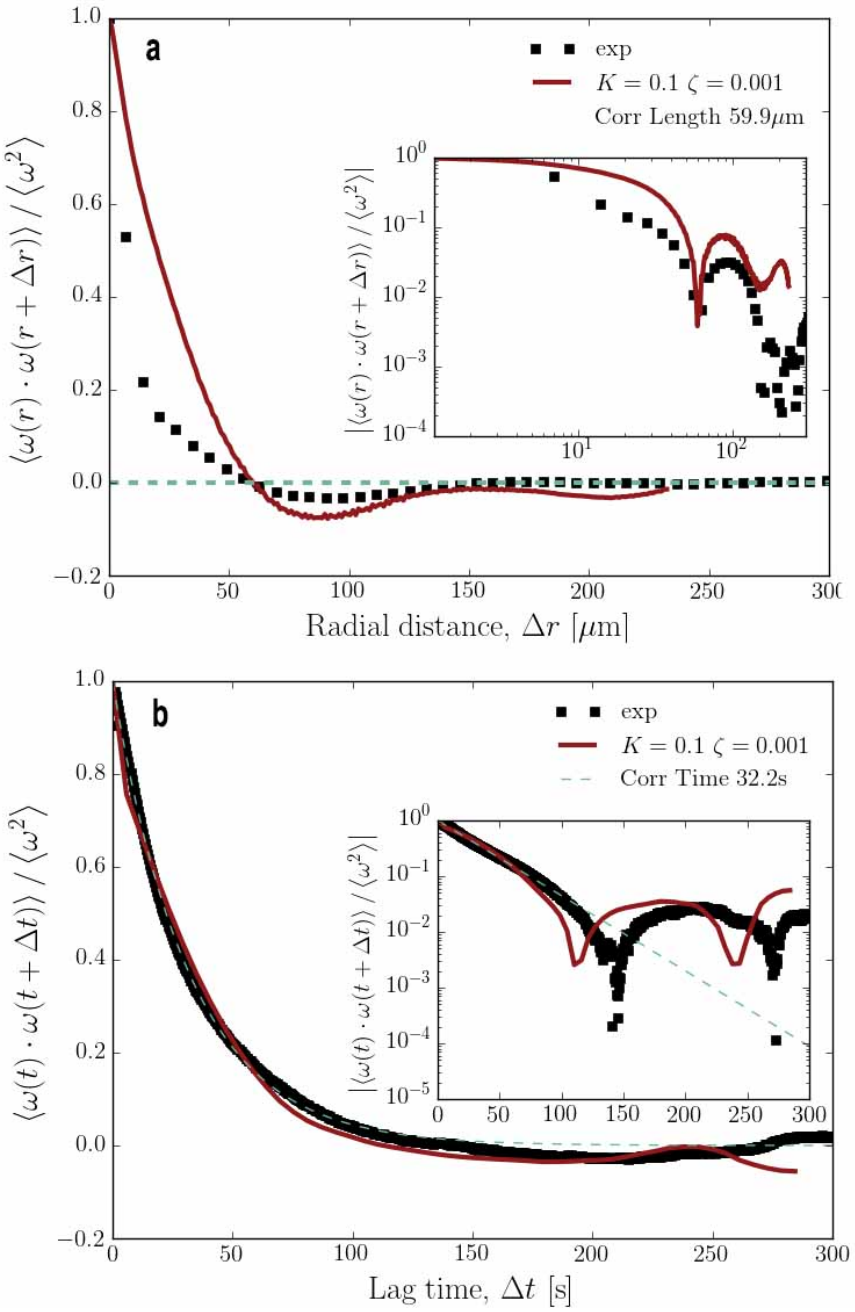

Figure 3.8: The vorticity auto-correlation functions for experiments (black squares) and hybrid-LB simulations (red lines). Panel (A) shows the same-time spatial auto-correlation function and panel (B) shows the temporal auto-correlation function. The simulation parameters used are $\gamma = 3 \times 10^{-4}$ and $\lambda = 0.3$.

merical results to physical units. We converted simulation length and time scales to the experiments by comparing decorrelations within the experimental and simulated vorticity fields. To determine the length unit conversion we matched the zero crossing point of the spatial vorticity auto-correlation function (Fig. 3.8(a)). Experimentally, the correlation length measured in this way is 60 μm. Positive correlation appears more pronounced in the idealized simulations in the near field, as do anti-correlations in the intermediate range. In our case, fitting the zero crossing point reproduces the extent of the anti-correlation range. This produces the conversion of 1 su : 2.38 μm.

The unit time conversion is determined by fitting an exponential decay to the short-lag region of the temporal vorticity auto-correlation function (Fig. 3.8(b)). The experimental correlation time is found to be approximately 30 s. This is seen to produce good agreement, both in the short-lag positive correlation and in the intermediate-time anti-correlation. This produces the conversion of 43.7 su : 1 s. We use these length and time units for the simulations presented in the main text. These conversions are for a specific experimental activity and oil layer thickness — we expect them to vary slightly for different experimental realizations.

3.5.4 Characterization of Nematic Order

3.5.4.1 +1/2-Defect Orientation Pair Correlation Function

Figure 3.9 displays the orientation correlation function between +1/2 defects in an active nematic film as a function of the separation Δr of the defects. The correlation function is defined as the average value of the dot product of the orientation unit vectors, $\langle \hat{\psi}(0) \cdot \hat{\psi}(\Delta r) \rangle$. Nearby +1/2 defects tend to be anti-aligned, as seen by the negative values of the correlation function at small separations.

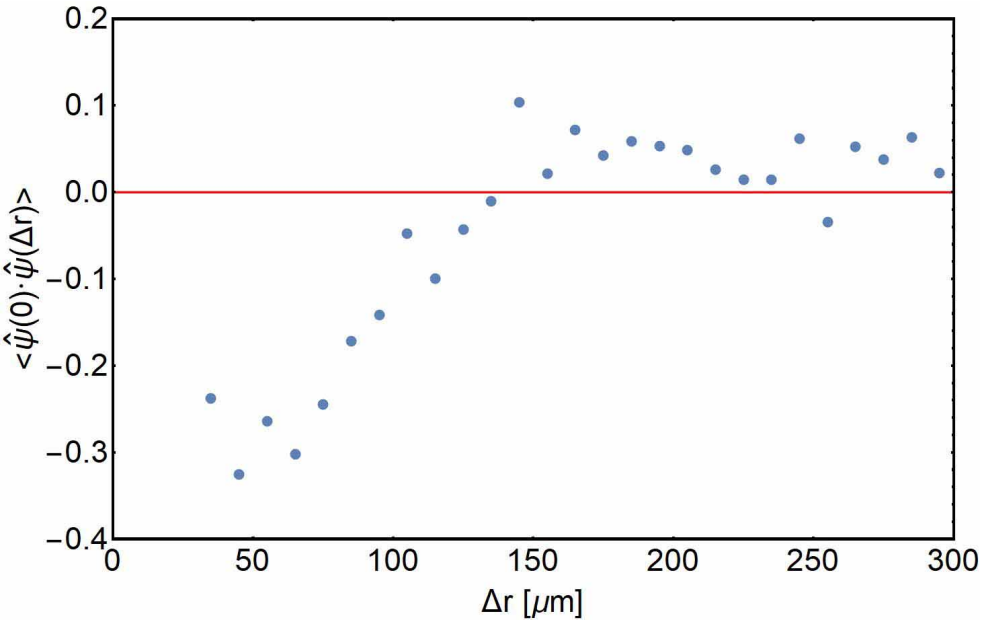

Figure 3.9: The orientation correlation function of +1/2 defects as a function of defect separation Δr. The negative values at short separations indicate that nearby +1/2 defects tend to be anti-aligned.

3.5.4.2 Nematic Correlation Length

Figure 3.10 displays a time and spatial average of the nematic director correlation function, defined as $\langle(\hat{n}(0)\cdot\hat{n}(\Delta r))^2\rangle$, obtained from analyzing a video of an active nematic film spanning 12 minutes and covering a field of view of 570 μm $\times$ 570 μm. Due to short-range nematic ordering in the active nematics, the correlation function is positive at small separations. For random relative orientations of the director, the average value of the correlation function is 0.5, which is the value reached at large separations. At intermediate separations of approximately 120 μm, the correlation function drops below 0.5. We identify the nematic correlation length, shown by the vertical dashed line in the Fig. 3.6, as the location of the minimum of this region. This distance also roughly equals the average separation between defects ($\sim$130 μm).

3.5.5 Image Analysis Details

3.5.5.1 Determination of Speed and Vorticity of the Flow in the Active Nematic Films

To quantify the velocity and vorticity in the active nematic films as shown in Fig. 5, we employed particle image velocimetry (PIV) techniques [145] to measure the displacement of microtubule bundles in subsections of the film between adjacent video frames. These results were binned and averaged by distance relative to the center of the disk, as determined by the mean location of the disk in the image pair

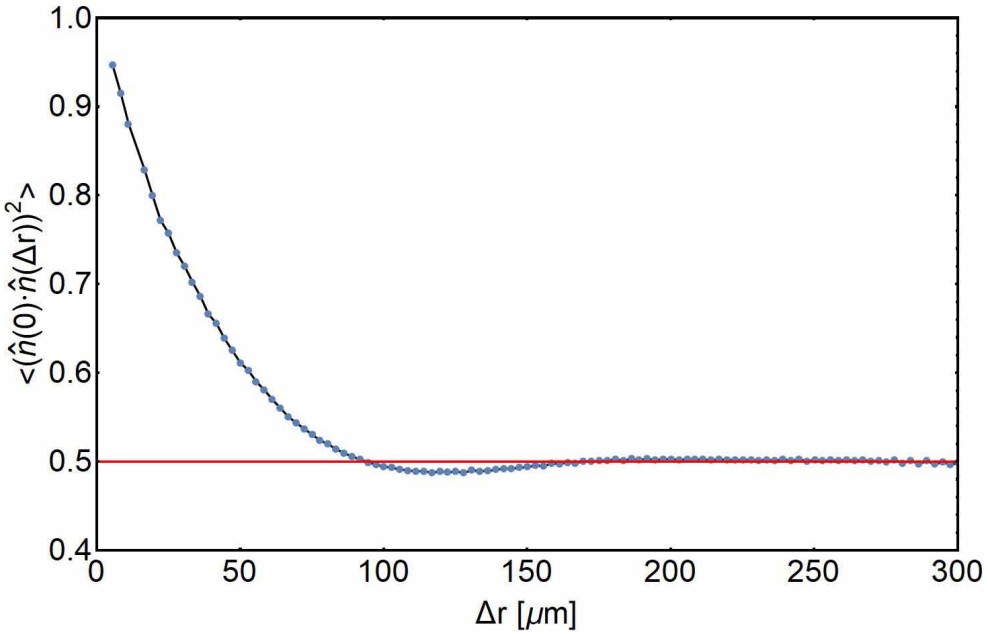

Figure 3.10: The nematic correlation function, defined as the average of the squared dot product of the director at positions separated by Δr. The results shown are obtained from averaging over a movie of 12 minutes in duration.

to produce the results shown in Fig. 3.6(a) and (e).

3.5.5.2 Quantifying Vortex Decay Dynamics

The decay of a topological vortex proceeded by the circularly symmetric director field around the defect core elongating into an elliptical shape in which two +1/2 defects oriented toward each other (*i. e.*, with each defect orientation vector ψ pointing toward the other defect) could quickly be identified. To characterize the time evolution of the decay process, we tracked this elongation and then the trajectories of the +1/2 defects by hand using the image processing program ImageJ. An example pair of trajectories is shown in Fig. 3.11. The inset shows the distance between the

+1/2 defects as a function of time. The specific decay time in which the +1 vortex is replaced by two well-defined +1/2 defects is not clearly defined, but was about 5 s after the start of the elongation into an elliptical director field. In Fig. 3.12 we plot five additional examples of the separation distance of +1/2 defect pairs produced in topological vortex decays versus time. The speeds of the +1/2 defects as they propagated away from one another were not measurably different from the typical speeds of the +1/2 defects in the film moving solely as a consequence of the activity.

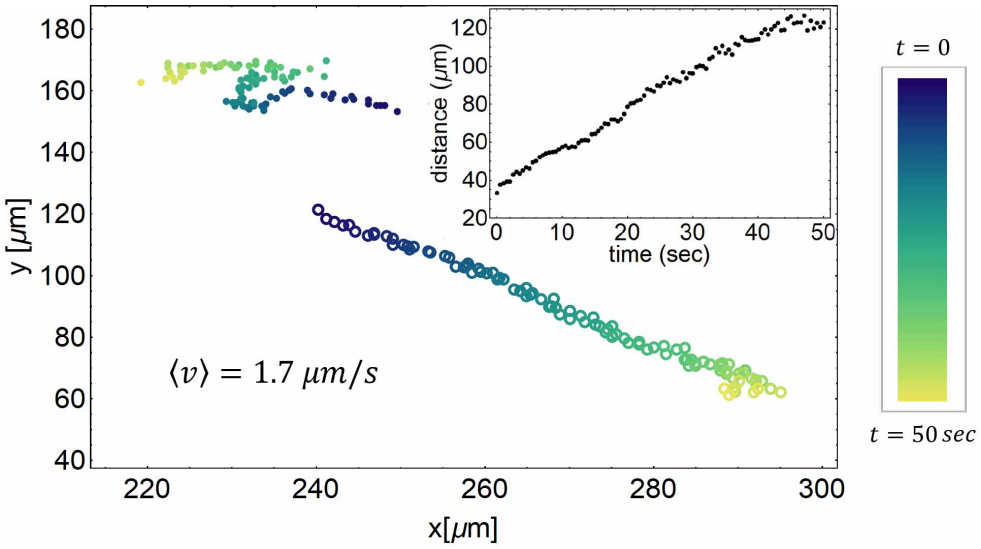

Figure 3.11: Example trajectories of the vertices of the collapsing elliptical +1 topological structure and the subsequent +1/2 defects. The inset shows their separation versus time. The average speed at which the two features separated was about 1.7 μm/s. For comparison, the average speed of the +1/2 defects in the film was 1.7 $\pm$ 0.5μm/s.

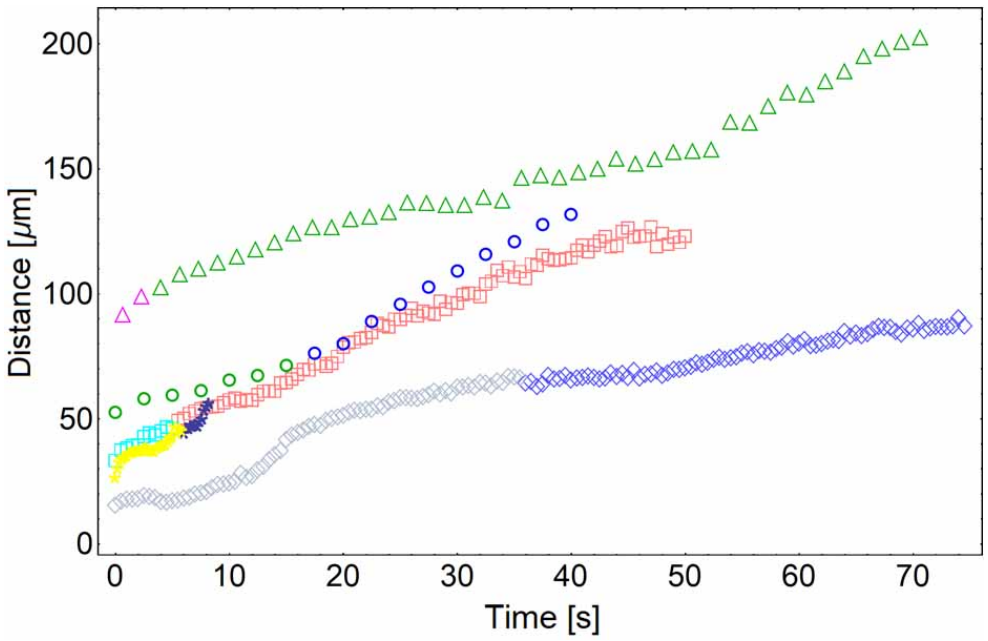

Figure 3.12: Distance between ends of the collapsing vortices as a function of time for several cases of vortex decay. The change of color of the data points indicates the approximate time at which the elongating +1 topological object became two distinct +1/2 defects.

3.5.5.3 Characterization of the Velocity Profile around a Topological Vortex

Individual microtubule bundles in the vicinity of vortices were tracked using the custom Python code Trackpy [3], which after thresholding found the centroids of the brightest connected features in each image. These features were then linked using Trackpy's link algorithm. The trajectories were hand filtered to select only the region of active nematic with director oriented azimuthally about the vortex. The distance of each feature from the vortex core was determined, and the measured speeds of features were averaged over bins of size 10 μm, resulting in the red data points in Fig. 3.7. The

blue data points in the same figure were produced using a similar method, however, since no topological vortex was present, no filtering of the trajectories was performed. The uncertainties were found by calculating the standard error of the mean of the ensemble average in each bin. Averages of the speeds of each feature were taken rather than an overall average in order to limit the effect of correlations in the data which could skew the mean and underestimate the uncertainty.

3.5.6 Estimate of Stress on Active Nematic Film from Rotating Disk

Estimates of the hydrodynamic stress imposed on the film by a disk rotating in the water layer above the film were performed using COMSOL's Computational Fluid Dynamics module. As an example, Fig. 3.13 displays the stress at the film surface as a function of horizontal distance r from the disk center computed for a 40 μm-diameter disk positioned 35 μm above the film and rotating at 80 Hz. The surface of the rotating disk imposed a no-slip boundary condition creating a shear flow in the water, and due to the large difference in viscosities between the water and film, we approximated the film as a stationary surface that also imposed a no-slip boundary condition on the water's flow. As shown in the inset, the stress decays as r^{-4} at large r, while at small values of r corresponding to the film directly under the disk, the stress increases linearly with r.

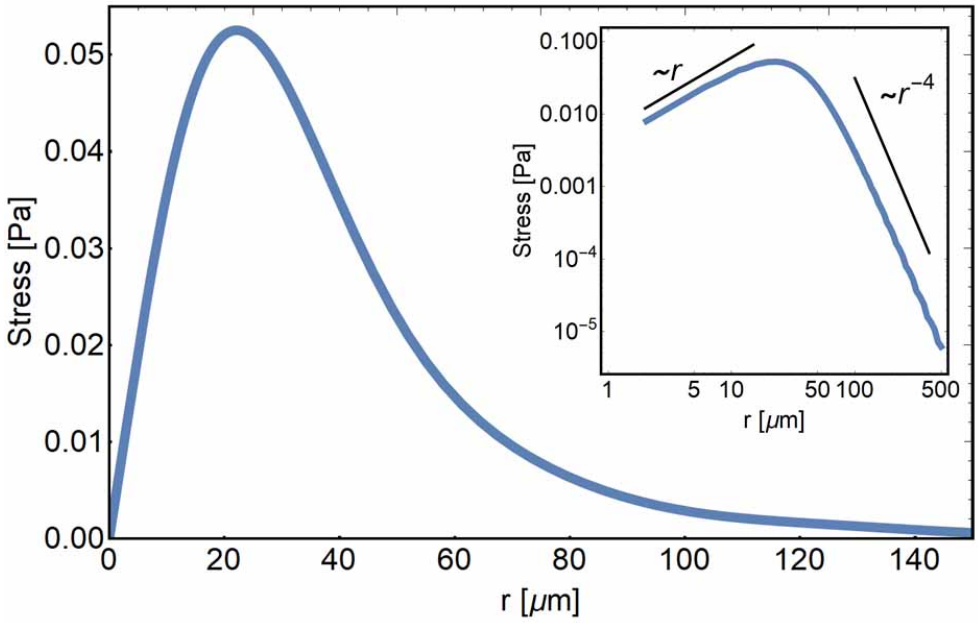

Figure 3.13: Computed stress on a film surface due to shear flow in the adjacent water created by a 40-μm-diameter disk rotating at 80 Hz at a height of 35 μm above the film, plotted as a function of distance r from the center of the disk. The inset shows the stress on a log-log scale.

3.5.7 COMSOL Calculations of Velocity Profile around a Vortex

As discussed in Sec. 3.3 of the manuscript, a region of the film in vicinity of the rotating disk experienced a large increase in flow velocity upon formation of a +1 topological vortex (see Fig. 3.7). To model this flow profile, we performed hydrodynamic calculations numerically using COMSOL's Computational Fluid Dynamics module. The calculations mimicked the experimental geometry of a disk rotating in a fluid with the viscosity of water (10^{-3} Pa·s) at a set height (35 μm) above a film of thickness 300 nm and viscosity η_f, which was varied in the calculations to optimize

the agreement with the experimental velocity profile. The space below the film was similarly treated as a fluid with viscosity matching that of the oil in the experiments (10^{-3} Pa·s). Several thicknesses for the oil layer were tested in the calculations, and the resulting velocity profile in the film was insensitive to the layer thickness as long as it was greater than ≈ 1 μm. Since the region of enhanced film velocity in the experiments typically coincided with the region of active nematic centered on the disk in which the director field was oriented in the azimuthal direction, we modeled the film as a circle of radius R matching the size of this region. As a boundary condition we set the velocity at the edge of the circle equal to the experimentally measured speed of the surrounding active nematic (approximately 1 μm/s). Over the lifetime of a vortex, the region of azimuthally oriented director field typically fluctuated. For example, for the vortex analyzed to produce the velocity profile in Fig. 3.7, R varied between approximately $R = 60$ μm and $R = 90$ μm during the measurements. Therefore, we calculated velocity profiles in films with R ranging from 60 to 90 μm and took the average of these curves to compare with the data. This process was repeated for different values of η_f to find the optimal agreement with the experimental data. For instance, Fig. 3.14 shows a set of curves that were averaged to produce the calculated curve shown in Fig. 3.7.

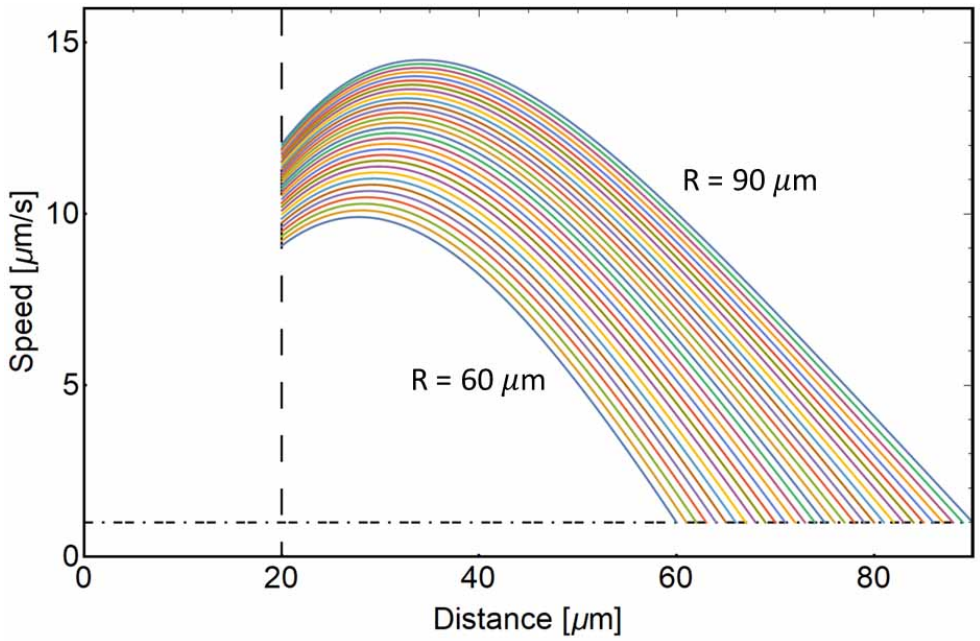

Figure 3.14: Calculated fluid velocity in a circular region of film as a function of distance from the center of the disk for a range of circle radii from 60 to 90μm in steps of 1μm. There is a boundary condition of v = 1μm/s at the outer boundary (shown by the horizontal dot-dashed line). The vertical dashed line represents the radius of the disk. These example velocity profiles were calculated using the same parameters that produced the calculated curve shown in Fig. 3.7 of the main text.

3.5.8 COMSOL Simulations of a Rotating Disk Near a Fluid Layer

In order to gain a greater sense of the hydrodynamics associated with a rotating disk near a fluid layer, below we describe results from COMSOL fluid dynamics simulations for disks of various distances from the layer and for various viscosities of the fluid layer.

Objects near a stationary wall experience drag forces due to the velocity gradient that occurs between the object and the wall. Similarly, the drag torque on a rotating

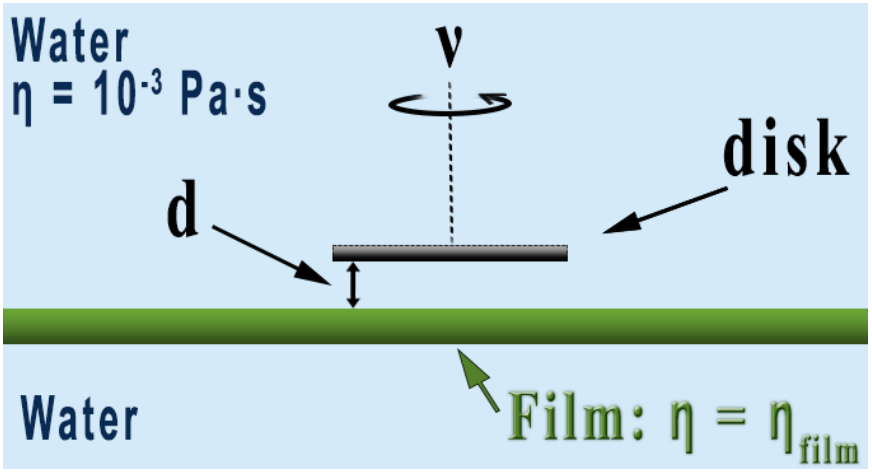

Figure 3.15: A schematic of the system. A disk rotates in water at a frequency ν at a height d from the surface of a fluid layer of viscosity η_{film}. The rotating disk creates azimuthal flows in the water, which creates a viscous stress on the film, inducing azimuthal flows within the film as well. The presence of the fluid layer also causes an increase in viscous drag on the disk.

disk near a fluid film layer (see Fig. 3.15) will be influenced by the presence of the layer. The disk, rotating at a frequency ν, creates azimuthally directed flows in the water which imposes a viscous stress on the film beneath. This stress results in azimuthal flows in the film which depends upon the viscosity of the film. The presence of the film also results in an increase in the drag torque on the rotating disk.

Figure 3.15 shows a schematic of the simulated system. We conducted fluid dynamics simulations using a computational fluid dynamics package in the software COMSOL. The normal of the disk's surface is parallel to the normal to the wall. We assume a no-slip boundary condition of the surface of the disk and the film and we take the fluid layer in the film to be Newtonian. The disk was rotated at a frequency of ν =80 Hz and has a diameter of 40μm. The film has a thickness of 300 nm and its

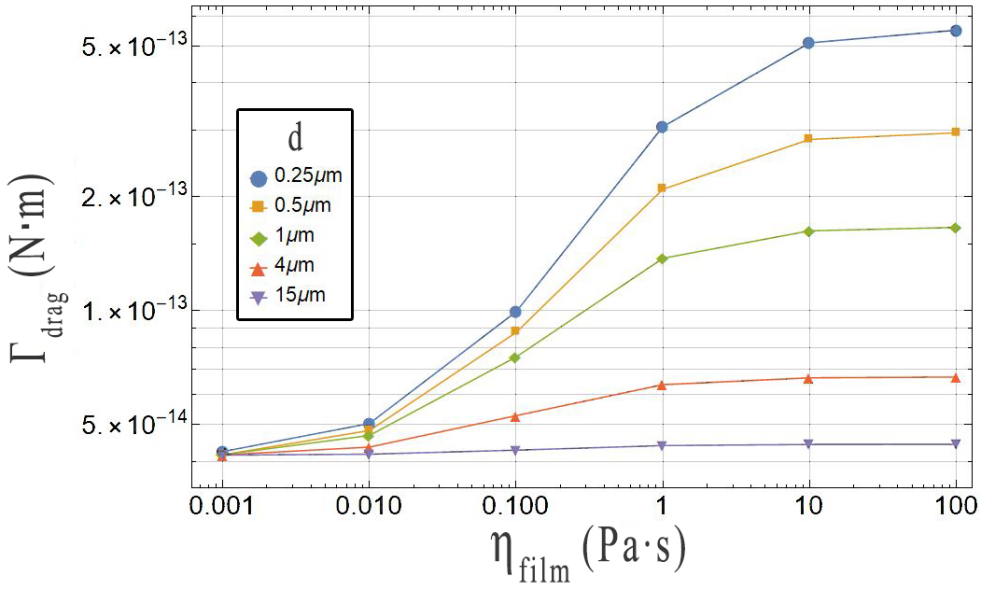

Figure 3.16: Calculated drag torque on a disk of diameter 40 μm rotating in water at 80 Hz at a distance d from a fluid layer of viscosity η_{film}. At distances greater than about 15 μm, the disk experiences a torque similar to that in just water in the absence of the film. For values of the film viscosity $\eta_{film} \gg \eta_{water}$, the film acts as a stationary wall.

viscosity is varied from 10^{-3} Pa·s (approximately equal to that of water at standard temperature and pressure) to 100 Pa·s. The calculated drag torque on the disk is shown in Fig. 3.16 for various values of the height, d, of the disk above the film.

For distances d greater than about 15 μm, the drag on the disk is similar to that of a disk rotating in water in the absence of the film ($\approx 4.2 \times 10^{-14} N \cdot m$) for all values of η_{film}. At smaller values of d, the drag on the disk increases with increasing viscosity of the fluid layer, until reaching a plateau at the largest values of η_{film}. This plateau can be associated with the case of infinite film viscosity, in which the film essentially behaves as a stationary substrate.

For small values of d and large values of η_{film}, one can show that the drag torque

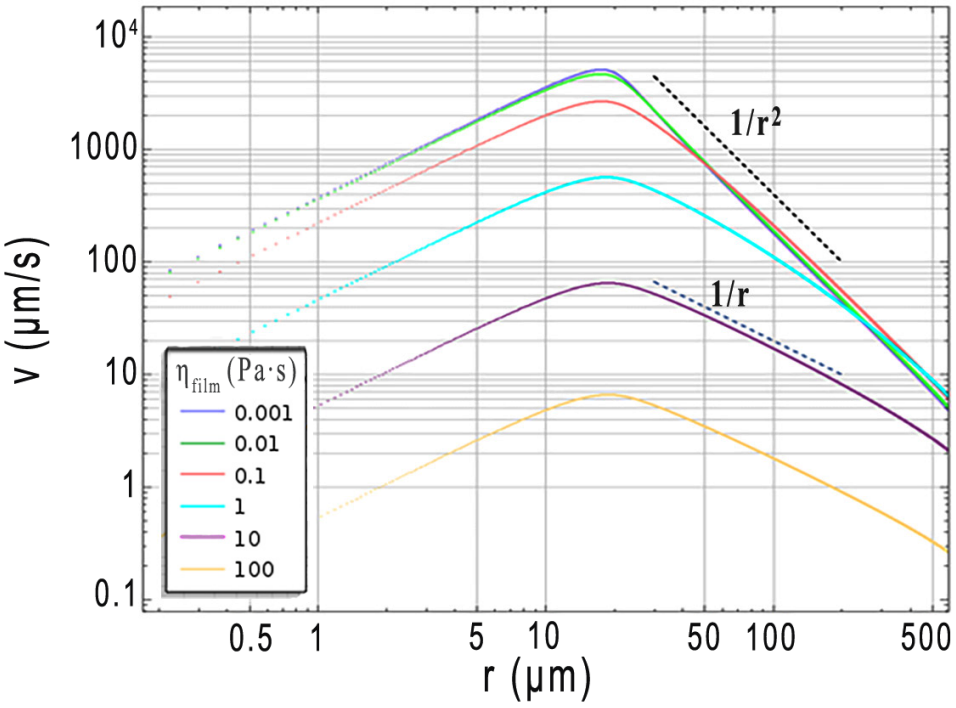

Figure 3.17: Calculated azimuthal velocity within a fluid film layer of viscosity η_{film} due to the imposed viscous stress created by a rotating disk of radius 20 μm at a distance 4 μm from the film. For large film viscosities, the velocity within the film falls off as $1/r$, indicating the quasi-2D hydrodynamics of the film at this relatively large viscosity. For viscosities close to that of the bulk phase, the velocity falls off as $1/r^2$, similar to the case without the presence of the film. The thickness of the film is 300 nm.

on the bottom of the disk is approximately $\Gamma_{drag} = \frac{\pi^2 \nu R^4 \eta_{water}}{d}$, where R is the radius of the disk. As an example, plugging in the values used in the simulation for $d = 0.5\mu$m and $\eta_{film} = 100Pa \cdot s$, gives $\Gamma_{drag} = 2.5 \times 10^{-13} N \cdot m$, only slightly less than the simulation result of about $3 \times 10^{-13} N \cdot m$.

The rotating disk also creates a viscous stress on the film which results in an induced azimuthal flow. Figure 3.17 displays the simulated azimuthal velocity within the film for a 40 μm diameter disk rotating at 80 Hz at a distance of 4 μm from the

film for a range of film viscosities, η_{film}. The velocity in the region of the film directly beneath the disk increases approximately linearly with distance. For greater distances from the disk, and when $\eta_{film}/\eta_{water} < 100$, the velocity decays approximately as $1/r^2$, as expected in a 3D system. In the case of large film viscosity, $\eta_{film}/\eta_{water} \geq 1000$, the velocity within the film decays approximately as $1/r$, as expected for a 2D system. One can understand this transition between 2D and 3D behavior in the film by the associated Saffman-Delbrück length, $L_{SD} = \frac{\eta_{film} h}{2\eta_{water}}$, which determines the length scales over which the film behaves as a 2D system, where h is the thickness of the film [152]. For example, the cyan curve in Fig. 3.17 corresponds to $L_{SD} = 150$ μm, which is approximately where the velocity transitions from $1/r$ to $1/r^2$ decay. The peak velocities within the film for $\eta_{film}/\eta water \geq 1000$ decrease approximately linearly with increasing film viscosity. This can be understood by considering that the torque on the film directly beneath the disk imposed by the disk is approximately equal to the drag torque on the bottom of the disk found above, $\Gamma = \frac{\pi^2 \nu R^4 \eta_{water}}{d}$. Balancing this with the viscous drag on the film at $r = R$ produced by the film itself, gives $v(r) = \frac{\pi \nu R^4 \eta_{water}}{4rdh\eta_{film}}$, where h is the film thickness. This approximate solution for the velocity magnitude within the film indicates that it decreases inversely proportionally with increasing film viscosity, film thickness, and distance from of the disk from the film, while increasing approximately linearly with the rotation rate of the disk. This approximation assumes that the stress increases linearly with distance up to $r = R$ and then is zero beyond this value. In reality, the stress is continuous in

nature (see, for example, Fig. 3.13) and, consequently, the velocity within the film around $r = R$ has a more rounded appearance.

Chapter 4

Coupling of Colloidal rods to the dynamic order of active nematic films

4.1 Introduction

As described in the previous chapters, active nematic films are a class of materials that combine the emergent properties of out-of-equilibrium active matter with the unique attributes of liquid crystals. A major experimental realization of an engineered active nematic is a film composed of dense packings of microtubular bundles driven by kinesin motors at an oil-water interface. The bundles align with one another, endowing the films with nematic order characterized by a director field $\hat{n}(\mathbf{r})$, and

slide along one another due to forces generated by the molecular motors. This sliding motion creates extensional strains in the films that drive bend instabilities in $\hat{n}(\mathbf{r})$ and ultimately lead to turbulence-like flows. The instabilities also cause spontaneous creation of pairs of $\pm 1/2$-charged topological defects in the nematic order, and the extensional strains endow the $+1/2$ defects with characteristic velocities, so that they act as self-propelled quasi-particles. Due to the symmetry of the director field around -1/2 defects, these defects behave as passive objects in the films, whose motion results primarily from the influence of the motile $+1/2$ defects. The defect pairs form and annihilate at an equal rate, creating a state of dynamic equilibrium in which the interface is populated with a time-averaged fixed density of defects.

The flow properties of active nematic films, which result from a complex coupling among the hydrodynamics, the nematic elastic distortion energy, and the active stress leads to behavior that is unexpected based on that of traditional, equilibrium liquid crystals. For example, the active forces can drive $+1/2$ defects away from -1/2 defects, overcoming their attractive elastic interactions. The extensional flows also result in an aligning hydrodynamic torque between adjacent filaments [64] that derives from the nature of flow field created by the extensional strain and that stabilizes the nematic order on short lengthscales. Indeed, films formed in the absence of ATP to fuel the molecular motors remain in a disordered gel state lacking nematic order. This hydrodynamic effect is similar to that in suspensions of swimming bacteria that create extensional flow by pushing fluid behind them as they swim. Such swimmers, which

are called "pushers", tend to align with their neighbors.

An important step in understanding active nematic systems is characterizing their activity-driven flows and the hydrodynamic forces they generate. Experiments have investigated the dynamics of active nematic films by measuring the shearing of fluorescently marked square regions of uniform nematic director, which undergo deformation due to extensional flows and diffusion, and by measuring flow velocity fields within the film by tracking fluorescently labeled microtubules [69]. Other experiments have sought to understand the dynamics of active nematic films in terms of their turbulent mixing and topological chaos [138]. Still other work has characterized the size distribution of vortices in the flow, the characteristic length scales of the nematic order, and the film speed as functions of activity, as controlled by the concentration of ATP [68]. Despite such studies, as well as the broader interest in better understanding the role of activity, hydrodynamics, and elasticity on the dynamics of the active nematics, much remains to be understood.

In this chapter, we study the dynamics and forces generated by active nematic films by tracking the motion of microscale magnetic rods that are positioned adjacent to the films. We observe that the rods undergo translational motion that follows the flow of the film in their vicinity while maintaining alignment with the local nematic director. Taking advantage of this behavior by employing the rods as tracers, we gain a novel perspective on the spatial and temporal properties of the nematic order and its coupling to the flow dynamics in the film. Further, by rotating the rods away

from alignment with the director using external magnetic fields and tracking rotational dynamics after the field is removed, we characterize the hydrodynamic torques generated by the flows in the active nematic. The results of these two studies are described in Sec. 4.3 below. First, in Sec. 4.2 we provide details about the experimental procedures. Finally, in Sec. 4.4 we discuss the findings and give some concluding remarks.

4.2 Materials and Methods

The experiments employed both ferromagnetic nickel rods (370 nm average diameter and typically 30 μm in length) and superparamagnetic rods (250 nm average diameter and similar in length) composed of iron oxide nanoparticles in a polymer matrix. The ferromagnetic rods possessed a permanent magnetic moment parallel with their axis that was proportional to their length and was approximately $3 \cdot 10^{-13}$ A/m^2 for a 10-μm-long rod. They were fabricated using an electrochemical deposition technique described in Chapter 2 and elsewhere [139]. The superparamagnetic rods, which were kindly provided by J.-F. Berret of University of Paris Diderot, possessed an anisotropic magnetic susceptibility that caused them to obtain an induced magnetic moment in applied magnetic fields. Details regarding the fabrication and properties of the superparamagnetic rods are described elsewhere [18, 22, 41].

The active nematic films were formed at an oil-water interface between two glass

slides that were separated by an adhesive tape and sealed with an optical adhesive, as described in Chapter 3. The films were composed of a dense layer of fluorescent microtubule bundles driven by kinesin molecular motors fueled by ATP [117]. The materials to fabricate the films were provided by the Brandeis University Materials Research Science and Engineering Center Biological Materials Facility. The magnetic rods were added to the active gel by vortex mixing prior to introduction of the gel into the glass sample chamber. The sample was centrifuged for 10-15 minutes at 800 rpm (103 g), causing the microtubule bundles to sediment to the oil-water interface to form a quasi-two-dimensional, nematic layer. During the centrifugation the rods also sedimented, but did not embed within the film. Instead, they became positioned adjacent to the film in the aqueous phase with rod axes parallel to the film. More precisely, the rods became positioned a small distance (< 5 μm) above the film. We attribute this separation to a thin, dilute layer of unadsorbed microtubules adjacent to the interface. The concentration of rods was kept sufficiently small to prevent aggregation and to assure that magnetic interactions between rods were negligible.

Observations of the rods and films were performed on an inverted microscope (Nikon TE2000) using a Flare CameraLink camera (IOIndustries) operating at 1-3 frames per second. Both bright-field and fluorescence microscopy measurements were performed. Four pairs of solenoids mounted on the microscope [66] generated time varying magnetic fields of specified magnitude from 10-80 Gauss in arbitrary directions in the plane of the film. The image analysis methods described in Chapter

2 were employed to determine the time-dependent rod position and orientation and nematic director field.

4.3 Results

We observed that rods positioned adjacent to the active nematic films translated with the active flows seemingly with the same velocity as the film directly below them, implying a strong hydrodynamic coupling between the rods and films. As they translated, the rods rotated to maintain alignment with the local director. Figure 4.1 shows a series of images of a rod translating and rotating along with an active nematic film in this way. To characterize this alignment quantitatively, we tracked the orientation of the rods as well as the orientation of the local director in the vicinity to the rod (averaged over an area small enough that the director was essentially uniformly oriented over the analyzed region). Fig. 4.2 displays results of such a measurement conducted over an approximately two-minute period during which the rod followed a trajectory set by the underlying active flow of several hundred micrometers in length. The orientation of the rod axis and local director are specified in terms of the angle θ that each makes with horizontal axis of the microscopy images.

This tendency of the rods to translate with the flow of the film while maintaining alignment with the local director can be understood from the rods' close proximity to the film and to the flows created in the bulk aqueous phase by the film. If the

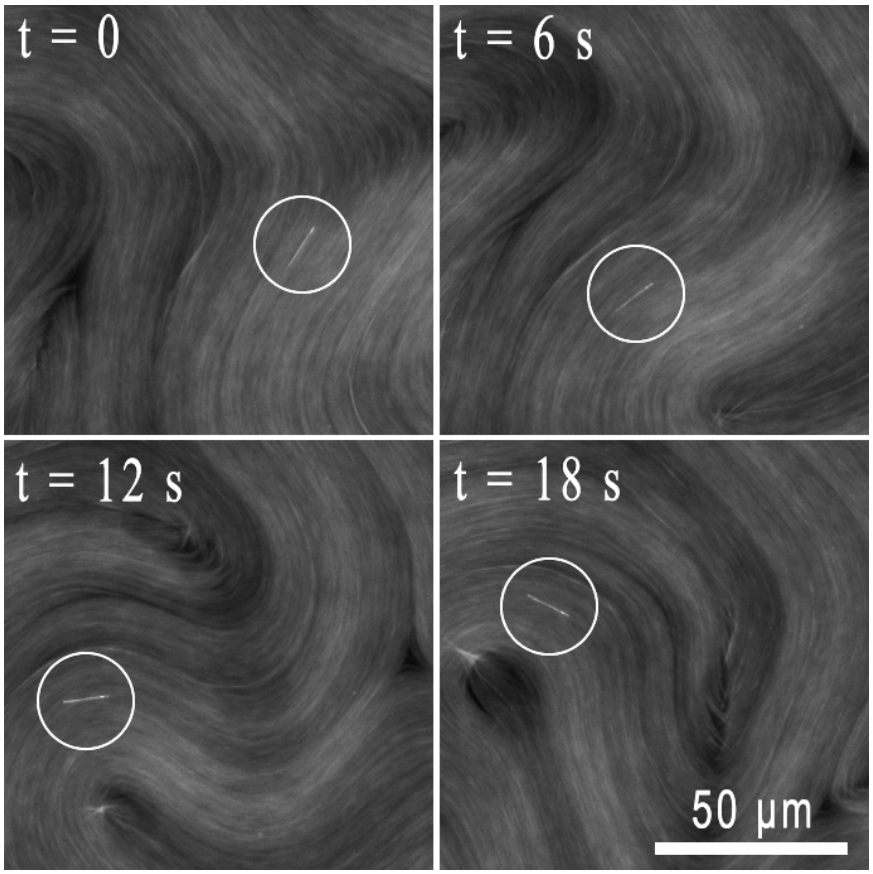

Figure 4.1: Sequence of fluorescence microscopy images showing magnetic rod (circled) in close proximity to a active nematic film. The rod aligns with the local director and follows the flow of the film.

active nematic film acts as a substrate that imposes a no-slip boundary condition on the water, the motion in the film sets up shear flows in the water with velocities that match those of the film at the film surface and that decay to zero at the confining glass substrate. Since the rods are much closer to the films than to the glass, they reside in a region of water that has a velocity $\vec{v}(\mathbf{r})$ essentially matching that of the nearby film and move passively in this flow. However, since the rods are extended objects and the film velocity is spatially varying, $\vec{v}(\mathbf{r})$ has both an average over the rods that dictates their translational velocity and gradients that cause torques leading to the alignment with the director. In the sections below, we exploit this coupling between the rod and active nematic film to make two sets of observations. First, we employ the rods as tracers to characterize correlations in the nematic order. Second, we characterize the rotational dynamics of the rods to elucidate the hydrodynamic torques created by the active flows.

4.3.1 Correlations in nematic order

The chaotic flows of active nematic films have a complex spatio-temporal structure whose similarities to hydrodynamic turbulence have led to their being described as "active turbulence". Experimental and simulation efforts to describe this dynamical behavior have introduced a number of correlation functions based on the position-dependent flow velocity and director field in the films. The tendency of the rods to translate with the local flow velocity of the film while maintaining alignment with

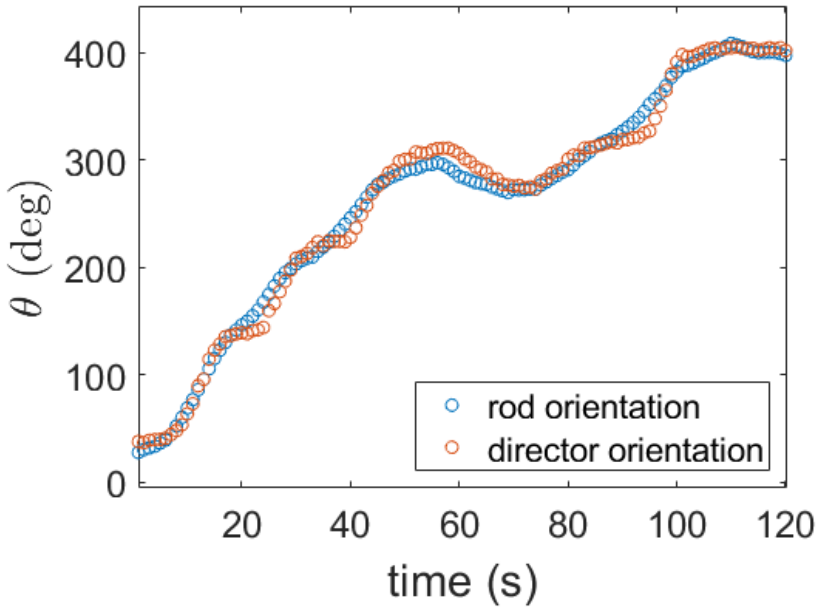

Figure 4.2: The orientations of a colloidal rod and the director of an active nematic film in proximity to the rod as functions of time. The rod orientation tracks the local director as the film flows and director reorients.

the local director provides a new perspective from which to characterize the relationship between flow and nematic order. Specifically, we define a time auto-correlation function for the director in close proximity to the rod as,

$$c_n^c(t) = 2\langle(\hat{n}(\mathbf{r}_r(t+t')) \cdot \hat{n}(\mathbf{r}_r(t'))^2\rangle_{t'} - 1/2 \tag{4.1}$$

where the average is taken over measurement time t', $\mathbf{r}_r(t')$ is the position of the rod, the square of $\hat{n} \cdot \hat{n}$ is taken due to the symmetry of $\hat{n}$ with respect to rotations of 180°, and the superscript "c" signifies that the correlation is taken between points in space given by the time-dependent position of the rod, which travels with the active flow, and hence can be considered a "convective" correlation. In terms of the angle θ, the correlation function is $c_n^c(t) = 2\langle cos(\theta(t) - \theta(0))^2\rangle - 1/2 = \langle cos(2(\theta(t) - \theta(0)))\rangle$.

Perfect anti-correlation, *i.e.*, $c_n^c = -1$, corresponds to changes in orientation of 90°, while random relative orientations correspond to $c_n^c = 0$.

Fig. 4.3(a) displays an example of the convective correlation obtained from a measurement spanning 120 seconds in which a wire of length 12 μm was tracked. As the figure illustrates, the convective correlation oscillates as a function of lag time with a first minimum at $\tau_m = 18$ s. This behavior can be contrasted with that of a correlation function characterizing the time-dependent director orientation at fixed points in space,

$$c_n^s(t) = 2\langle(\hat{n}(\mathbf{r}, t+t') \cdot \hat{n}(\mathbf{r}, t')^2\rangle_{t',\mathbf{r}} - 1/2, \tag{4.2}$$

where the director is evaluated at stationary positions $\mathbf{r}$ by averaging the orientation in square windows of size ≈ 5.5 μm throughout the image, and the superscript "s" signifies this as a "stationary" correlation function. Fig. 4.3(a) displays $c_n^s(t)$ calculated from the same video from which $c_n^s(t)$ was obtained. As the figure shows, $c_n^s(t)$ decreases monotonically to a value near zero and is well fit by a exponential decay with a correlation time $\tau_s = 7.5 \pm 0.8$ s.

The oscillatory behavior of the convective correlation is perhaps surprising given the notion of active turbulence. In particular, the robust magnitude of $c_n^c(t)$ over more than a full period of oscillation points to a regularity in the dynamics of the nematic director that is not apparent in other measures of the time-dependent order like $c_n^s(t)$. At short times, $c_n^s(t)$ and $c_n^c(t)$ track each other, and while $c_n^c(t)$ is not as well fit by an exponential decay as $c_n^s(t)$, it similarly falls to $1/e$ at $t \approx 8$ s. This

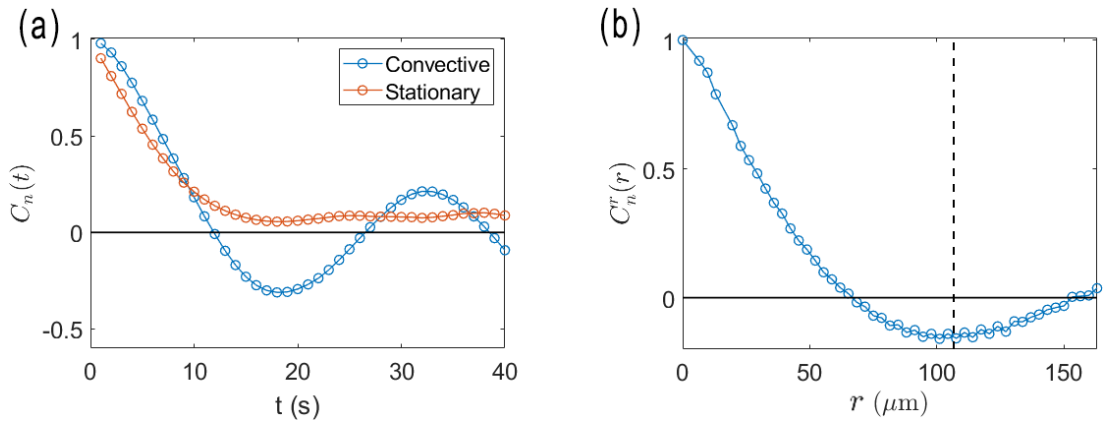

Figure 4.3: Temporal (a) and spatial (b) auto-correlation functions of the nematic director. In (a), the stationary temporal correlation function, averaged over fixed points in space, decays monotonically, whereas the convective correlation function, averaged over a location that follows the position of a rod in proximity of the film and translates with the active flows, contains oscillatory features in time. In (b), the spatial correlation function also decays non-monotonically and reaches a minimum below zero. The vertical dashed line indicates the approximate defect-defect spacing. The data for the convective correlation was obtained by tracking a rod of length 12 μm for 120 s. The stationary and spatial correlation function were found from an average over a subset of 80 s, while convective correlation was found from an average over 120 s. The dimensions of the image were 226×169 μm.

similarity indicate that the characteristic time scales of both functions are set by the same dynamical properties of the film. However, the stochasticity that one might infer from the exponential decay of $c_n^s(t)$ belies a more persistent memory in the dynamics that tracking material elements like with $c_n^c(t)$ reveals.

Insight into the structure of $c_n^c(t)$ and $c_n^s(t)$ can be found in examining the equal-time spatial correlations in director field characterized by

$$c_n^r(r) = \langle cos(2(\theta(r) - \theta(0))) \rangle \tag{4.3}$$

Figure 4.3(b) shows $c_n(r)$ obtained from the same video as the time correlations shown in Fig. 4.3(a). The spatial correlations show an initial decay that can be fit to exponential function to give a correlation length of $\xi = 43 \pm 5$ μm. The correlation does not decay monotonically, however, and reaches a minimum below zero at approximately $d_m = 101$ μm. For comparison, the approximate defect-defect separation of the positive defects in the film was 107 μm. We find, based on several trials, that the defect-defect separation is approximately equal to the location of the minimum in $c_n^r(r)$. Dividing the characteristic distances, ξ and d_m, by the characteristic times, τ_s and τ_m, gives characteristic speeds, $v_s = \xi/\tau_s \approx 5.7$ μm/s and $v_c = d_m/\tau_m \approx 5.6$ μm/s. As a comparison, we measured the average speed of the +1/2 defects to be 6.5 μm/s, the average speed of the -1/2 defects to be 2.9 μm/s, and the average speed of the rod to be 2.9 μm/s. Therefore, we interpret the time scales associated with the features in Fig. 4.3(a) to derive the time required for the +1/2 defects to move characteristic distances.

4.3.2 Hydrodynamic Torques on Rod

To investigate the mechanism behind the alignment of the rods with the local director, we applied magnetic fields to rotate the rods away from the director and then tracked the rods' orientations following removal of the field as the rods rotated back into alignment. Figure 4.4(a) shows an example of results from such measurement using a superparamagnetic rod of length 29 μm that was initially rotated approximately 80 degrees away from the director by a 15 G field. Specifically, the figure shows the angle $\Delta\theta$ between the rod axis and the local director as a function of time after removal of the field. The rod rotates monotonically toward the director and eventually aligns after about 25 seconds; however, the rate of decrease of $\Delta\theta$ is unsteady, in part because the director itself is reorienting during the measurement as a consequence of the flows in the active nematic.

Notably, the images reveal no measurable distortion of the director in the vicinity of the rod as a consequence of its field-driven misalignment. Thus, unlike the case of anisotropic colloids in thermotropic liquid crystals [61, 62, 112], the restoring torque aligning the rod and director appears not to result from the nematic elasticity. Instead, we hypothesize that the torques aligning the rods with the director result from a hydrodynamic coupling between the rods and extensile and shear flows in the water created by gradients in the velocity of the active nematic film beneath. Figure 4.5 (a) and (b) show examples of velocity fields that are purely extensile ($\mathbf{v} \sim (x\hat{x} - y\hat{y})$) and purely shear ($\mathbf{v} \sim y\hat{x}$), respectively. As an illustration of their presence in the

active nematic flows, Fig. 4.4(b) shows the time-averaged velocity field of the active nematic film in the vicinity of the rod during the measurement of the rod's rotation from Fig. 4.4(a). The velocities are shown in a reference frame in which the center of the rod is at the center of the plot and the local director is along the horizontal. Specifically, the video frames used in the analysis were first centered at the center of the rod and rotated such that the director was oriented along the x-axis. PIV measurements tracking features in the active nematic film were then conducted to determine the velocity field between adjacent frames, and the time average of the velocity at each position was obtained. As can be seen from the figure, the time-average flows have an extensile component where the film flows outward along the director and inward perpendicular to the director as a consequence of the activity. We can quantify the extension in the flow by the extensional rate, $\mathcal{E} = \frac{1}{2}(\frac{\partial v_x}{\partial x} - \frac{\partial v_y}{\partial y})$, which is shown by the color-map in Fig. 4.4(b). Positive values of $\mathcal{E}$ indicate extensional flows, whereas contractile flows are characterized by $\mathcal{E} < 0$. As expected for the active nematic, $\mathcal{E} > 0$ over nearly the entire field of view. The flow also has a shear component, as most evident in the top portion of the image, that can be quantified in terms of the shear rate, $\mathcal{S} = \frac{1}{2}(\frac{\partial v_x}{\partial y} + \frac{\partial v_y}{\partial x})$.

The combination of extensile and shear flows like those in Fig. 4.4(b) can result in rotation of the rods toward the director. In order to understand these effects quantitatively, we model the torque on a rod as arising from a coupling with the surrounding flow field, where we assume the fluid around the rod moves at the same

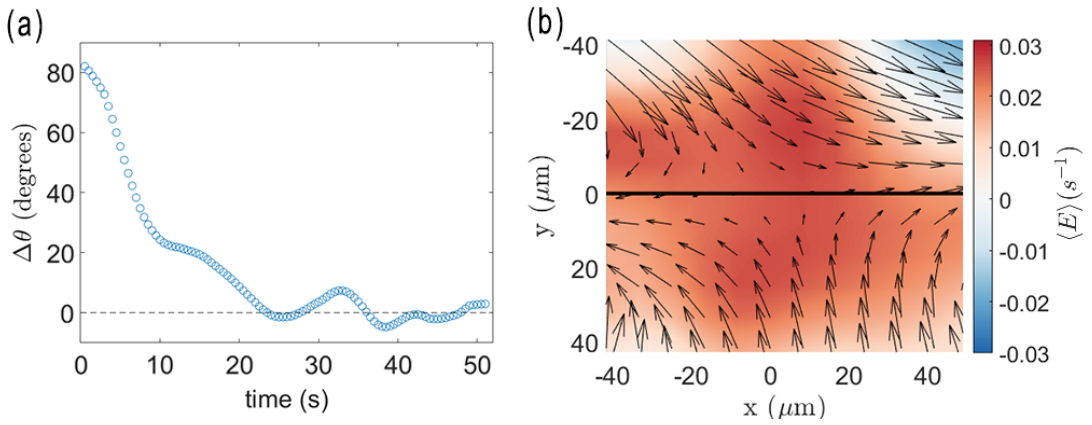

Figure 4.4: (a) The angle of a magnetic rod, length 29 μm, with respect to the local director as a function of time following removal of an applied 15 G field. (b) A colormap of the average extensional rate in a frame of reference in which the rod is at the center and the director is along the x-axis. The time-average velocity field is shown by the arrows.

local velocity as the film beneath. The torque $d\mathbf{\Gamma}$ on a segment of rod of length dr due to the fluid will be $d\mathbf{\Gamma} = \gamma \mathbf{r} \times \mathbf{v} dr$, where $\mathbf{r}$ is the vector from the center of the rod to a point along its axis, $\mathbf{v}$ is the velocity of the film relative to the velocity of the rod at that point, and γ is a drag coefficient that depends on viscosity. The total torque $\mathbf{\Gamma}$ on the rod can then be found by integrating these infinitesimal contributions along the length of the rod.

Because the PIV analysis does not provide a map of the film velocity with adequate spatial and temporal resolution to determine the time-dependent torque directly, we decompose the flow field to into three components – extension, shear, and solid rotation – and analyze the videos is the frame of reference illustrated in Fig. 4.4(b). In this reference frame, the rate of solid rotation is given simply by the time derivative of $\Delta\theta$, $\omega_r = d\Delta\theta/dt$, and the torque on the rod due to the solid rotation is $\Gamma_r = \gamma \frac{L^3}{12} \omega_r$,

where L is the length of the rod. The magnitudes of the extensional and shear rates are found by averaging over a small region of interest around the rod. Specifically, we obtain spatial averages of $\mathcal{E}$ and $\mathcal{S}$, which we call u_e and u_s, respectively, by averaging over a cropped region of dimensions 1-3 times larger than the size of the rod itself. In the example shown, the average was taken over a region approximately 60×60 μm^2. We found that this size was a good compromise between capturing the region whose flows most influence the rod's motion, while including the greatest amount of data as possible for the sake of statistics and also mitigating the influence of the rod's motion on the PIV analysis. These velocity fields were then used to determine u_e as a function of time, which is shown in Fig. 4.6(a). To obtain u_s further simplifications were applied. Although, in general, the shear flow includes a component from velocities perpendicular to $\hat{n}$, the anisotropy in the viscosity of the nematic gives strong preference for shear in film's flow parallel to $\hat{n}$. Hence, we focused on these contributions by averaging the velocity along $\hat{n}$ to obtain a velocity as a function distance from the center of the rod perpendicular to $\hat{n}$. A third-degree polynomial was then fit to the data and the derivative was taken at the center of the rod to determine the shear rate. Figure 4.6(a) shows the resulting u_s as as function of time for the example experimental trial.

The torque on the rod due to the extensional flow is found by integrating $d\Gamma$ along the length of the rod using the form for the extensional flow field, which leads to $\Gamma_e = -\gamma \frac{L^3}{12} u_e \sin(2\Delta\theta)$. Note, this torque is maximum at $\Delta\theta = 45^\circ$ and is zero

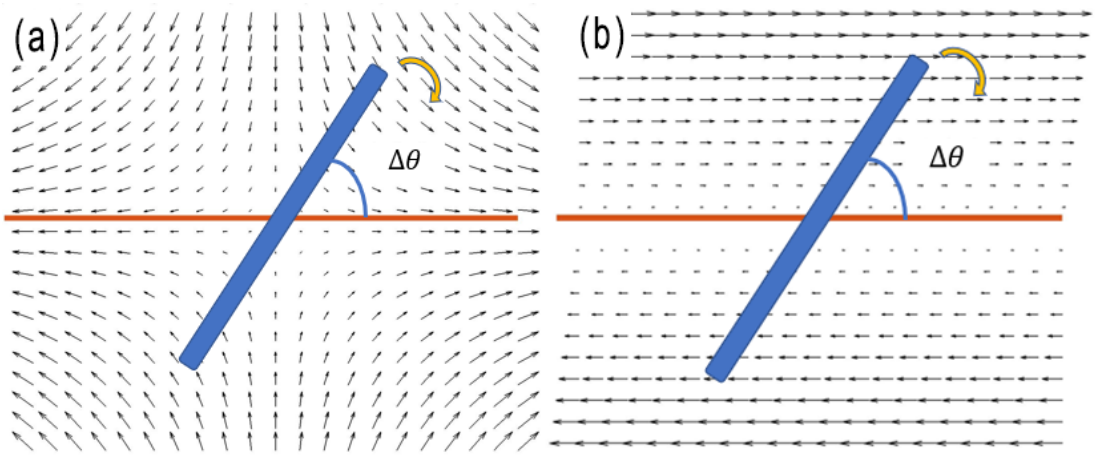

Figure 4.5: Example extensional and shear flow fields. The arrows indicate the fluid velocity. (a) An ideal extensional flow field. A rod experiencing this flow field rotates toward the director. (b) A shear flow field which, in this example, acts to rotate the rod clockwise.

for $\Delta\theta = 0°$ and $90°$. The torque on the rod due to the shear flow field is $\Gamma_s = -\gamma\frac{L^3}{12}u_s \sin^2(\Delta\theta)$. Note, in contrast, this torque is maximum for $\Delta\theta = 90°$ and is zero for $\Delta\theta = 0°$. These forms of Γ_e and Γ_s explain the tendency of the rods to remain aligned with the director. Specifically, for small values of $\Delta\theta$, $\Gamma_e/\Gamma_s \approx \frac{2u_e}{u_s\Delta\theta}$. We found that u_e and u_s are typically of similar magnitude; therefore, at small $\Delta\theta$, the torque from the extensional flows dominates. Further, because u_e is invariably positive due to the extensional strains inherent in the active nematic film, Γ_e always acts as a restoring torque to rotate the rod back into alignment with the director for small misalignments.

When the rod is misaligned with the director by larger values of $\Delta\theta$, it experiences the hydrodynamic torques derived above due to all three components of the flow: Γ_w,

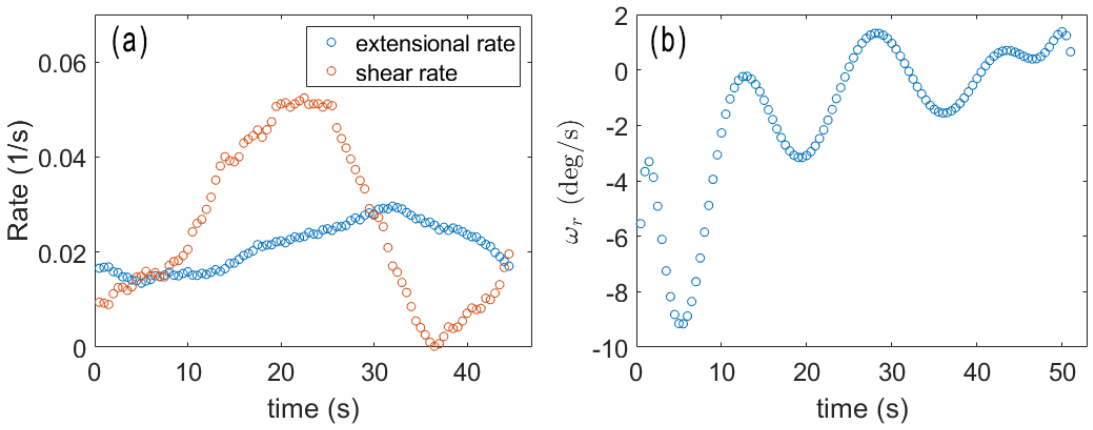

Figure 4.6: (a) The time-dependent extensional and shear rates in vicinity of the rod whose angle relative to the director is shown in Fig. 4.4. (b) The rotation rate of the rod relative to the director, as determined by fitting $\Delta\theta$ to polynomials and taking the derivative.

Γ_e, and Γ_s. Since the system is at low Reynolds number, these torques sum to zero,

$$\Gamma_r + \Gamma_e + \Gamma_s = \gamma\frac{L^3}{12}\omega_r - \gamma\frac{L^3}{12}u_e\sin(2\Delta\theta) - \gamma\frac{L^3}{12}u_s\sin^2(\Delta\theta) = 0 \tag{4.4}$$

or,

$$\omega_r = u_s\sin^2(\Delta\theta) + u_e\sin(2\Delta\theta) \tag{4.5}$$

To test this prediction, we find ω_r by fitting a polynomial to $\Delta\theta(t)$ and taking the derivative of the polynomial. An example is shown in Fig. 4.6(a). We then plot the results of such measurements in Fig. 4.7 against the RHS of of Eq.(4.5), which we denote as ω_p. The different colors of the data points correspond to ten different trials in which the torques were evaluated as the orientation of misaligned rods rotated back toward the director. The solid line is a guide to the eye that passes through the origin and has a slope of 2.5. As can be the case when taking numerical derivatives of data, the results are quite noisy. However, the linear relation predicted by Eq. (4.5)

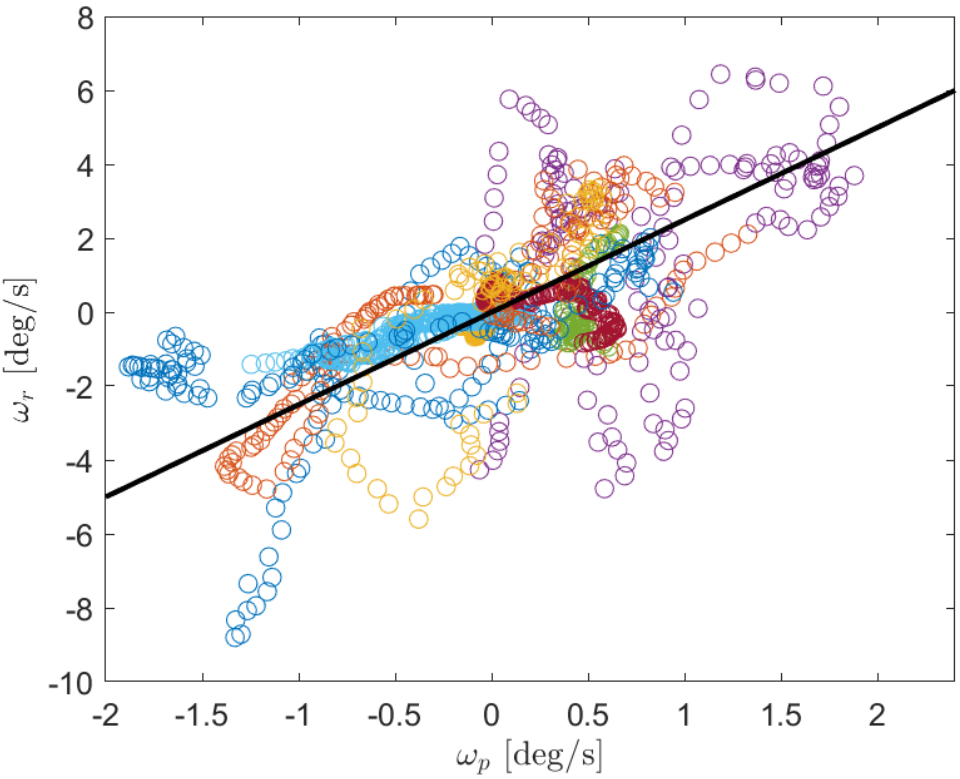

Figure 4.7: The measured rotation rate of the rods relative to the director plotted against the predicted rate based upon the measured shear and extensional flows near the rod. The colors of the data points represent different trials, and the solid line is a guide to the eye that passes through the origin with a slope of 2.5.

seems to be confirmed but with a slope that is larger than predicted. A source of this discrepancy could be the nature of the fluid in contact with the rod and its coupling to the film. As mentioned above, the rods appear to reside in a solution of unadsorbed microtubules adjacent to the film. These microtubules could give the region a viscoelastic character that resists flow gradients, effectively making the drag coefficient γ larger for the extensile and shear terms than for the solid rotation term.

4.4 Discussion and Conclusion

In conclusion, measurements of the nematic director correlation at a stationary location in the lab frame and along the flow of the active nematic film revealed two distinct and intriguing aspects of the film dynamics. The monotonic decay of the former is unsurprising given the turbulent-like flows within the film which act to decorrelate the director. However, the periodicity observed in the correlation of the director along the flow indicates that the director undergoes a more regular, predictable, rotation in this frame of reference. The time scale of this periodicity can be associated with the approximate time required for the $+1/2$ defects within the film to move a typical defect-defect spacing. In addition, we observe that the alignment of the rods with the director is driven by shear and extensional flows of the films. One can imagine that such alignment of the rods is not unlike the alignment of the constituent microtubule bundles themselves. We note that in the absence of any activity driven flows, these films form an isotropic gel. Thus, our results lend insight into the fundamental, dynamic mechanism of formation of nematic order in these systems.

4.5 Appendix

4.5.1 Measuring the rod and director orientations

The orientation of the rod was determined as described in Chapter 2. The values for $\Delta\theta$ shown in Fig. 4.4(a) were found by first measuring the orientation of the rod and the local director in the near vicinity of the rod. The data for each are smoothed by taking a moving mean of 10-20 frames. Finally, the difference between the two angles was found and then this was smoothed again by taking another moving mean of 10 frames.

Chapter 5

Dynamic and mechanical evolution of an oil-water interface during bacteria film formation

5.1 Introduction

Biofilms, assemblies of microbes in a self-produced conglomeration of extracellular polymeric substances (EPS), play a crucial role in the growth, protection, and dispersal of many bacteria species. Biofilms are abundant in nature and adept at existing in even extremely harsh environments. It has been estimated that 99% of all bacteria cells reside within biofilms, making them of fundamental importance to the life cycle of nearly all bacterial species. Some of the survival advantages associated

with biofilm formation include protection from shear stress, desiccation, radiation, antibiotic and chemical threats, osmotic stress, and from attacks from host immune cells, as well as more efficacious gene transfer [30]. The robustness of biofilm communities and their ability to survive in a wide range of environments also make them difficult to eliminate in undesirable settings. Biofilms are responsible for recurrent infections, contamination of medical and food processing equipment [126], and fouling of underwater equipment and ship surfaces [93]. Conversely, biofilms have also been utilized in constructive ways in environmental and industrial applications. For example, biofilms formed by hydrocarbon consuming bacteria have been used in bioremediation of marine oil-spills where they form at oil-water interfaces [93]. They have also been used for electrical energy extraction in microbial fuel cells [34, 75]. Therefore, understanding the material properties of these films is valuable in development strategies pertaining to their removal, prevention, or optimization in these contexts.

In general, biofilms can form at liquid-solid, liquid-air (where they are known as pellicles), or liquid-liquid interfaces. Biofilm formation involves the attachment or adsorption of the bacteria onto a solid or fluid interface followed by the secretion of EPS components by the cells [103]. The EPS can encase the cells in an extracellular matrix that consists primarily of polysaccharides, proteins, and nucleic acids. The mechanical integrity of the matrix is mostly due to the polysaccharides and proteins that often form a cross-linked viscoelastic polymer gel [159]. The viscoelastic properties of the film allow it to resist deformation when subject to small stresses while also

avoiding brittle fracture under large external stresses. However, biofilm structure and mechanical properties can vary greatly depending on the particular organism creating it and its local environment [14]. In fact, bacterial cells have been shown to change the amount of polymers they secrete and their cohesive strength according to changes in their environment [6, 134]. Experiments have shown that biofilm properties and growth rate at liquid-liquid and liquid-air interfaces are influenced by many factors, including the hydrophobicity of the bacteria cells, the surface tension of the interface, the subphase pH, and the bacteria growth medium [90,113,114]. Biofilms are also naturally heterogeneous structures. Consequently, conventional macrorheological studies effectively provide an average of the film's mechanical properties. Microrheology is able to probe the heterogeneity of a film, but relating the results of such interfacial microrheology to a film's material properties can be difficult.

Although much work has focused on the mechanical properties of biofilms that form on solid surfaces, relatively few studies have addressed films at liquid-air or liquid-liquid interfaces [52, 59, 74, 90, 103, 113, 114, 149, 150, 162, 163]. Fewer still have studied the time-evolution of biofilm rheology during the formation process, which is of interest from both a biological and physical perspective. In addition to the practical importance of biofilms at water-oil interfaces, which are particularly relevant in applications such as bioremediation and oil recovery, liquid-liquid interfaces provide unique environments in which hydrodynamics, physiochemical effects, and interfacial tension can conspire for intriguing outcomes [90, 151].

In this paper, we report a study combining passive particle tracking, active microrheology, and differential dynamic microscopy (DDM) to gain a comprehensive perspective on the evolution in mechanics and dynamics of an oil interface with a bacteria suspension during biofilm formation. We use the bacteria strain *Pseudomonas Aeruginosa* PA14 (wild type), a widely investigated model organism. Previous experiments using *Pseudomonas* have shown that a number of strains of the bacteria, including PA14, form viscoelastic biofilms over the course of several hours at an oil-water interface [90]. Vaccari and coworkers employed particle tracking with 1-μm-diameter colloidal spheres in concert with pendant drop elastometry to characterize the interfacial dynamics and mechanics of suspensions of *Pseudomonas* sp. in contact with hexadecane. They found that the evolution in the interface could be divided into three stages: an initial active stage in which the dynamics are dominated by the motile bacteria collecting at the interface, a transitional viscoelastic phase in which mean-square displacements of colloidal probes at the interface follow weak power-laws, and a final elastic stage in which the interface acquires a bending rigidity. The work by Niepa *et al.* studied two strains of *Pseudomonas Aeruginosa*, PA14 and PA01, as well as mutants of these strains in which certain genes associated with secretion of EPS components or with the growth of pili were deleted. They found that 1-μm-diameter passive tracers transitioned from superdiffusive to subdiffusive motion on the order of hours consistent with the stages of biofilm development identified by Vaccari *et al.*, although the films showed different properties depending on the strain

used, particularly at late ages. For example, PA01 strains became elastic after several hours, as determined by cessation of colloidal motion and the observation of wrinkles during compression of pendent drops, while PA14 strains did not. The mutant strains had a lower degree of film elasticity or formed a biofilm at later ages compared to the wild-type strains, demonstrating ways in which the bacteria's genetic makeup correlates with the resulting biofilm properties.

Although such previous studies have shown how the passive tracking of colloidal probes can sensitively detect changes in an interface during biofilm formation, significant open questions remain. One important question in particular is how to interpret probe mobility in terms of material properties in these heterogeneous and active films, where the application of generalized Stokes-Einstein relations used in microrheology of equilibrium systems [72, 133] are not necessarily valid. Indeed, the effects of interactions with motile bacteria on passive colloidal probes have been the subject of extensive work, where the probe motion has provided a window into the nature of the bacteria suspensions as an example of "active matter". In this regard, interfacial biofilms provide an intriguing experimental system for studying active matter within viscoelastic environments. To help gain insight into this issue, we conducted experiments in which we tracked passively moving spherical colloids at an interface during film formation in parallel with active microrheology measurements involving the rotation of microscale magnetic rods at the interface in response to time-varying magnetic fields. We studied the colloidal dynamics during a transition from a purely

active environment, prior to biofilm formation, into an active viscoelastic state during and after biofilm formation. The mechanical properties of the interface that one would infer from the passive and active measurements are strongly different. We attribute the discrepancy to the differing length scales over which the film properties are interrogated by the spheres versus the rods and to the differing effects of the activity of the motile bacteria in each case. To gain an understanding of the influence of each of these factors, we employed colloidal probes of varying sizes in the passive measurements and conducted differential dynamic microscopy (DDM) measurements in parallel to elucidate the evolving bacteria motion during film formation.

5.2 Materials and Methods

5.2.1 Magnetic Microrods and Fluorescent Spherical Colloids

The magnetic microscale rods used to probe the micromechanics of the interface were composed of ferromagnetic nickel and were fabricated by electrodeposition following procedures described elsewhere [139]. The rods, 370 nm in diameter and 30-75 μm in length, possess a magnetic moment coincident with their axis that is proportional to their length and is approximately $3 \cdot 10^{-13}$ A/m^2 for a 10-μm-long rod. The passive particle-tracking experiments employed fluorescent, charge-stabilized,

polystyrene spheres (Bangs Laboratories) of three diameters, 1 μm, 4 μm, and 15 μm. These three sphere diameters span scales from less than the bacteria cell size (1-5 μm length) to up to several times larger than this, providing a useful range for probing the relevant length scales affecting the local rheology. The 1-μm and 15-μm diameter spheres were internally dyed with "Dragon Green" fluorescent fluorophores (480 nm excitation, 520 nm emission), while the 4-μm-diameter particles contained "Flash Red" fluorophore (660 nm excitation, 690 nm emission).

5.2.2 Bacteria Suspension Preparation

We used *Pseudomonas Aeruginosa* PA14 (wild-type) strain for all experiments involving interfacial film formation. Additional active and passive microrheology with the rods at the interface in the absence of a film was performed using *Pseudomonas Aeruginosa* PA14 ΔPelA, a mutant which has the pelA gene deleted, thereby rendering the bacteria unable to form the extracellular matrix [90]. The bacteria were grown in LB broth medium while shaken at 200 RPM for approximately 36-48 hours at room temperature. Once the broth became turbid, a portion was extracted and centrifuged at 6000 g for 10 minutes. The supernatant was discarded and the bacteria were resuspended in 0.85% NaCl solution. This was repeated four times. The final number concentration of bacteria was approximately $1.6 \times 10^{10} mL^{-1}$, as determined from cell counting with a hemocytometer.

5.2.3 Sample Preparation

The sample cells were composed of aluminum rings of 1 cm inner-diameter and 0.8 cm in height. Glass slides attached to the rings using an optical adhesive (Norland Products) served as the sample cell bottoms for viewing from below. The rings were cleaned by scrubbing with a detergent, then sonicating in acetone followed by isopropyl alcohol and then deionized water. The substrate and ring were then hydrophobically treated with aquapel (Pittsburgh Glass Works) or rain-x glass water-repellant (Rain-X). Approximately 200 μL of HFE 7500 fluorinated oil (Ran Biotechnologies) was pipetted into the ring. The viscosity of the oil is approximately equal to that of water, 1 mPa·s. The oil is denser than water, thereby allowing for viewing of the interface through the oil phase using an inverted microscope (see Fig. 5.1). Bacteria suspension containing fluorescent spheres and ferromagnetic rods was then pipetted onto the surface of the oil to form an interface, and the top of the sample cell was covered with a coverslip to prevent evaporation. Since the spheres and rods are denser than water, they sedimented and became attached to the interface over the course of several minutes. The age of the interfaces t_a was taken as the time since the bacteria suspension was added atop the oil.

5.2.4 Video Microscopy

Measurements were performed using a Nikon Eclipse TE2000 inverted microscope. Magnetic fields were applied by an array of four pairs of magnetic solenoids mounted to the microscope and controlled with custom Labview code, as described elsewhere [67]. Fluorescent microscopy was conducted using an X-Cite 120PC mercury arc lamp light source. CY5 (Nikon) and FITC (Omega Optical) filter cubes were used for fluorescent imaging of spheres labeled with "Flash Red" and "Dragon Green" fluorophores, respectively.

Videos were acquired using a 20X (Nikon, CFI 40 LWD DL) objective and a Flare CameraLink (IO Industries) camera connected to the microscope. Typically, 1000 frames were captured at 3 fps for passive particle-tracking experiments of the spherical colloids. Additional measurements at frame rates of 0.4 and 30 fps were also conducted to extend the dynamic range. A frame rate of 30 fps was employed for all measurements of the rod response to external magnetic fields, and frame rates between 20 and 30 fps were used for passive particle-tracking measurements on the rods.

5.2.5 Passive Particle Tracking

Passive particle-tracking measurements were performed using both the spherical colloids and the magnetic rods. The positions of the fluorescent spherical particles

were tracked and their trajectories determined using custom Python code based on the Crocker-Grier algorithm [3]. Overall drift of the particles was determined by finding the average motion of the colloids between adjacent frames and was subtracted from the individual trajectories. Despite this correction, we found that a small amount of residual drift affected the results in measurements with very small colloid mobility. We believe this residual drift was due to spatial variation in the drift velocity of the biofilm across the field of view. Segmentation of the frames into sections for more local drift determination was performed in instances where the residual drift was significant, thus producing sufficient improvement on some cases.

To characterize the time-dependent position and orientation of the rods, we employed a custom python code as described previously [4]. Briefly, the code first applies a thresholding of the images that zeroed all pixels below a certain intensity value. The rods were then located by determining the largest connected region of non-zero pixels. The angle of the long axis of the rods was found by computing the eigenvectors of the moment of inertia tensor and finding the eigenvector with the largest eigenvalue.

5.2.6 Magnetic Rod Active Microrheology

Two types of measurements involving the response of the rods to external fields were performed. In the early stage of the interface before biofilm formation, when the interfacial dynamics were dominated by motile bacteria, we applied fields of constant

magnitude rotating in the plane of the interface that caused the rods to rotate at constant angular velocity and determined the effective interfacial viscosity from the rotational drag on the rod. Once the biofilm formed, the microrheology measurements were conducted by the application of step changes in the applied magnetic field. Starting initially from zero field, the applied field was switched on, creating a constant field oriented in the plane of the film at an angle to the rod. The rod's orientation as a function of time was then monitored as it rotated in response to the magnetic torque. As described below, the rod typically rotated until reaching an equilibrium orientation at which the magnetic torque was balanced with the elastic torque on the rod from the film. After some time, the field was then set back to zero, and the rod's orientation as a function of time was again monitored as it relaxed back toward its original orientation under the viscoelastic stresses of the film.

5.2.7 Differential Dynamic Microscopy

Differential dynamic microscopy (DDM) [44] measurements were performed to characterize the bacteria motion at the interface during film formation. Brightfield images were acquired and analyzed following the procedure described elsewhere [160]. Briefly, in a typical measurement 800 images were captured at 30 fps. The difference between all pairs of images in the sequence was determined, and the square of the Fourier transform of these differences as a function of wave vector $\vec{q}$ was calculated. An average over wave-vector direction and an average over all pairs of frames separated by

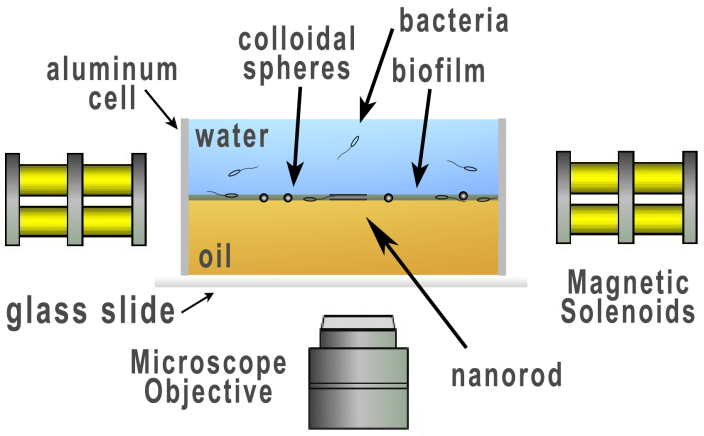

Figure 5.1: Schematic of the experimental system. Bacteria in the aqueous phase are pipetted over a layer of oil and adsorb to the interface where they form a biofilm. Passive fluorescently labeled spheres and magnetically controlled colloidal rods sediment to the interface where they are used in passive particle tracking and active microrheology experiments.

the same lag time t were then taken to obtain the image structure function $D(q,t)$ [44],

$$D(q,t) = \langle |I(\vec{q}, t+t') - I(\vec{q}, t'|^2 \rangle \tag{5.1}$$

where $I(\vec{q}, t')$ is the Fourier transform of the image $I(\vec{x}, t')$ acquired at t', and the average is over t' and over wave-vector direction. Prior to calculation of $D(q,t)$, the image functions $I(\vec{x}, t')$ were corrected for global drift by shifting the positions $\vec{x}$ in each frame relative to those of the preceding frame using Matlab's *imtranslate* function. Failure to account for drift in this way resulted in spurious oscillatory features in $D(q,t)$.

5.3 Results and Discussion

Immediately following addition of the bacteria suspension atop the oil to form the oil-water interface, bacteria were observed at the interface at high surface coverage. However, no collective swarming motion was observed. Hence, prior to film formation, the interface was densely populated by bacteria swimming randomly, creating a highly active system. At later interface ages, a viscoelastic film formed which resulted in a large reduction in mobility of the tracer particles [150]. As mentioned above, in order to characterize the evolution of the dynamics and mechanical properties of the interface throughout the process of biofilm formation, we conducted particle-tracking experiments with colloidal probes of different sizes – specifically, spheres with diameters of 1 μm, 4 μm, and 15 μm – in parallel with complementary passive particle-tracking and active-microrheology measurements using ferromagnetic rods of length 30-75 μm and with complementary DDM measurements to characterize the bacteria mobility at the interface. In the sections below, we describe the observations made with each experimental approach in turn and compare the results to interpret their implications for the mechanical and dynamical evolution of the interface.

5.3.1 Passive Particle Tracking

5.3.1.1 Tracking of Spherical Colloids

Figure 5.2(a) displays the ensemble mean-squared displacement (MSD) of 4-μm spheres at various ages of an interface, while Fig. 5.2(b) shows ensemble MSDs for all three sphere sizes at interface ages $t_a = 1$ hr and 6 hr. For comparison, the MSD of the 4-μm spheres measured at the bare oil-water interface in the absence of bacteria is included in the figures. The evolution in the particle mobility follows qualitatively the trends reported previously by Vaccari *et al.* At early ages the MSDs exceed those at the bare interface, indicating that the particle motion is strongly enhanced by interactions with the motile bacteria. However, at later ages the particle mobility becomes increasingly suppressed, as shown by significant decreases in the MSDs, reflecting the formation and development of a viscoelastic interfacial film. Specifically, in Fig. 5.2(a) one sees a only a minor change in the MSDs between $t_a = 1$ hr and 3 hrs, but then a significant reduction in probe mobility between $t_a = 3$ hrs and 5 hrs. Results for the MSDs of 4-μm spheres obtained during two additional experiments are shown in the Appendix. In those cases, the MSDs undergo a qualitatively similar reduction over the same time scale, but the changes are more continuous, indicating the variation in the evolution of probe dynamics that can occur under nominally identical experimental conditions.

A key feature of the particle mobility at the interface is the dependence on probe

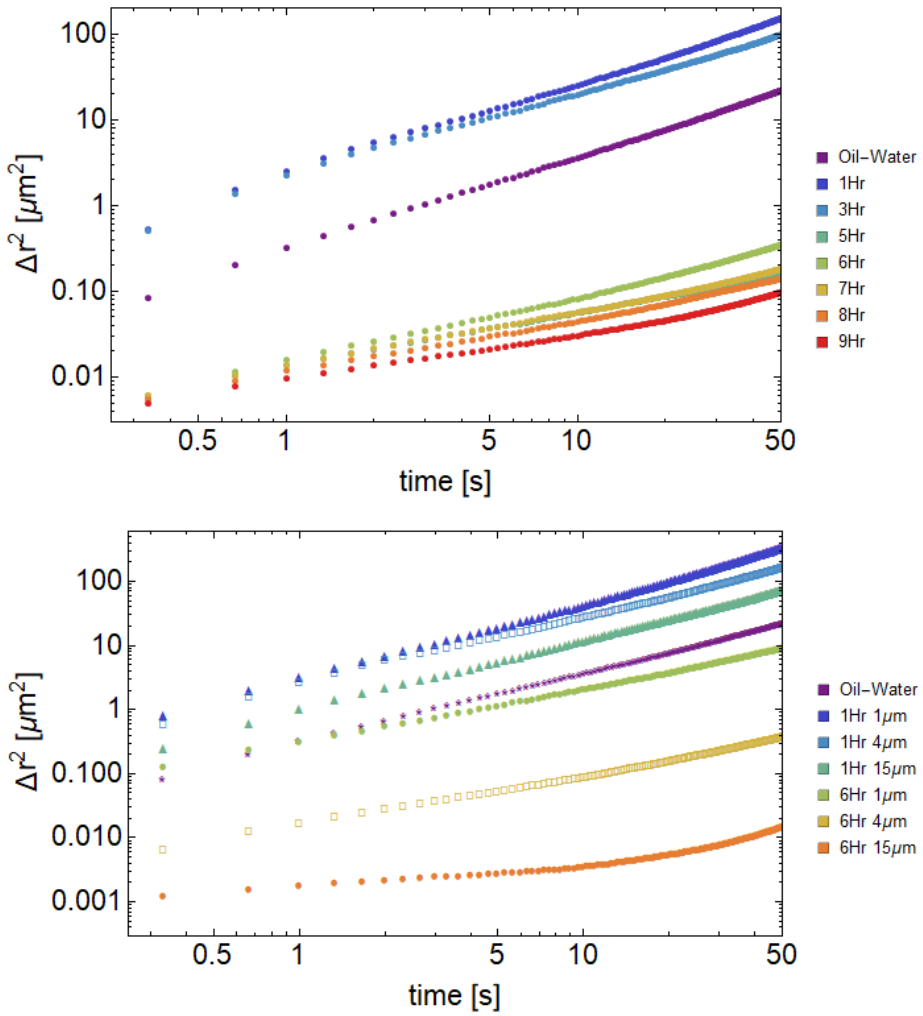

Figure 5.2: (a) Ensemble mean-squared displacements of 4 μm-diameter spherical particles in the pre-biofilm ($t_a < 5$ hours) and biofilm ($t_a \geq 5$ hours) stages of the interface. (b) The mean-squared displacements of spheres of three different sizes at ages of 1 hr and 6 hr. The frame rate in all measurements was 3 fps.

size and particularly the evolution in size dependence with interface age. As seen Fig. 5.2(b), the mobilities of the different-sized probes diverge strongly from one another as the biofilm forms. At $t_a = 1$ hr, the MSDs of the 1-μm and 15-μm spheres have similar shape and differ by a modest factor of 3 to 4. This factor is even smaller than that predicted by the Stokes-Einstein relation, wherein the MSDs of colloids undergoing Brownian motion are predicted to vary inversely with colloid diameter. This anomalously small size dependence at the early interface age potentially reflects effects similar to those reported by Patteson *et al.*, who observed diffusivities of probes in bacteria suspensions that varied non-monotonically with probe size [98]. The situation changes dramatically, however, at later ages when the influence of the biofilm is strong. For instance, after $t_a = 6$ hrs, the 15-μm spheres have become essentially static with an MSD, $\langle \Delta r^2(t) \rangle \approx 10^{-3}$ μm^2, that is near the measurement resolution, while the MSD of the 1-μm spheres exceeds this value by a factor or 100 to 1000 over the range of lag times probed. The diverging probe mobilities are further illustrated in Fig. 5.3(a), which shows $\langle \Delta r^2(t) \rangle$ at $t = 10$ s as a function of age for the probes of different size. The very large difference in mobility with size at late age is particularly striking when considering that, with formation of the biofilm, the interfacial stresses on the probes should become dominant, and hence the hydrodynamics should become essentially two-dimensional in which case the particle mobility should become independent of probe diameter [115].

To characterize the evolution of the MSDs more quantitatively, we fit them to a

power-law form, $\langle \Delta r^2(t) \rangle = bt^\alpha$, which in most cases provides a good approximation to the data at least over a limited range of lag times. The fits are restricted to the range, 1.7 s $< t <$ 33 s, during which the power-law form is most accurate. The power-law exponent α extracted from the fits is shown in Fig. 5.3(b). At the earliest age, $t_a = 1$ hr, the probes exhibit slightly superdiffusive motion ($\alpha > 1$), and then the motion becomes essentially diffusive ($\alpha \approx 1$) at somewhat later age, $t_a = 3$ hr. The reduction in mobility at $t_a = 5$ hr and above is accompanied by a transition to subdiffusive motion ($\alpha < 1$), qualitatively consistent with previous results on 1-μm spheres at the interface of suspensions of PA14 and hexadecane. The divergence in the mobilities of the probes of different sizes is again apparent in this subdiffusive behavior of the MSDs, where, as seen in Fig. 5.3(b), α decreases more quickly for the larger-diameter colloids. As discussed below, we attribute this large size dependence to the varying effects of activity due to the motile bacteria in the biofilm.

Subdiffusive motion is often described by models such as caged-diffusion, continuous-time random walks, obstructed diffusion, or fractional Brownian motion [129]. We find that the particle's velocity-correlations within the biofilm are in fairly good agreement with those predicted by a fractional Brownian motion model (see Appendix), which is often used to model particle motion in viscoelastic materials [54, 158]. We provide plots the velocity-correlations of the particles along with the theoretical curves in the Appendix.

For another perspective on the sphere motion in the biofilms, Fig. 5.4(a) displays

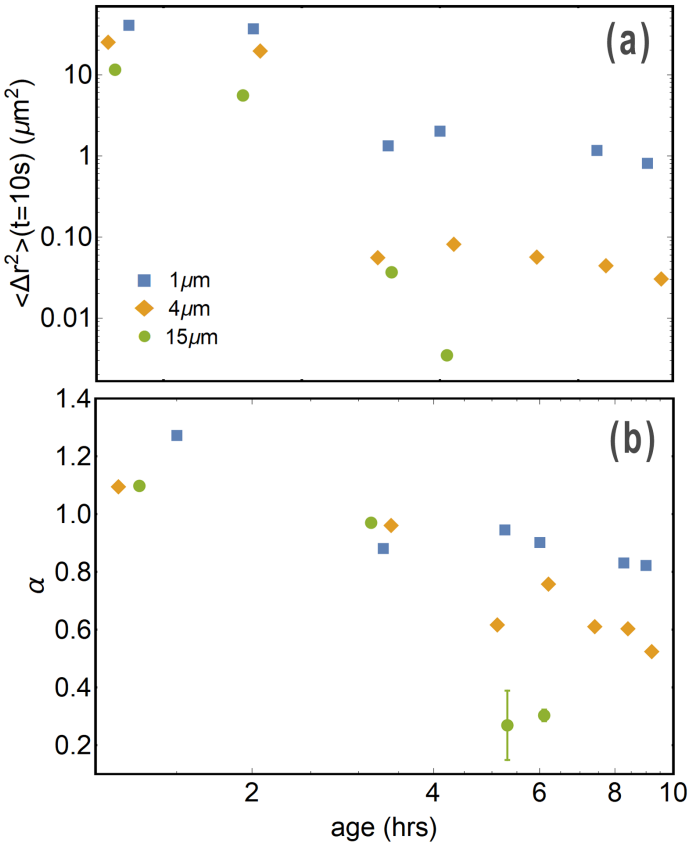

Figure 5.3: (a) The mean-squared displacement of the spheres at a lag time of 10 seconds as a function of age. The mobility of the colloids, particularly the ones of largest size, decreases significantly upon formation of the biofilm at approximately 3 hours. (b) Exponents from power-law fits to the MSDs of the colloids a function of age. The colloids are slightly superdiffusive prior to biofilm formation and become subdiffusive once the biofilm forms.

the Van-Hove correlation function, which is the probability distribution of particle displacements, of the ensemble of 4-μm particles at a lag time of 1/3 s at $t_a = 9$ hrs. For particles in thermodynamic equilibrium, the Van-Hove correlation is Gaussian. In contrast, the spheres' van Hove function has large non-Gaussian tails reflecting excess probability of large displacements, as illustrated by the comparison with the Gaussian lineshape in Fig 5.4(a). While such non-Gaussian behavior can reflect a variety of out-of-equilibrium dynamical properties, in this case we can identify it with spatial heterogeniety of the dynamics. This heterogeneity is illustrated in Fig. 5.4(b), which displays examples of the Van-Hove correlations of two individual 4-μm spheres from the ensemble. Both individual correlation functions are Gaussian, which is what we find for the vast majority of the particles at all ages. We show the MSDs of the two particles in Fig. 5.4(c). Both particles display motion that is similarly sub-diffusive, but the curves are well separated throughout the experimental time frame, indicating a persistence to the heterogeneity in mobility over at least tens of seconds. In other words, particles that have relatively less or greater mobility at the start of the measurement continue to have less or greater mobility throughout the video. Thus, the non-Gaussian character of the ensemble van Hove correlation function is a consequence of averaging over particles whose dynamics individually obey Gaussian statistics but with significant variation in mobility. This variation is illustrated by the wide distribution of Gaussian widths over the population of particles shown in Fig. 5.4(d).

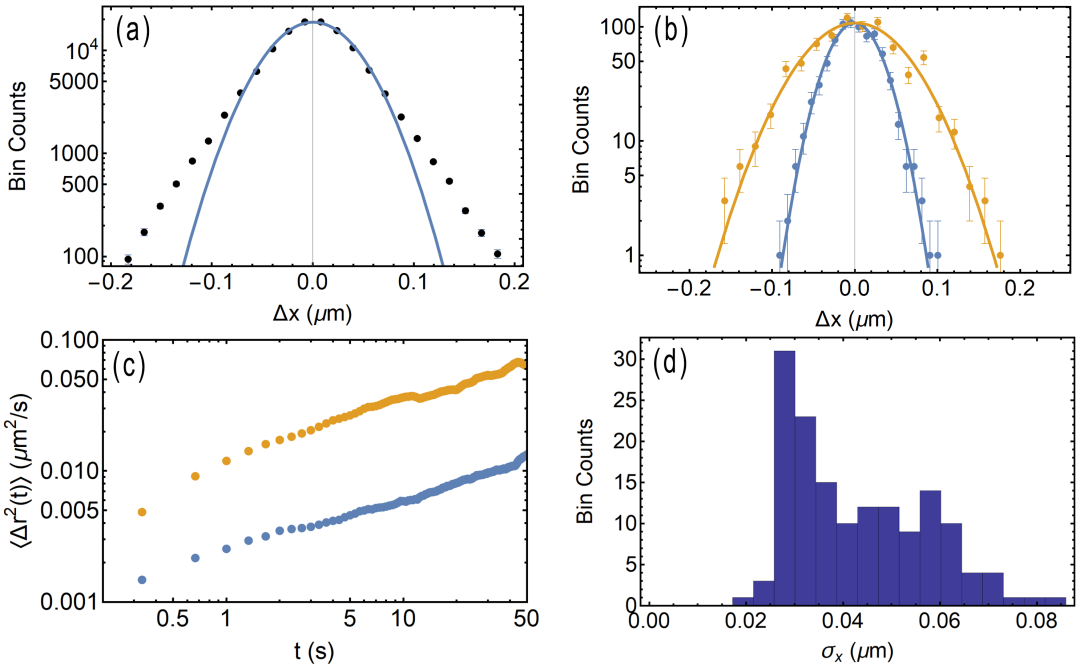

Figure 5.4: (a) Ensemble average Van-Hove correlation function of the displacement of 4-μm spheres over 0.33 s within a biofilm at an age of 9 hours. The solid blue curve is a Gaussian fit to the data. (b) Van-Hove correlation functions for two individual spheres at the interface in comparison with Gaussian fits giving widths of $\sigma_x = 0.055$ μm and 0.028 μm. (c) The MSDs for the same two spheres. The consistency of their separation with time indicates a disparity in the mobility of the particles that persists upwards of at least tens of seconds. (d) The distribution of widths of the Van-Hove correlations of the ensemble, as determined by conducting Gaussian fits to the data for each sphere.

Qualitatively similar results as that shown in Fig. 5.4 were found at all ages. Prior to biofilm formation, the large variances could be due to heterogeneities caused by secretions of the bacteria in the incipient film, or possibly from differences in bacteria-particle interactions, such as attachment. The colloids seemed to act as nucleation sites of the viscoelastic biofilm, therefore this effect could lead to a variation of effective particle sizes during the biofilm formation stage.

5.3.1.2 Tracking of Rods

5.3.1.2.1 Orientational Fluctuations

To gain another perspective on the mobility of colloidal tracers at the interface, we performed particle-tracking measurements of the passive motion of magnetic rods. Because of the rods' large magnetic moment μ, the torques imposed by magnetic fields as small as earth's field constrain their orientation such that thermal orientational fluctuations are immeasurably small. For instance, in a 1 G field at room temperature, $\mu B/k_BT \sim 10^4$. However, consistent with the enhanced mobility of the spheres at early interface age, rods at the oil interface of the bacteria suspension underwent measurable orientational fluctuations. Figure 5.5 displays the angular MSD, $\langle \Delta\theta^2(t) \rangle = \langle (\theta(t') - \theta(t'+t))^2 \rangle_{t'}$, of a rod of length 29 μm at the active bacterial interface in the presence of a 1 G field, where $\theta = 0$ is taken as the direction of the field. To interpret this correlation function, we assume an overdamped Langevin equation describing the rotational motion [79],

$$\gamma_R \eta \dot{\theta} = \Gamma_B + \zeta_A(t) \tag{5.2}$$

where $\Gamma_B = \mu B \sin(\theta) \approx \mu B \theta$ is the magnetic torque, $\zeta_A(t)$ is a random active torque, $\gamma_R = \frac{\pi L^3}{3(ln(L/d) - 0.662 + 0.917 L/d)}$ is the geometric drag coefficient of a rotating rod [146], and we ignore random thermal forces since they are deemed insignificant in comparison to the active forces. (Note γ_R is the coefficient for rod rotation in a bulk, three-dimensional fluid. As described below, γ_R must be replaced with a

two-dimensional version at later interface ages when the interfacial rheology of the biofilm dominates the rotational response.) Assuming correlations in the random active torques decay exponentially in time, $\langle \zeta_A(t)\zeta_A(t') \rangle = \frac{D_A}{\tau} \exp(-|t-t'|/\tau)$, we can use Eq. (5.2) to obtain an expression for $\langle \Delta\theta^2(t) \rangle$ [79],

$$\langle \Delta\theta^2(t) \rangle = 2D_A \Big(\frac{\tau_B(1-e^{-t/\tau_B}) - \tau(1-e^{-t/\tau})}{1-(\tau/\tau_B)^2} \Big) + \Delta\theta_0^2 \tag{5.3}$$

where $\tau_B \equiv \gamma\eta/\mu B$ sets the timescale at which the MSD becomes constrained by the magnetic torque, and $\Delta\theta_0^2$ is an offset introduced to account for noise in the images.

A fit to $\langle \Delta\theta^2(t) \rangle$ using Eq. (5.3), shown by the line in Fig. 5.5, agrees well with the data and gives $\tau_B = 0.554 \pm 0.013s$, $\tau = 0.082 \pm 0.007s$, $D_A = (4.19 \pm 0.12) \times 10^{-3}$ s^{-1}, and $\Delta\theta_0^2 = (2.4 \pm 2.2) \times 10^{-5}$. The de-correlation time of the active forces, τ, is comparable to that obtained in particle tracking of colloidal spheres in other active bacteria suspensions [78, 79, 150]. Additionally, the value of τ_B provides a result for the rotational drag viscosity,

$$\eta = \frac{\tau_B \mu B}{\gamma} \tag{5.4}$$

which is found to be $\eta = (4.3 \pm 1.4) \times 10^{-3}$ Pa·s. This value of the viscosity is a 3-4 times that of the bulk oil and water subphases and is approximately twice that obtained in active microrheology measurements described below.

5.3.1.2.2 Effective Temperature

The behavior of $\langle \Delta\theta^2(t) \rangle$ can be divided into three regimes. In the first, when $t \ll \tau$, the MSD increases ballistically, $\langle \Delta\theta^2 \rangle \approx \frac{2D_A t^2}{\tau(1-(\tau/\tau_B)^2}$. In the second, when

$\tau_B \gg t \gg \tau$, the behavior is diffusive, $\langle \Delta\theta^2(t) \rangle \approx 2D_A t$. Finally, at very long times, $t \gg \tau_B$, the MSD plateaus, $\langle \Delta\theta^2(t \to \infty) \rangle = \frac{2D_A\tau_B}{1+\tau/\tau_B} \approx 2D_A\tau_B$. From this large-lag-time plateau in the rotational displacements, one can identify an "effective temperature" of the active bath,

$$T^R_{eff} = \frac{\mu B \langle \Delta\theta^2(t \to \infty) \rangle}{2k_B} \approx (32 \pm 10) T_{RT} \tag{5.5}$$

where $T_{RT} = 293$ K is room temperature. We note that in a typical passive microrheology measurement, one is only able to find an effective diffusivity and then must assume a value for η in order to extract an effective temperature. In contrast, measuring the motion of a probe within a potential energy well allows for the determination of both η_{eff} and T^R_{eff} from equations 5.4 and 5.5, respectively. Therefore, this technique provides a more complete picture of the active environment influencing the probe's motion.

The notion of an effective temperature is supported by the angular probability distribution function of the rod, which follows a Boltzmann-like form, as shown in Fig. 5.6. Previous experiments of an active colloidal suspension under gravitational force found the position probability distribution to exhibit a Boltzmann form with an effective temperature equal to that determined by their diffusive motion [97]. Additionally, experiments of an active system of particles in a harmonic potential found a Boltzmann probability distribution when the confinement size was much larger than the correlation length of the active swimmer's trajectories [137]. A similar result was found for a colloid trapped in a harmonic potential within a bacterial

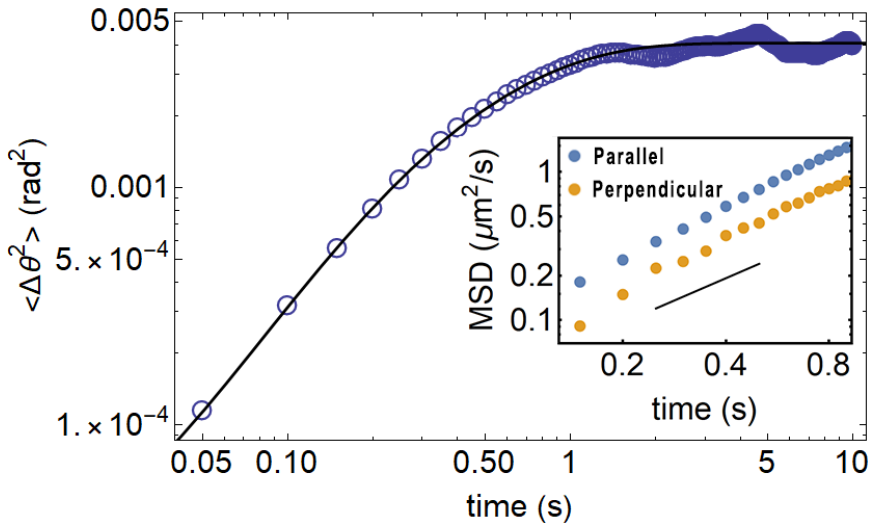

Figure 5.5: Rotational mean-squared displacement of a rod in a bacterial suspension while confined by the potential from a 1 G magnetic field. The solid curve is a fit using equation 5.3. Inset: MSD of the translational motion of the same rod parallel (blue) and perpendicular (orange) to the rod's axis. The solid line has a slope of 1.

bath [7].

5.3.1.2.3 Positional Fluctuations

In addition to measuring the rod's angular MSD, we tracked the center of mass of the rod to compare its translational and rotational mobilities. We separated the center-of-mass motion into components parallel and perpendicular to the rod axis. The resulting translational MSDs, shown in the inset in Fig. 5.5, vary approximately proportionally with lag time, implying effective diffusive motion, $\langle \Delta r^2_{\parallel,\perp}(t) \rangle = 2D_{\parallel,\perp}t$ over the range of lag times shown. From this diffusive motion, we can identify additional effective temperatures for each direction of motion,

$$T^{\parallel,\perp}_{eff} = \frac{\eta \gamma_{\parallel,\perp} D_{\parallel,\perp}}{k_B} \tag{5.6}$$

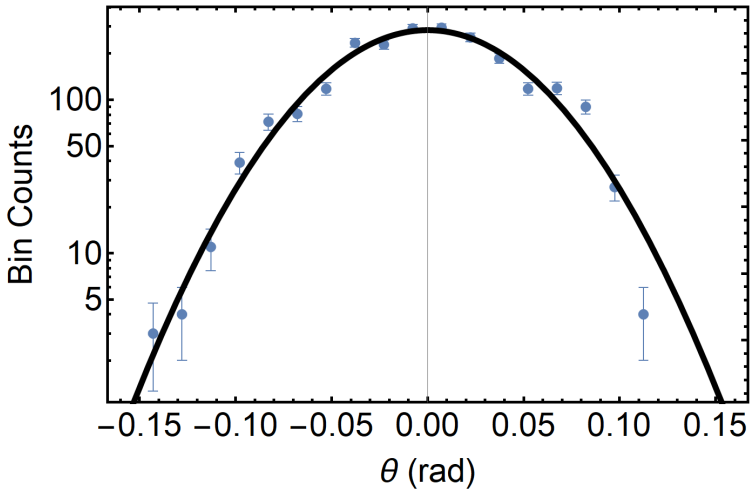

Figure 5.6: The Van-Hove correlation function of the angle of the rod relative to its mean orientation, which corresponds to the direction of the magnetic field. The solid line shows the results of a Gaussian fit to the data. The distribution is in good agreement with a Boltzmann form, with an effective temperature $(29 \pm 9)T_{RT}$. Uncertainties are determined by the square root of the number of counts per bin.

where $\gamma_{\parallel} \approx \frac{2\pi L}{ln(L/d)-0.2}$ and $\gamma_{\perp} \approx \frac{4\pi L}{ln(L/d)+0.84}$ are the drag coefficients in the parallel and perpendicular directions, respectively [147]. Based on the viscosity obtained from the rod's orientational fluctuations (Eq. (5.4)), we find $T^{\parallel}_{eff} \approx T^{\perp}_{eff} \approx (101 \pm 34)T_{RT}$. The approximate equality of $T^{\parallel}_{eff}$ and $T^{\parallel}_{eff}$ implies the ratio $D_{\parallel}/D_{\perp}$ is similar to that of thermal diffusion. Previous experiments investigating the translational diffusion of ellipsoidal colloids in *E. Coli* suspensions within soap films [100, 165] found that $D_{\parallel}/D_{\perp}$ was significantly smaller than expected from equilibrium at high bacterial concentrations. The authors of the study postulated that the persistence time of the anisotropic particle's motion along the minor axis was enhanced due to the effects of the extensile dipole flow field created by the swimming bacteria. This effect is expected to be weak when the bacteria density is below the critical number

for swarming behavior. Since we do not observe swarming in our system, the lack of evidence of anomalous diffusion between the parallel and perpendicular directions is consistent with this picture. However, the effective temperature obtained from the translational diffusion is somewhat larger than that obtained from the rotational diffusion, indicating a possible difference in the hydrodynamic coupling between the bacteria and the rod's rotational and translational degrees of freedom.

5.3.2 Active Microrheology

5.3.2.1 Rod Mobility at Early Interface Age

As a complementary method for investigating the evolution of the mechanics and dynamics of the oil-water interface during biofilm formation and aging, we conducted active microrheology measurements with the ferromagnetic rods. At early age ($t_a <$ 2 hrs), when the interfacial dynamics are dominated by the activity of the motile bacteria, the measurements involved the application of a field of strength B rotating at constant angular velocity ω in the plane of the interface such that the rods rotated in response. Due to drag, the axis of the rod lagged the field by an angle ψ, providing a means of determining an effective drag viscosity. Specifically, in steady state the magnetic torque and drag torque on the rod are balanced,

$$\mu B \sin(\psi) = \omega \gamma_R \eta, \tag{5.7}$$

where η is the viscosity. Figure 5.7 displays results for $\sin(\psi)$ as a function of ω from measurements on a rod of length 31 μm in a rotating 10 G field. The line displays the result of a linear fit from which a viscosity of 1.8 ± 0.2 mPa·s is obtained through Eq. (5.7). Similar measurements on several other rods at active interfaces resulted in an average viscosity of 2.2 ± 0.4 mPa·s. This is comparable to that obtained from similar measurements at the bare oil-water interface (3 ± 1 mPa·s), indicating that presence of the motile bacteria at early interface ages has negligible effect on the drag on the rod. Thus, the rod's rotational response to the torque from the external field contrasted with its spontaneous orientational fluctuations at early age, which as described above, were strongly enhanced over thermal diffusion due to the activity of the bacteria. Such contrasting behavior in passive and active measurements is well documented in bacteria suspensions [17].

Our results indicate that the effective viscosity found from the passive rod is similar, or possibly slightly greater, than the viscosity found from the actively rotated rod. The possible difference in viscosities could perhaps be the result of reduced effective viscosity when performing active rheology on an active bacterial suspension, as has been seen elsewhere [76]. However, the linearity seen in Fig. 5.7 is an indication of a lack of shear rate dependence of the effective viscosity down to ~ 0.5 Hz. The difference therefore could instead be the result of changes to the drag at low Peclet number, where the diffusive motion becomes comparable to the rotational motion. If one defines the Peclet number as $Pe = \nu/D$, where ν is the rotational frequency of

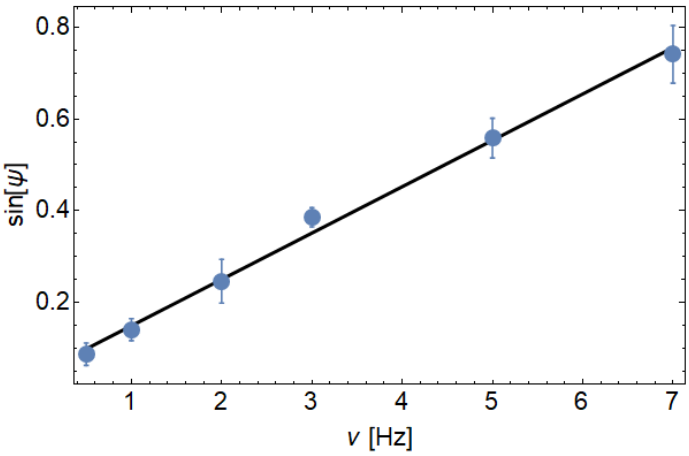

Figure 5.7: Sine of the angle by which the orientation of a ferromagnetic rod of length 31 μm at the interface before biofilm formation lags a 10-G magnetic field that is rotating at frequency ν. The slope is proportional to the drag torque on the rod.

the rod in Hz, then at 0.5 Hz, Pe is roughly 200, which is still quite large. A previous study conducting both passive and active microrheology in an active bacterial suspension found little difference in the measured drag between active and passive measurements [78]. However, aside from those experiments being conducted in a 3D system compared to our quasi-2D interface, another possible important experimental difference is that the effective temperature in [78] was only about 1.5 times room temperature, therefore the effects of activity were most likely greatly diminished.

5.3.3 Active Microrheology of an Aging Biofilm

Once the biofilm had formed, the viscoelastic nature of the film made measurements of the rods under constant rotation unfeasible. Instead, at later age the active measurements tracked the rotational response of a rod to the application of step-like

changes in magnetic field between zero and a constant value B in the plane the interface at an angle ϕ_0 to a rod's magnetic moment. An example of the resulting time-dependent angle of rotation θ away from its initial orientation in such a measurement is shown in Fig. 5.8 for a rod length 34 μm in a film at age 22 hours. At $t = 0$, a 40 G magnetic field was applied at $\phi_0 = 110°$, causing the wire to rotate until the angle reached a plateau at $\theta \approx 46°$ (*i.e.*, an angle of $\phi_0 - \theta \approx 64°$ with respect to the field), at which point the magnetic torque on the rod was balanced by an elastic restoring torque from the film. The field was then set back to zero at $t = 22$ s, allowing the orientation of the rod to relax under the viscoelastic stresses of the film. Notably, the rod rotated essentially fully to its initial equilibrium orientation, $\theta = 0$, indicating no unrecoverable strain and hence a rheological response of the biofilm that is free of creep. (Because of slight global rotation of the biofilm during these measurements, ϕ_0, the angle between the field and the equilibrium orientation of the rod, typically changed by 2-3° over the course of the measurement, and the data are corrected for this variation.) We observed such viscoelastic-solid response in all measurements on fully formed biofilms, where we varied the strength of the applied field over the range 5-150 G and applied the magnetic torque for durations up to 2 minutes. Solid-like behavior on this timescale is consistent with previous studies of the mechanical properties of biofilms on solid substrates, in which an elastic relaxation time of approximately 20 minutes was observed for a range of systems [123].

As Fig. 5.8 illustrates, the rotational response of the rod to the changes in magnetic

field is characterized by an initial fast rotation followed by a slower terminal relaxation to the final angle. We find a viscoelastic model consisting of two Kelvin-Voigt spring-dashpot segments in series, depicted schematically in the inset of Fig. 5.8, describes the behavior accurately. The model is described by the constitutive equations of motion,

$$G_1\theta_1 + \eta_1\dot{\theta_1} = -\frac{\mu B}{\gamma_{2D}} sin(\phi_0 - \theta) \tag{5.8}$$

$$G_2\theta_2 + \eta_2\dot{\theta_2} = -\frac{\mu B}{\gamma_{2D}} sin(\phi_0 - \theta) \tag{5.9}$$

$$\theta = \theta_1 + \theta_2 \tag{5.10}$$

where G_1, G_2, η_1, η_2 are the (two-dimensional) elasticities and viscosities associated with the springs and dashpots, respectively, θ_1 and θ_2 are the rotational strains of each Kelvin-Voigt segment, and $\gamma_{2D} = 1.5L^2$ [71] is the geometrical coefficient for rotational drag on a rod in two dimensions. We conducted least-squares fits to $\theta(t)$ using the model in which the data during both the rotational response to the field ($t < 22$ s) and subsequent zero-field rotational relaxation ($t > 22$ s) were fit simultaneously with four parameters: η_1, η_2, G_1, and G_2. As mentioned above, global rotation of the biofilm caused ϕ_0 to change slightly ($< 5°$) during the experiment. Due to uncertainties associated with correcting for this bulk rotation, the best fit was given freedom to shift the relaxation segment of the fit along the y-axis by an amount up to the estimated maximum uncertainty of 0.5°. Figure 5.8 displays the result of the fit, which describes the data well and which results in the parameter values $\eta_1 = 33.7$

Pa·s·μm, $\eta_2 = 0.4$ Pa·s·μm, $G_1 = 11.6$ Pa·μm, and $G_2 = 5.3$ Pa·μm. Similarly good agreement was found for all measurements conducted on fully formed biofilms.

Such active microrheology experiments were performed on several biofilms, and measurements were conducted as the biofilms aged, providing temporal information of the films' viscoelastic properties. Measurements were initiated once the biofilm had formed sufficiently, as determined by the inability of the rod to fully align with the magnetic field ($t_a \approx 3$ hrs). Qualitatively consistent behavior was observed across all trials. Surprisingly, the films showed no significant change in the viscoelastic parameters as a function of age, except perhaps for a slight increase in the elastic constants with age until $t_a \approx 10$ hours. However, the viscoelastic parameters showed large variation between biofilms, which we believe reflected mesoscale heterogeneity in the film properties. Overall, across multiple trials, the viscoelastic constants were found to have average values and standard deviations of $\eta_1 = 49 \pm 38$ Pa·s·μm, $\eta_2 = 0.80 \pm 0.76$ Pa·s·μm, $G_1 = 9.8 \pm 6.8$ Pa·μm, and $G_2 = 4.8 \pm 4.0$ Pa·μm.

Notably, the viscoelastic behavior of the biofilms measured in these active microrheology experiments is strikingly unlike the film rheology that one would infer from the MSDs of the 1-μm and 4-μm colloids spherical colloids at late age shown in Fig. 5.2. One clear qualitative difference is the lack of a plateau in the MSDs that one would expect for a passive tracer in a viscoelastic solid. To make this comparison more concrete, we note that for a 2D medium in thermodynamic equilibrium, the MSDs are related to the creep compliance $J(t)$ through a generalized Stokes-Einstein

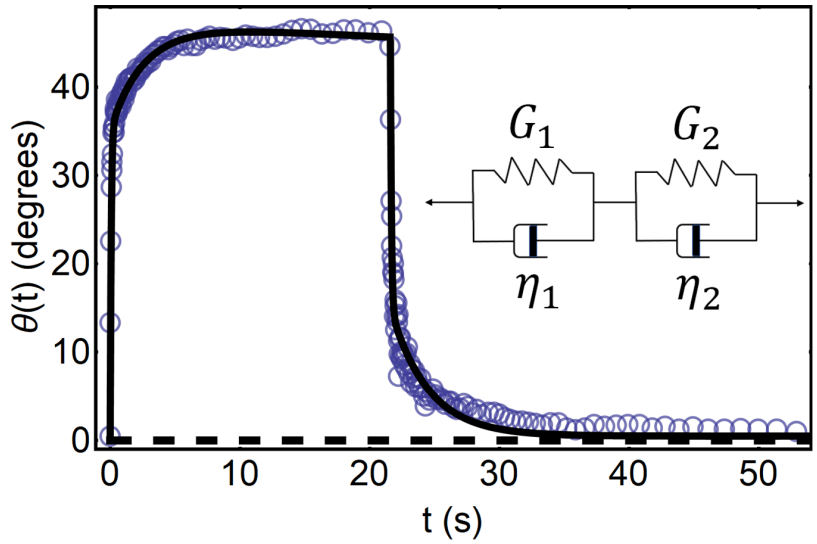

Figure 5.8: The angle of rotation of a ferromagnetic rod embedded within a biofilm at an age of 22 hours while subject to a magnetic torque (t $<$ 22 seconds) and relaxing under no external torque (t $>$ 22 seconds). At t = 0 the magnetic field of strength 57 G is directed at 110 degrees to the rod axis. The solid curve represents the best fit to the data using a double-Kelvin-Voigt viscoelastic model. The horizontal dashed line corresponds to the location of the rod's equilibrium orientation. The time constants associated with the viscoelastic model, which were extracted from the fit are 2.9 s and 0.08 s. Inset: Schematic of viscoelastic model consisting of two Kelvin-Viogt systems in series.

relation,

$$\langle \Delta r^2(t) \rangle = \frac{2k_B T}{3\pi} J(t) \tag{5.11}$$

For the double Kelvin-Voigt system the creep compliance is

$$J(t) = \frac{1}{G_{eff}} - \frac{e^{-tG_1/\eta_1}}{G_1} + \frac{e^{-tG2/\eta_2}}{G_2} \tag{5.12}$$

with $G_{eff} = G_1 G_2/(G_1 + G_2)$. According to the active microrheological results, therefore, the MSDs of the spheres should show two time constants, η_1/G_1 and η_2/G_2, and should reach a plateau of $2k_B T/3\pi G_{eff}$ at large lag times. The time constants obtained from the measured viscoelastic parameters were on the order of fraction of a second for the fast time constant and tens of seconds for the slow time constant. As one can see from Fig. 5.2, the MSDs do not display any obvious structure on these timescales. Additionally, based on a typical value of G_{eff} of 3 Pa·μm, the expected plateaus in the MSD should be at about 3×10^{-4} μm^2, well below the actual MSDs of the spheres shown in Fig. 5.2 and in fact below the resolution of the particle tracking measurements. The failure of Eqs. (5.11) and (5.12) to the describe the MSDs quantitatively is not surprising given the out-of-equilibrium nature of the system. However, such a strong and qualitative discrepancy implies a breakdown that goes beyond, for example, a simple "effective temperature" picture like that invoked above to describe the passive rod motion prior to biofilm formation.

A number of previous studies have noted large discrepancies between the rheology inferred from passive particle-tracking measurements of colloids at viscoelastic interfaces and the results of macroscopic interfacial rheology and have speculated

about the origins of these discrepancies. One clue to the origin of the discrepancies between the sphere mobility and the active microrheology of the biofilms comes from considering the sizes and geometries of the colloids. As discussed above, the mobilities of the spherical tracers of different size diverge from one another during the biofilm formation and aging, with the larger spheres becoming orders-of-magnitude less mobile, in contrast to the expected size-independent diffusion of spheres in 2D (see Fig. 5.2(b)). This divergence suggests that the mechanical properties of the biofilms could be lengthscale dependent. The rods employed in the active microrheology were 30-75 μm in length and rotated through large angles, thereby probing the rheology on lengthscales comparable to their length. Notably, in the particle-tracking measurements the 15-μm spheres, whose size most closely matched that of the rods, became essentially immobile as the biofilms formed, qualitatively consistent with the viscoelastic-solid behavior measured in the active rheology. The dramatically higher mobility of the 4-μm and especially 1-μm spheres thus suggests that the biofilms might have hierarchical mechanical properties such that they are significantly more compliant and fluid-like at the smaller scales of these particles. The mesh size of the polymer extracellular matrix (ECM) of biofilms is likely much smaller than the colloids [159]; therefore, we do not anticipate the lengthscale set by the mesh has any direct influence. Notably, however, the bacteria, which are 1-5 μm in length, have a size that is similar to that of the smaller, more mobile spheres. This similarity suggests an intriguing speculation that the biofilms potentially form with a hierarchi-

cal mechanical structure that has a compliant, fluid-like rheology on the scale of the bacteria to facilitate their motility in the films but more rigid, solid-like rheology on larger lengthscales to maintain mechanical integrity.

Another possible source of the discrepancies between the mobility of the smaller spheres and the active microrheology could be the activity of the bacteria within the biofilm. Just as the particle tracking measurements on the spheres and rods at the interface prior to biofilm formation revealed diffusive and even superdiffusive motion dominated by the interactions with the swimming bacteria, so potentially could residual bacteria motility in the biofilms induce probe motion. Generally, bacteria can be motile or nonmotile within biofilms. For example, an experiment performed with *Pseudomonas Aeruginosa* PA01 biofilm found a subpopulation of motile cells that moved on average 1.5 $\mu m/hr$ with 90% of these cells moving less than about 6 $\mu m/hr$ [108]. In other experiments, it has been shown that bacteria in the bulk fluid can penetrate and move within the biofilm [53]. In the microscopy measurements after biofilm formation, fluctuations in videos of the interface suggested that the bacteria retained some motility. However, the bacteria at the interface were too crowded, and the interface was otherwise to visually heterogeneous to resolve the motion directly. Therefore, to understand the extent to which the bacteria remained motile, we performed differential dynamic microscopy (DDM) measurements, as describe in the next section.

5.3.4 Differential Dynamic Microscopy of an Aging Biofilm

Measuring the mobility of the bacteria by directly tracking individual cells was unfeasible due to the high density of bacteria at the interface, their small size, and the mottled appearance of the interface once the biofilm formed. Therefore, we employed differential dynamic microscopy (DDM) to circumvent these limitations. As described in Sec. 5.2.7, DDM involves measuring an ensemble quantity, the image structure function $D(q,t)$, which is related to the intermediate scattering function $g(q,t)$ via,

$$D(q,t) = A(q)(1 - g(q,t)) + B(q) \tag{5.13}$$

where $A(q)$ depends on the spatial intensity correlations in the images, and $B(q)$ is due to digital noise. The intermediate scattering function, which has the limits $g(q,0) = 1$ and $g(q, t \to \infty) = 0$ for an ergodic system, is the spatial Fourier transform of the density autocorrelation function, or van Hove function. A strength of DDM is its access to dynamics a larger wave vectors than can be reached with other techniques that measure DDM $g(q,t)$, such as dynamic light scattering. As a microscopy-based technique, DDM is also naturally suited to characterizing dynamics in quasi-two-dimensional systems when direct tracking is not feasbible, as in our case with the bacteria in biofilms. DDM has been performed previously on suspensions of motile bacteria, as well as other soft and living matter, and has been shown to be a useful tool, for example, for extracting a diffusion constant of swimming bacteria [160][oth-

ers]. If the dynamics of the moving particles being imaged are uncorrelated and obey Gaussian statistics, $g(q,t)$ can be related to the particle MSD,

$$g(q,t) = e^{-q\langle \Delta r^2(t)\rangle/4}. \tag{5.14}$$

Hence, for particles undergoing simple diffusion, the intermediate scattering function has an exponential form, $g(q,t) = e^{-t/\tau}$, where $\tau = 1/Dq^2$, and D is the diffusion coefficient.

Figure 5.9(a) displays DDM results obtained from images of an interface at an early age, $t_a = 1$ hr, prior to biofilm formation. The figure shows $1 - g(q,t)$ over the range of $0.1 < q < 5.7$ μm^{-1} along with the results of best fits to the data assuming a diffusive, exponential form. Specifically, a fit to $D(q,t)$ is made at each wave vector with $\tau(q)$, $A(q)$, and $B(q)$ as parameters, and the resulting $A(q)$ and $B(q)$, which are provided in Fig. 5.17 of the Appendix along with additional analysis details, are used to extract the values of $1-g(q,t)$ and the fit results shown. Figure 5.10 displays τ as a function of q on a log-log plot. The line in the figure shows the result of a fit with the diffusive form, $\tau = 1/Dq^2$, which describes the data well, except perhaps at the lowest q. We note, however, $1-g(q,t)$ fails to reach its terminal plateau within the measured range of lag times at these lowest q, introducing greater uncertainty to the fitting at these wave vectors. Thus, the bacteria undergo diffusive dynamics at the interface at early ages. The diffusion constant obtained from the fit is $D = 0.86 \pm 0.01$ $\mu\text{m}^2/\text{s}$. For comparison, a sphere of diameter 4 μm undergoing thermal diffusion in water at room temperature has $D = 0.1$ $\mu\text{m}^2/\text{s}$. This diffusive motion to the largest wave vectors is a

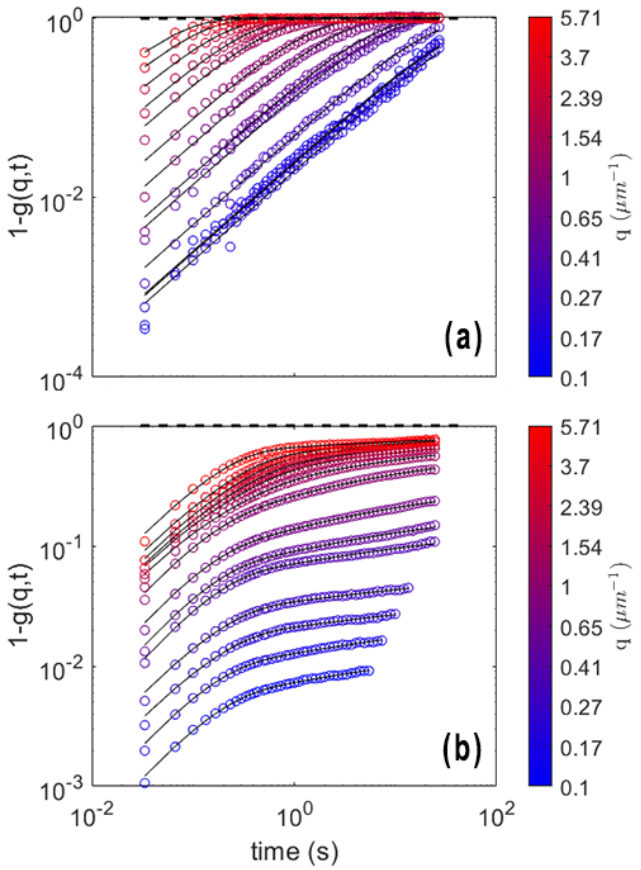

Figure 5.9: One minus the intermediate scattering function obtained from DDM measurements of an interface at ages of 1 (a) and 7 (b) hours. The data are color-coded by the values of the wave vector q. The solid curves are fits to the data, as described in the text.

bit surprising since on the shortest lengthscales the swimming motion of the bacteria should lead to ballistic behavior, $\tau \sim q^{-1}$. We can estimate a lower bound for the lengthscale l_D at which the motion crosses over to diffusion from the value of the largest measurement wave vector, $l_D \approx q_{max}^{-1} = 5.7^{-1}$ μm ≈ 0.18 μm, which is only a small fraction of the bacteria body length, indicating the concentration of bacteria is such that their mean-free path is small.

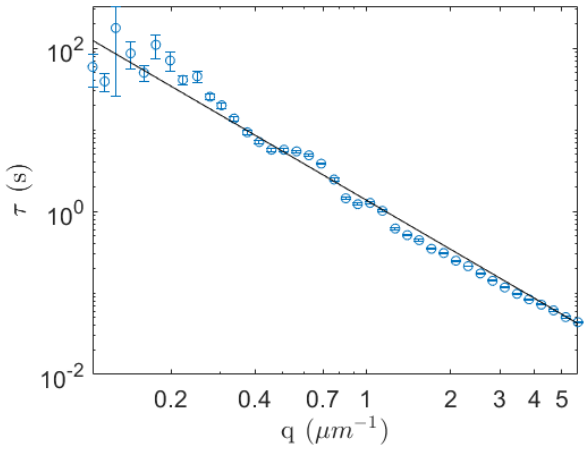

Figure 5.10: A log-log plot of the correlation time τ as a function wave vector q obtained from fits to $D(q,t)$ for the interface at age $t_a = 1$ hr. The solid line is a fit using the form $\tau \sim q^{-2}$ characteristic of diffusive dynamics.

Once the viscoelastic biofilm forms, $g(q,t)$ no longer reaches zero over the range of measured lag times at any wave vector, signalling constrained motility of the bacteria. This loss of ergodicity creates a problem in the analysis, because if $D(q,t)$ does not reach a plateau that can be confidently associated with the terminal plateau of $g(q,t)$, the factors $A(q)$ and $B(q)$ cannot be unambiguously determined. To circumvent this difficulty, we conducted DDM analysis of the microscopy images in which we shifted the images relative to each other at regular time intervals, which created an artificial de-correlation between images that forced $g(q,t)$ to zero at large lag times and enabled us to extract values for $A(q)$ and $B(q)$. Details regarding this analysis procedure are provided in the Appendix. An example of results from this analysis is displayed in Fig. 5.9(b), which shows $1 - g(q,t)$ from a measurement at interface age $t_a = 7$ hrs. (In Fig. 5.9(b), the data at large lag times at low values of q are discarded due to

upward curvature of the data that we associate with the effects of residual drift.) The intermediate scattering functions show an initial decay at short lag times to a quasi-plateau at a value that depends on wave vector, followed by a much slower variation at larger lag times. DDM measurements on interfaces at other late ages ($t_a > 5$ hrs) gave similar results. Such partial decays in the correlations to a quasi-plateau are familiar from glassy fluids where the decay is associated with localized, caged motion of the particles. With formation of the biofilm, the bacteria motility apparently becomes similarly constrained.

To analyze the bacteria dynamics in the biofilm quantitatively, we fit the intermediate scattering functions using a sum of an exponential and a power-law to capture the initial decay at small lag times and the slow relaxation at large lag times, respectively,

$$g(q,t) = \lambda e^{-t/\tau_1} + (1-\lambda)(\frac{t+\tau_2}{\tau_2})^{-\alpha}. \tag{5.15}$$

Results of such fits are are shown by the lines in Fig. 5.9(b). The fit parameters τ_1 and τ_2, along with further details regarding the fitting procedure, are described in the Appendix. Here, we focus on interpreting the other fit parameters λ and α, which characterize the magnitude of the initial decay and the late-time power-law behavior, respectively. As mentioned above, the initial decay in $g(q,t)$ is indicative of constrained, localized motion of the bacteria on short timescales. Following Eq. (5.14), for particle motion restricted to an average localization length r_{loc}, $g(q,t)$ decays to $e^{-r_{loc}^2 q^2/4}$, or equivalently from Eq. (5.15), $1-\lambda = e^{-r_{loc}^2 q^2/4}$. Figure 5.11(b) displays

$\ln(1-\lambda)$ plotted against q^2. Over much of the measured range, the expected linear form is observed. The line in Fig. 5.11(b) displays the result of a linear fit to the data for $q^2 > 10\ \mu\text{m}^{-2}$. From the slope of the linear fit, we find $r_{loc} = 0.15\ \mu$m. In principle, the predicted linear from should have an intercept of zero. The non-zero y-intercept of the fit result could be due to either a contribution to the DDM signal from bacteria that are not localized, for example bacteria that are moving in the aqueous phase above the biofilm, or from small systematic errors in $A(q)$ at low q, where the factor has the greatest uncertainty.

The dynamics of the bacteria in the biofilm are not bounded by r_{loc} on all time scales; however, as the power-law decay in $g(q,t)$ indicates slow, de-localized motion. Figure 5.11(a) displays the power-law exponents α obtained from the fits shown in Fig. 5.9(b) as a function of wave vector. The exponents have dependence of wave vector whose origin is not immediately clear, but they maintain small values, $\alpha < 0.2$, over the full range. This weak power-law behavior is similar to the weak power-law growth of the MSDs of the 1-μm and 4-μm colloids at late interface age seen in Fig. 5.2, suggesting the long-time dynamics of the bacteria in the biofilm resembles that of the passive tracers.

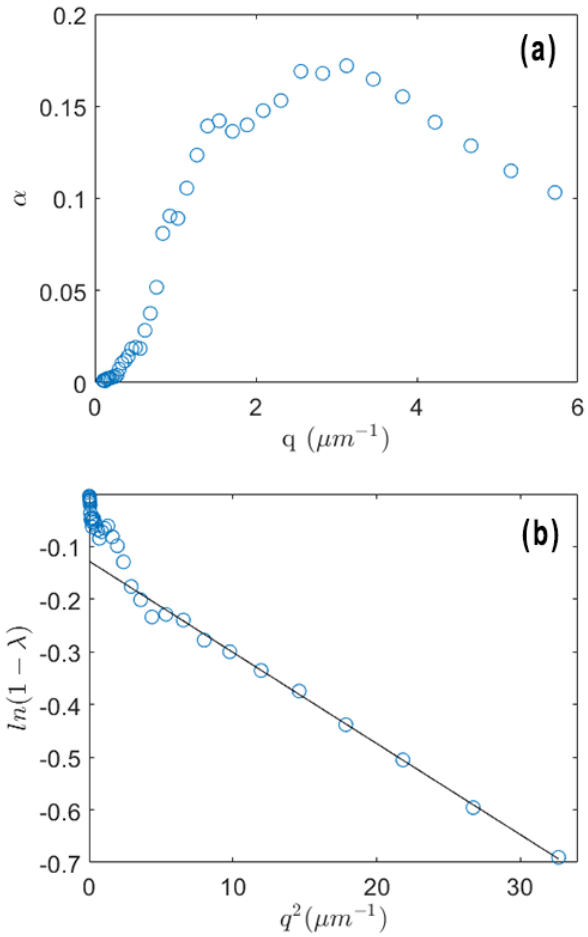

Figure 5.11: (a) The power-law exponent α characterizing the large lag-time decay of $g(q,t)$ from the DDM measurements at interface age $t_a = 7$ hr (b) Logarithm of one minus λ, the value of the quasi-plateau in $g(q,t)$, as a function of wave-vector squared. The solid line shows the result of a linear fit.

5.4 Discussion and Conclusion

Taken as a whole, the DDM measurements provide a picture of the bacteria dynamics at the interface in which the dynamics evolve from diffusive motion characteristic of a concentrated but disordered assembly of unconstrained swimming bacteria at early age to constrained but ultimately unbounded motion within the viscoelastic biofilm at later age. Details aside, a key observation from the DDM measurements is the continued motility of the bacteria in the biofilm at late age, which presumably affects the motion of the spheres in the passive particle tracking measurements and explains, at least in part, the decoupling of the motion of the 1-μM and 4-μm spheres from the film rheology. The fact that these spheres, which are much more strongly affected than the 15-μm sphere, are similar in size to the bacteria themselves seems unlikely to be a coincidence. Indeed, when a colloidal probe is comparable in size to the constituent particles of the medium, the validity of typical macroscopically derived formulas can no longer be assumed to hold [21]. An interesting question is how the large-time, slow dynamics of the bacteria captured in the DDM might reflect the same "passive" motion experienced by the smaller spheres. That is, one has a picture in which they become caught in the viscoelastic solid biofilm but nevertheless continue to exert forces on the environment. This activity provides a nonthermal energy source that ultimately leads to delocalization of the bacteria.

5.5 Appendix

5.5.1 MSDs of Colloidal Spheres

Displayed in Fig. 5.12 are the MSDs of passively moving spherical colloids during biofilm formation obtained from additional trials and at additional ages than those shown in the main text. Shown in Fig. 5.13 are the power-law exponents and the value of the MSD at a time lag of 1 s as a function of biofilm age for several different trials.

5.5.2 Velocity Correlations of Spherical Colloids

As further evidence that the spheres' motion is consistent with their being in a viscoelastic environment, the velocity-velocity correlations of the particles agree well with a fractional-Brownian-motion model, which is often used to model the motion of particles in viscoelastic materials [references]. Details of this model can be found in [158]. The velocity correlation is defined as follows,

$$C_v^{\delta}(t) = \langle \mathbf{v}(t+\tau) \cdot \mathbf{v}(t) \rangle \tag{5.16}$$

where the velocity between frames separated by lag time δ is defined as

$$\mathbf{v}(t) = \frac{1}{\delta}(\mathbf{r}(t+\delta) - \mathbf{r}(t)) \tag{5.17}$$

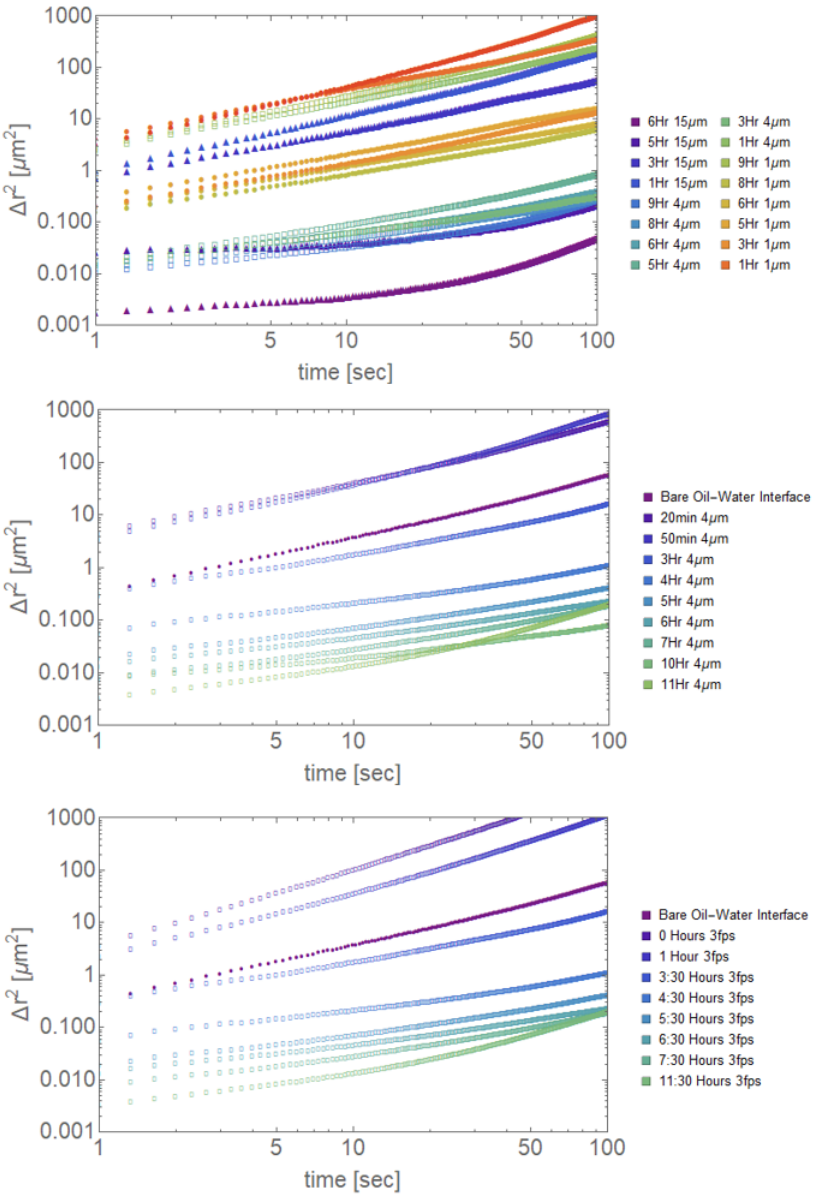

Figure 5.12: (a) Mean-squared displacements of 1-μm, 4-μm, and 15-μm diameter spherical particles in the pre-biofilm and biofilm-forming stages of the interface. All measurements were performed at 3 fps. (b) and (c) MSD of 4-μm spheres as a function of biofilm age from two additional trials.

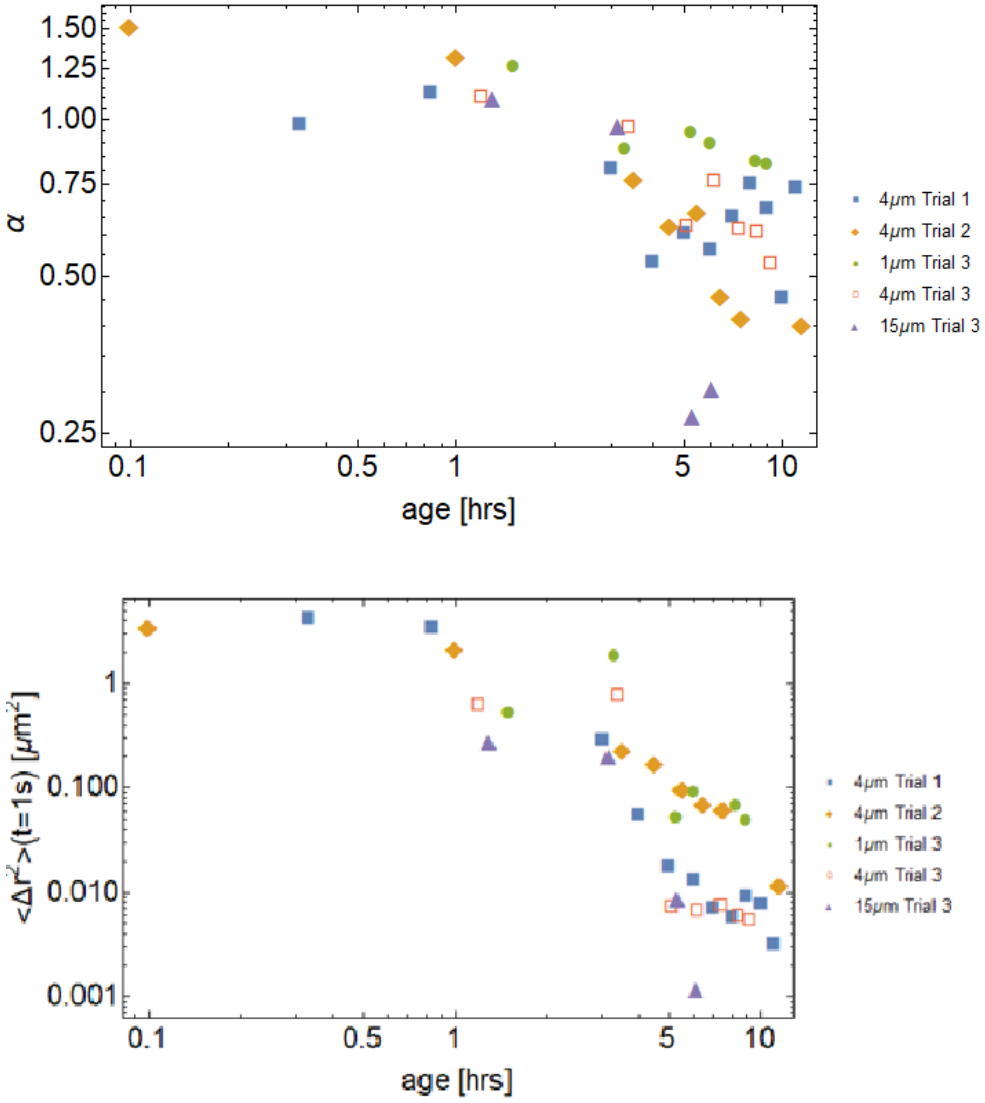

Figure 5.13: (a) Exponents characterizing the power-law behavior of the MSDs obtained in three different trials. (b) The value of the MSD at a lag time of 1 s obtained in three different trials.

With this model, the predicted velocity correlations are

$$C_v^\delta(\tau) = \begin{cases} \frac{C_v(\tau)}{\kappa^2\alpha(1-\alpha)}2 - (1-\kappa)^\alpha - (1+\kappa)^\alpha, & \text{for } \tau \geq \delta \\ \frac{C_v(\tau)}{\kappa^2\alpha(1-\alpha)}2 - (1-\kappa)^\alpha - (1+\kappa)^\alpha + & \\ \frac{3k_BT}{6\pi\alpha\eta}\frac{\sin(\alpha\pi)}{\pi(1-\alpha)(1-\frac{\alpha}{2})\alpha\delta^2}(\delta-\tau)^\alpha, & \text{for } \tau < \delta \end{cases} \tag{5.18}$$

where $\kappa = \delta/\tau$, α is the power-law exponent of the MSD, and $C_v(\tau) = \frac{-3k_BT}{6\pi\alpha\eta}\frac{\sin(\alpha\pi)}{\pi(2-\alpha)}|\tau^{\alpha-2}|$. One can show that the normalized and re-scaled velocity correlation,

$$\frac{C_v^\delta(\tau/\delta)}{C_v^\delta(0)} \tag{5.19}$$

collapses onto one master curve for all values of δ. We plot the normalized velocity correlations along with a fit to the fractional-Brownian-motion model in Fig. 5.14. The value for α is chosen based on a fit to the MSD, therefore the curve has no free parameters. We find that the data agrees well with the theoretical curve for $\delta \geq 10$. For values of δ lower than this, the anti-correlation persists to longer lag times than is predicted by the model.

The experimental velocity correlations are first found according to equation 5.16 and 5.17 for each value of τ given a particular value of δ. For each value of δ, the results are averaged over all particles and all time-lags equal to τ. Finally, a normalization is done by dividing $C_v(\tau)$ by $C_v(0)$. This process is repeated for each value of δ.

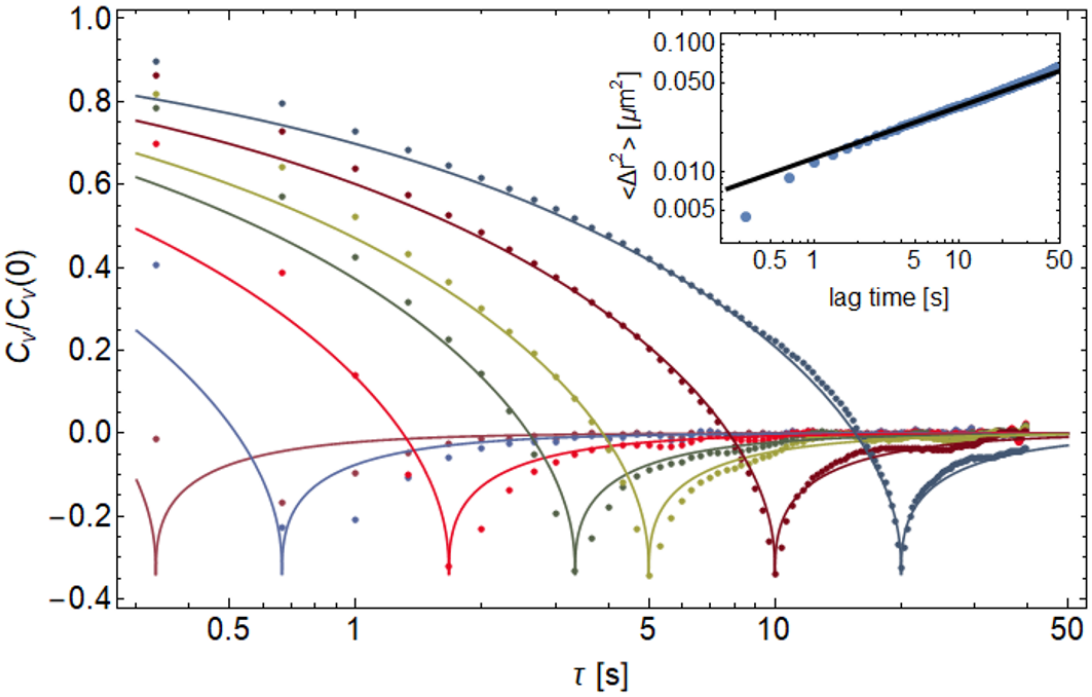

Figure 5.14: Normalized velocity correlations, shown for $\delta = 1/3$, $2/3$, $5/3$, $10/3$, 5, 10, and 20 s. The solid lines are the theoretical curves based on the fractional-Brownian-motion model with $\alpha = 0.4$, the exponent of the power-law MSD shown in the inset.

5.5.3 Wire Fit Parameters

Shown in Fig. 5.15 are the fit parameters obtined from analysis of active microrheology measurements with the ferromagnetic rods employing a double Kelvin-Voigt model to fit data for the rods' rotational motion, as described in the main text. Results from five separate trials are shown. Generally, they all show similar trends, although the trial-to-trial variation is significant.

5.5.4 Differential Dynamic Microscopy Analysis Procedure

DDM analysis was performed on bright-field images acquired at 30 fps with a resolution of $2048x2048$ pixels. The analysis resulted in value for $D(q,t)$ within a binned set of wave vectors q, at each lag time t. To decrease the calculation time, and because of the nature of the intermediate scattering function, the analysis was performed on exponentially spaced time lags. The analysis typically resulted in approximately 1448 unique values of q and 60 unique time lags. The results were further binned using an exponential spacing of q in order to reduce the computational time in fitting $D(q,t)$. The bin spacing Δq was chosen such that $\Delta q/q$ was approximately 0.1, which was deemed adequate resolution given the lack of sharp features in $D(q,t)$ as a function of q. The range of q was limited to $q = 0.1 - 5\ \mu\ \mathrm{m}^{-1}$ in order to retain only the statistically most robust $D(q,t)$ with the largest signal-to-noise ratio.

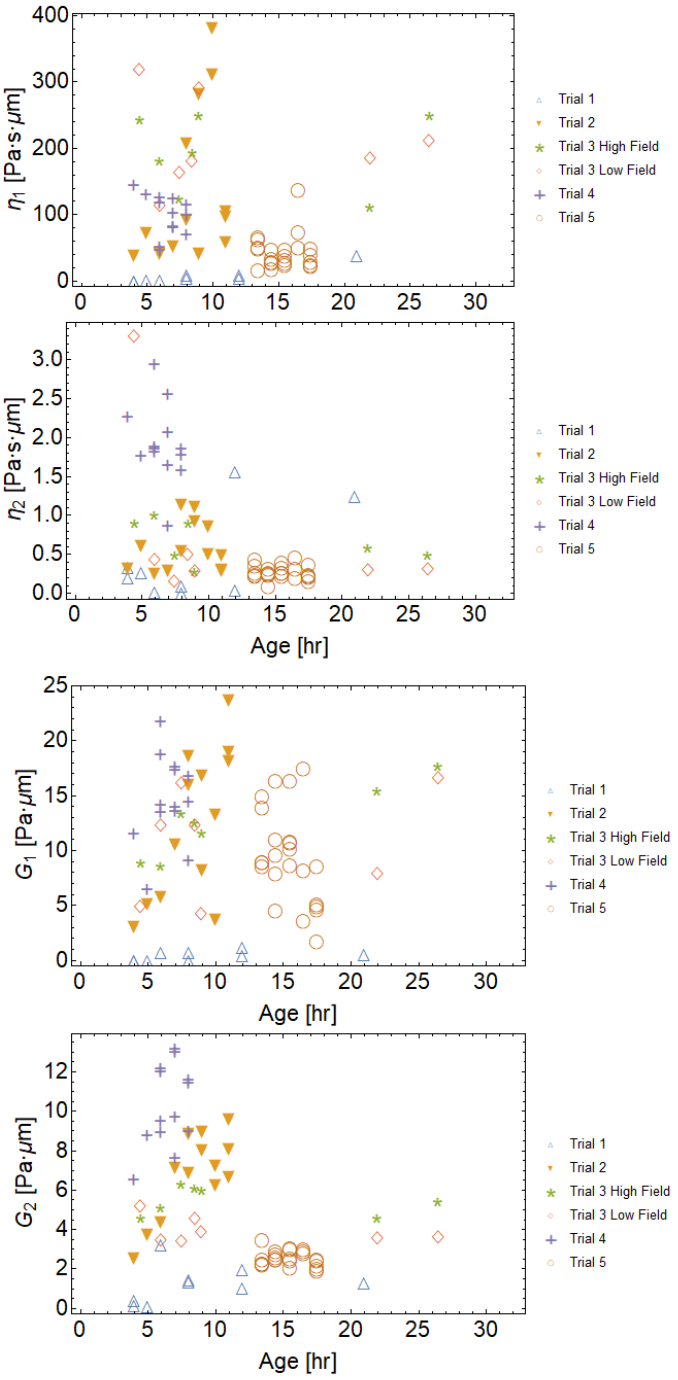

Figure 5.15: The viscoelastic model parameters as a function of biofilm age, as determined by performing a least-squares fitting procedure to the data obtained in several trials using a double Kelvin-Voigt model, as depicted in Fig. 5.8

As described in the main text, a challenge in DDM was to determine whether $g(q,t)$ was ergodic and hence $D(q,t)$ reached a terminal plateau corresponding to $g(q,t) \to 0$. To test whether this condition was met, we conducted a separate DDM analysis on the videos in which a subset of the images were digitally translated, thus ensuring complete decorrelation of the ISF while maintaining approximately the same structure and noise of the original video. Approximately every 160th image (approximately every 5.3 s or about 1/5 of the total number of frames) was translated by 300 pixels: first to the right, then left, then down, then up, relative to the original image. The choice of 300 pixels, or 83 μm, was made because it was small enough not to appreciably alter the region over which the analysis was performed, while also being large enough to decorrelate the images over length scales greater than q^{-1}, even for the smallest wave vector 0.1 μ m^{-1}) included in the analysis. A comparison of the resulting $D(q,t)$ at $t_a = 1$ hr and 7 hrs obtained with and without the shift introduced are shown in Fig. 5.16. The difference in the results at $t_a = 1$ hr is minor, consistent with our assumption that the measurements at early age were ergodic; that is, that $D(q,t)$ reached a terminal plateau corresponding to $g(q,t) \to 0$. However, the difference in results at $t_a = 7$ hrs is more significant, indicating the measurements at later ages were not ergodic. Note $D(q,t)$ at $t_a = 7$ hrs in which the images were shifted shows a sharp kink at $t = 5.3$ s, corresponding the artificially imposed decorrelation. The plateau values these $D(q,t)$ at greater lag times provided a means to analyze the late-age results.

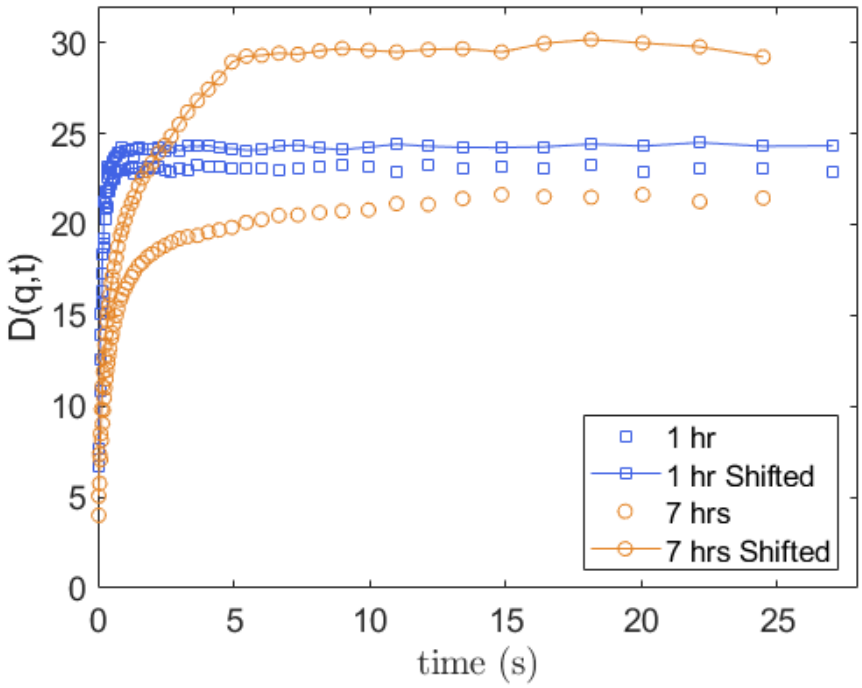

Figure 5.16: A comparison of $D(q,t)$ as found from a bright-field video of the interface with that of the same video in which the images were digitally translated. Results are shown at ages of 1 hour (blue squares) and 7 hours (orange circles), both at a wave vector of $q = 3\ \mu\text{m}^{-1}$. The video in which the frames were artificially translated produces a plateau in $D(q,t)$ at lag times that are greater than the interval between translations, which is approximately 5.3 seconds. The large difference in $D(q,t)$ between the translated and original videos at 7 hours, compared to the negligible difference between the two at 1 hour, indicates a lack of complete decay of the ISF at the later age.

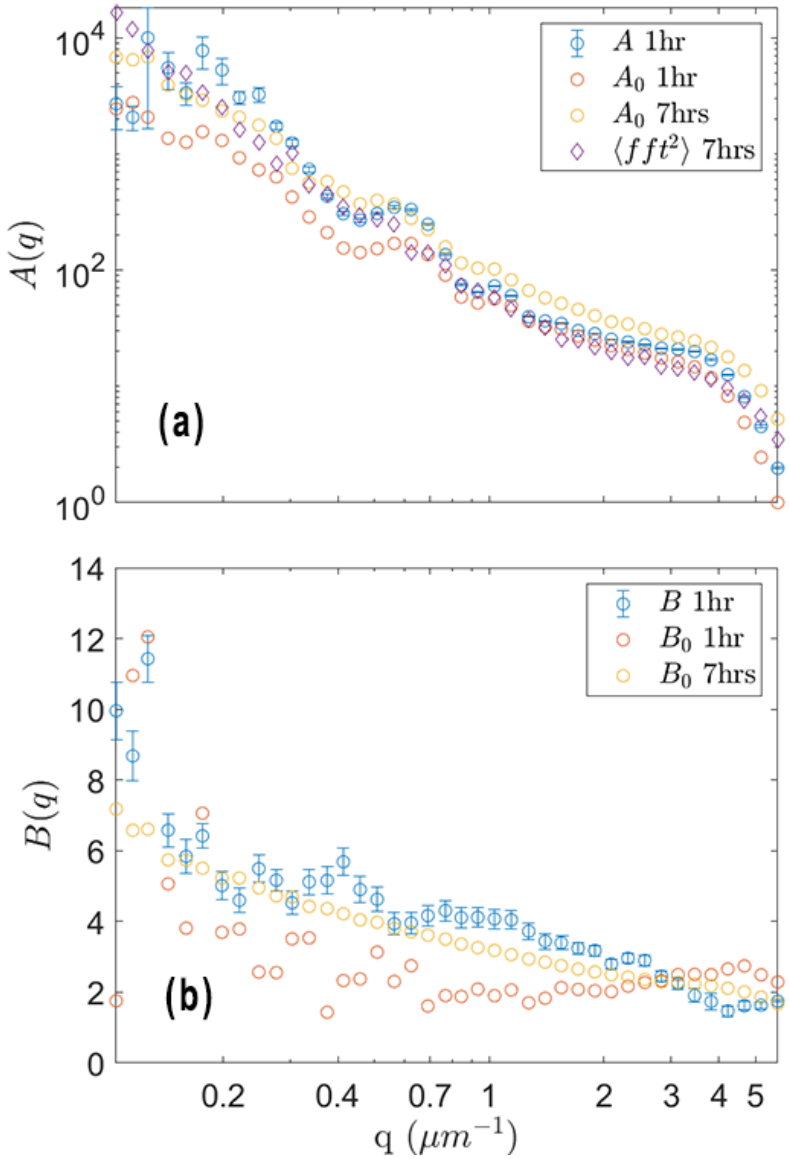

Figure 5.17: The parameters $A(q)$ and $B(q)$ at interface ages of 1 and 7 hours. (a) The scaling parameter $A(q)$, as found from the exponential fits to the data at an age of 1 hour, along with the plateau of $D(q,t)$, $A_0(q)$, found from the digitally translated frames at both an age of 1 and 7 hours. Also shown is the average squared fast Fourier transform of the bright-field images at 7 hours. (b) The value of $B(q)$ found from the fits, as well as the estimate, $B_0(q)$ at both 1 and 7 hours.

For analysis of $D(q,t)$ at $t_a = 1$ hr, since the measurements were apparently ergodic, the data were analyzed accordingly. As described in the main text, $D(q,t)$ at each q was fit using a model of diffusive dynamics for $g(q,t)$,

$$D(q,t) = A(q)(1 - \exp(-t/\tau(q))) + B(q) \tag{5.20}$$

with $\tau(q)$, $A(q)$, and $B(q)$ as free parameters. To obtain initial guesses for each parameter, the following procedure was employed. First, a linear fit to $D(q,t)$ from the analysis with artificial shifts was performed using the data at small lag times, and the y-intercepts of those fits were used as the initial guesses for $B(q)$. Then, the differences between large-lag-time plateaus of $D(q,t)$ from the analysis with artificial shifts and these y-intercepts values were obtained, and these were used as the initial estimates of $A(q)$, The estimates are shown in Fig. 5.17 as $A_0(q)$ and $B_0(q)$. Finally, initial guesses for $\tau(q)$ at $t_a = 1$ hr were made by assuming $\tau \sim q^{-2}$. In the fitting, constraints are put on $A(q)$, $B(q)$, and $\tau(q)$ to guide the optimizer to only search a reasonable domain of parameter space. All of the parameters were constrained to be greater than zero, while $A(q)$ was also constrained to be less than 10^4. The final results for $\tau(q)$ are shown in Fig. 5.10. Figure 5.17 shows the final results for $A(q)$ and $B(q)$.

The large discrepancy at $t_a = 7$ hrs between $D(q,t)$ obtained with and without artificially de-correlating the images indicates the measurements were not ergodic; that is, $g(q,t)$ failed to decay fully to zero over the range of measured lag times. In such cases, one cannot directly obtain a reliable estimate of $D(q,t)$ on an absolute

scale. Therefore, from $D(q,t)$ of the artificially shifted data, we obtained values of $A(q)$ and $B(q)$ that we used in the analysis of the results from the unaltered images. Specifically, we followed the same procedure we employed to obtain initial guesses for $A(q)$ and $B(q)$ at $t_a = 1$ hr, but in this case we kept those values fixed in the subsequent analysis. These values for $A(q)$ and $B(q)$ at $t_a = 7$ hrs are shown in Fig. 5.17. As a cross-check, also shown in Fig. 5.17(a) is the squared Fourier transform of the bright-field images at $t_a = 7$ hrs averaged over the video. One can show that the averaged squared Fourier transform is proportional to $A(q)$, and indeed our estimate of $A(q)$ demonstrates this well. Notably, we find little qualitative difference between the average Fourier transform of the images at 1 and 7 hours. Therefore, the similarity of $A(q)$ between these two ages is also reasonable.

With $A(q)$ and $B(q)$ fixed in this way, we fit each $D(q,t)$ at $t_a = 7$ hrs using Eq. 5.15 allowing τ_1, τ_2, λ, and α to vary with the constraint that all parameters be greater than zero. Initial estimates for τ_1 and τ_2 were 0.5 s and 0.01 s, respectively. We also constrained τ_2 to be less than 0.1 s to prevent the algorithm from incorporating it too strongly into the fit, as it is merely included to keep the modeled ISF physical. Based on the results of preliminary fits, we obtained power-law initial estimates for λ and α by assuming continuity of the parameters, which produced a good degree of consistency in the fit results. Fig. 5.18 displays the resulting fit parameters τ_1 and τ_2. Although on several occasions τ_2 reaches the maximum value it is allowed to by the constraint, we find that the fit result is largely insensitive to its precise value.

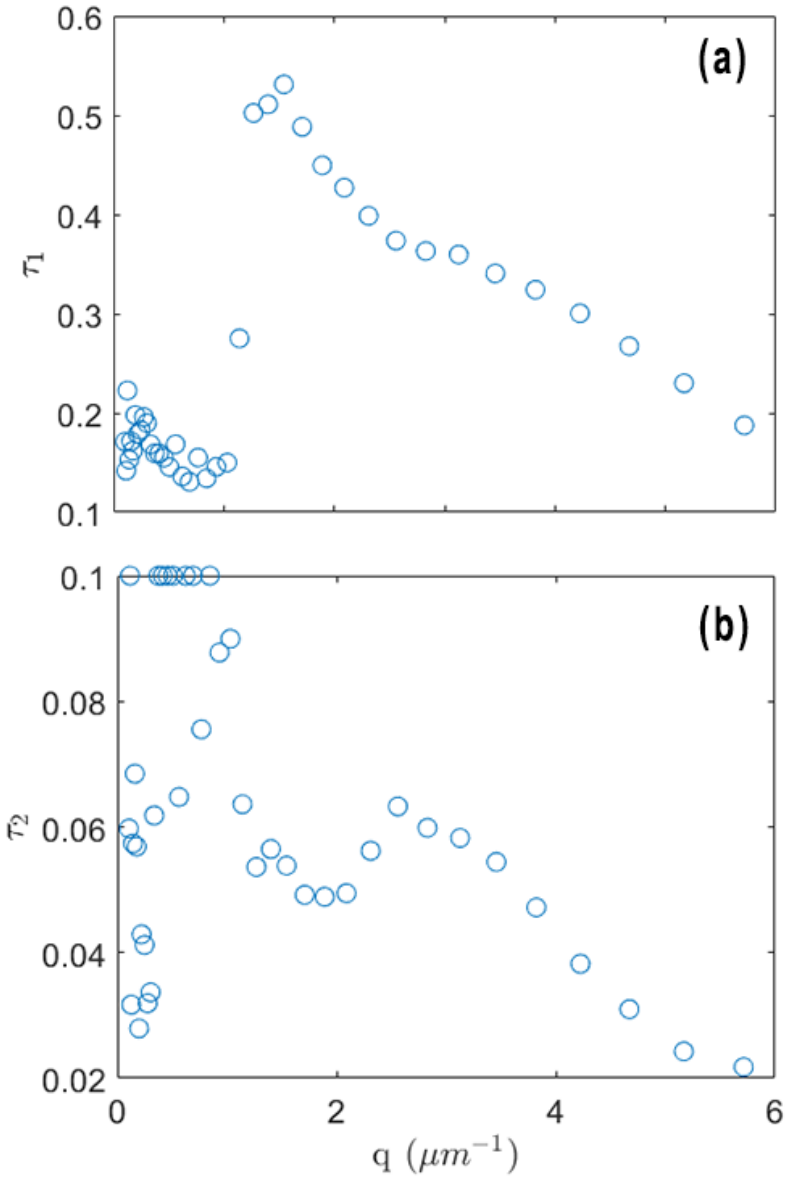

Figure 5.18: The fit parameters τ_1 (a) and τ_2 (b) found from fits to $D(q,t)$ at an age of 7 hours, as explained in the main text.

Bibliography

[1] A.A. Abrikosov. *Fundamentals of the Theory of Metals*. North-Holland, 1988.

[2] A. C. Aitken. Iv.—on least squares and linear combination of observations. *Proceedings of the Royal Society of Edinburgh*, 55:42–48, 1936.

[3] Daniel B. Allan, Thomas A. Caswell, Nathan Keim, Fred Boulogne, Rick W. Perry, and Lucy Uieda. trackpy: Trackpy v0.3.3. 2014.

[4] Daniel B. Allan, Daniel M. Firester, Victor P. Allard, Daniel H. Reich, Kathleen J. Stebe, and Robert L. Leheny. Linear and nonlinear microrheology of lysozyme layers forming at the air–water interface. *Soft Matter*, 10:7051–7060, 2014.

[5] Denis Andrienko. Introduction to liquid crystals. *Journal of Molecular Liquids*, 267:520 – 541, 2018. Special Issue Dedicated to the Memory of Professor Y. Reznikov.

[6] Paula A. Araújo, Joana Malheiro, Idalina Machado, Filipe Mergulhão, Luís

Melo, and Manuel Simões. Influence of flow velocity on the characteristics of ¡i¿pseudomonas fluorescens¡/i¿ biofilms. *Journal of Environmental Engineering*, 142(7):04016031, 2016.

[7] Aykut Argun, Ali-Reza Moradi, Erça ğ Pinçe, Gokhan Baris Bagci, Alberto Imparato, and Giovanni Volpe. Non-boltzmann stationary distributions and nonequilibrium relations in active baths. *Phys. Rev. E*, 94:062150, Dec 2016.

[8] Ilene D. Auerbach, Cody Sorensen, Helen G. Hansma, and Patricia A. Holden. Physical morphology and surface properties of unsaturated pseudomonas putida biofilms. *Journal of Bacteriology*, 182(13):3809–3815, 2000.

[9] Nicole Billings, Alona Birjiniuk, Tahoura S Samad, Patrick S Doyle, and Katharina Ribbeck. Material properties of biofilms—a review of methods for understanding permeability and mechanics. *Reports on Progress in Physics*, 78(3):036601, feb 2015.

[10] G. Birkhoff. *Hydrodynamics*. Princeton Legacy Library. Princeton University Press, 2015.

[11] Åke Björck. *Numerical Methods for Least Squares Problems*. Society for Industrial and Applied Mathematics, 1996.

[12] Héloïse Boudarel, Jean-Denis Mathias, Benoît Blaysat, and Michel Grédiac. To-

wards standardized mechanical characterization of microbial biofilms: analysis and critical review. *npj Biofilms and Microbiomes*, 4(1):17, August 2018.

[13] Henrik Bruus. *Theoretical Microfluidics*. Oxford Master Series in Physics. Oxford University Press Oxford, 2008.

[14] Markus Böl, Alexander E. Ehret, Antonio Bolea Albero, Jan Hellriegel, and Rainer Krull. Recent advances in mechanical characterisation of biofilm and their significance for material modelling. *Critical Reviews in Biotechnology*, 33(2):145–171, 2013.

[15] Michael E. Cates and Julien Tailleur. Motility-induced phase separation. *Annual Review of Condensed Matter Physics*, 6(1):219–244, 2015.

[16] P.M. Chaikin and T.C. Lubensky. *Principles of Condensed Matter Physics*. Cambridge University Press, 2000.

[17] D. T. N. Chen, A. W. C. Lau, L. A. Hough, M. F. Islam, M. Goulian, T. C. Lubensky, and A. G. Yodh. Fluctuations and rheology in active bacterial suspensions. *Phys. Rev. Lett.*, 99:148302, Oct 2007.

[18] L. Chevry, N. K. Sampathkumar, A. Cebers, and J.-F. Berret. Magnetic wire-based sensors for the microrheology of complex fluids. *Phys. Rev. E*, 88:062306, Dec 2013.

[19] Frank Cichos, Kristian Gustavsson, Bernhard Mehlig, and Giovanni Volpe. Machine learning for active matter. *Nature Machine Intelligence*, 2(2):94–103, 2020.

[20] Frank Cichos, Kristian Gustavsson, Bernhard Mehlig, and Giovanni Volpe. Machine learning for active matter. *Nature Machine Intelligence*, 2(2):94–103, 2020.

[21] Diego Coglitore, Stuart P. Edwardson, Peter Macko, Eann A. Patterson, and Maurice Whelan. Transition from fractional to classical stokes–einstein behaviour in simple fluids. *Royal Society Open Science*, 4(12):170507, 2017.

[22] Rémy Colin, Loudjy Chevry, Jean-François Berret, and Bérengère Abou. Rotational microrheology of maxwell fluids using micron-sized wires. *Soft Matter*, 10:1167–1173, 2014.

[23] John C. Crocker and David G. Grier. Methods of digital video microscopy for colloidal studies. *Journal of Colloid and Interface Science*, 179(1):298 – 310, 1996.

[24] P.G. de Gennes and J. Prost. *The Physics of Liquid Crystals*. International Series of Monogr. Clarendon Press, 1993.

[25] Stephen J. DeCamp, Gabriel S. Redner, Aparna Baskaran, Michael F. Hagan,

and Zvonimir Dogic. Orientational order of motile defects in active nematics. *Nature Materials*, 14:1110, 2015.

[26] D. Dell'Arciprete, M. L. Blow, A. T. Brown, F. D. C. Farrell, J. S. Lintuvuori, A. F. McVey, D. Marenduzzo, and W. C. K. Poon. A growing bacterial colony in two dimensions as an active nematic. *Nature Communications*, 9(1):4190, October 2018.

[27] C. Denniston, D. Marenduzzo, E. Orlandini, and J.M. Yeomans. Lattice boltzmann algorithm for three-dimensional liquid-crystal hydrodynamics. *Philosophical Transactions of the Royal Society of London. Series A: Mathematical, Physical and Engineering Sciences*, 362(1821):1745–1754, 2004.

[28] Christopher Dombrowski, Luis Cisneros, Sunita Chatkaew, Raymond E. Goldstein, and John O. Kessler. Self-concentration and large-scale coherence in bacterial dynamics. *Phys. Rev. Lett.*, 93:098103, Aug 2004.

[29] Christopher Dombrowski, Luis Cisneros, Sunita Chatkaew, Raymond E. Goldstein, and John O. Kessler. Self-concentration and large-scale coherence in bacterial dynamics. *Phys. Rev. Lett.*, 93:098103, 2004.

[30] Rodney M. Donlan. Biofilms: Microbial life on surfaces. *Emerging Infectious Disease journal*, 8(9):881, 2002.

[31] Amin Doostmohammadi, Michael F Adamer, Sumesh P Thampi, and Julia M

Yeomans. Stabilization of active matter by flow-vortex lattices and defect ordering. *Nature communications*, 7:10557, 2016.

[32] Amin Doostmohammadi, Tyler N Shendruk, Kristian Thijssen, and Julia M Yeomans. Onset of meso-scale turbulence in active nematics. *Nature Communications*, 8:15326, 2017.

[33] J Elgeti, R G Winkler, and G Gompper. Physics of microswimmers—single particle motion and collective behavior: a review. *Reports on Progress in Physics*, 78(5):056601, apr 2015.

[34] Benjamin Erable, Narcis M. Duţeanu, M.M. Ghangrekar, Claire Dumas, and Keith Scott. Application of electro-active biofilms. *Biofouling*, 26(1):57–71, 2010. PMID: 20390557.

[35] Herbert H.P Fang, Kwong-Yu Chan, and Li-Chong Xu. Quantification of bacterial adhesion forces using atomic force microscopy (afm). *Journal of Microbiological Methods*, 40(1):89 – 97, 2000.

[36] Edward J. Felton and Daniel L. Leheny. *Applications of magnetic nanostructures to cell patterning and heterotypic cell -cell interactions*. PhD thesis, The Johns Hopkins University, Ann Arbor, 2009.

[37] Albert Fert, Nicolas Reyren, and Vincent Cros. Magnetic skyrmions: Advances

in physics and potential applications. *Nature Reviews Materials*, 2:17031, June 2017.

[38] Hans-Curt Flemming and Jost Wingender. The biofilm matrix. *Nature Reviews Microbiology*, 8(9):623–633, September 2010.

[39] G. Foffano, J. S. Lintuvuori, K. Stratford, M. E. Cates, and D. Marenduzzo. Colloids in active fluids: Anomalous microrheology and negative drag. *Phys. Rev. Lett.*, 109:028103, Jul 2012.

[40] F. C. Frank. I. liquid crystals. on the theory of liquid crystals. *Discuss. Faraday Soc.*, 25:19–28, 1958.

[41] B. Frka-Petesic, K. Erglis, J.F. Berret, A. Cebers, V. Dupuis, J. Fresnais, O. Sandre, and R. Perzynski. Dynamics of paramagnetic nanostructured rods under rotating field. *Journal of Magnetism and Magnetic Materials*, 323(10):1309 – 1313, 2011. Proceedings of 12th International Conference on Magnetic Fluid.

[42] Fred Fu. Formation and field-switching dynamics of nematic droplets. 2017.

[43] C.A. Fux, J.W. Costerton, P.S. Stewart, and P. Stoodley. Survival strategies of infectious biofilms. *Trends in Microbiology*, 13(1):34 – 40, 2005.

[44] Fabio Giavazzi, Doriano Brogioli, Veronique Trappe, Tommaso Bellini, and

Roberto Cerbino. Scattering information obtained by optical microscopy: Differential dynamic microscopy and beyond. *Phys. Rev. E*, 80:031403, Sep 2009.

[45] Félix Ginot, Isaac Theurkauff, Demian Levis, Christophe Ybert, Lydéric Bocquet, Ludovic Berthier, and Cécile Cottin-Bizonne. Nonequilibrium equation of state in suspensions of active colloids. *Phys. Rev. X*, 5:011004, Jan 2015.

[46] L. Giomi, N. Hawley-Weld, and L. Mahadevan. Swarming, swirling and stasis in sequestered bristle-bots. *Proceedings of the Royal Society A: Mathematical, Physical and Engineering Sciences*, 469(2151):20120637, 2013.

[47] Luca Giomi. Geometry and topology of turbulence in active nematics. *Phys. Rev. X*, 5:031003, Jul 2015.

[48] Giuseppe Gonnella, Davide Marenduzzo, Antonio Suma, and Adriano Tiribocchi. Motility-induced phase separation and coarsening in active matter. *Comptes Rendus Physique*, 16(3):316 – 331, 2015. Coarsening dynamics / Dynamique de coarsening.

[49] P. Guillamat, J. Ignés-Mullol, and F. Sagués. Taming active turbulence with patterned soft interfaces. *Nature Communications*, 8(1):564, September 2017.

[50] Pau Guillamat, Jordi Ignés-Mullol, and Francesc Sagués. Control of active liquid crystals with a magnetic field. *Proceedings of the National Academy of Sciences*, 113(20):5498–5502, 2016.

[51] Pau Guillamat, Jordi Ignés-Mullol, Suraj Shankar, M. Cristina Marchetti, and Francesc Sagués. Probing the shear viscosity of an active nematic film. *PRE*, 94(6):060602, December 2016.

[52] Emily C. Hollenbeck, Jiunn C.N. Fong, Ji Youn Lim, Fitnat H. Yildiz, Gerald G. Fuller, and Lynette Cegelski. Molecular determinants of mechanical properties of v. cholerae biofilms at the air-liquid interface. *Biophysical Journal*, 107(10):2245 – 2252, 2014.

[53] Ali Houry, Michel Gohar, Julien Deschamps, Ekaterina Tischenko, Stéphane Aymerich, Alexandra Gruss, and Romain Briandet. Bacterial swimmers that infiltrate and take over the biofilm matrix. *Proceedings of the National Academy of Sciences*, 109(32):13088–13093, 2012.

[54] Jae-Hyung Jeon, Natascha Leijnse, Lene B Oddershede, and Ralf Metzler. Anomalous diffusion and power-law relaxation of the time averaged mean squared displacement in worm-like micellar solutions. *New Journal of Physics*, 15(4):045011, apr 2013.

[55] Andreas Kaiser, Anton Peshkov, Andrey Sokolov, Borge ten Hagen, Hartmut Löwen, and Igor S. Aranson. Transport powered by bacterial turbulence. *Phys. Rev. Lett.*, 112:158101, Apr 2014.

[56] Kyogo Kawaguchi, Ryoichiro Kageyama, and Masaki Sano. Topological defects

control collective dynamics in neural progenitor cell cultures. *Nature*, 545:327, April 2017.

[57] PA Kelly. Mechanics lecture notes: An introduction to solid mechanics. Available from http://homepages.engineering.auckland.ac.nz/~pkel015/SolidMechanicsBooks/index.html, 2020.

[58] Donald L. Koch and Ganesh Subramanian. Collective hydrodynamics of swimming microorganisms: Living fluids. *Annual Review of Fluid Mechanics*, 43(1):637–659, 2011.

[59] Anna Koza, Paul D. Hallett, Christina D. Moon, and Andrew J. Spiers. Characterization of a novel air–liquid interface biofilm of pseudomonas fluorescens sbw25. *Microbiology*, 155(5):1397–1406, 2009.

[60] Nitin Kumar, Rui Zhang, Juan J. de Pablo, and Margaret L. Gardel. Tunable structure and dynamics of active liquid crystals. *Science Advances*, 4(10), 2018.

[61] C. Lapointe, N. Cappallo, D. H. Reich, and R. L. Leheny. Static and dynamic properties of magnetic nanowires in nematic fluids (invited). *Journal of Applied Physics*, 97(10):10Q304, 2005.

[62] C. Lapointe, A. Hultgren, D. M. Silevitch, E. J. Felton, D. H. Reich, and R. L. Leheny. Elastic torque and the levitation of metal wires by a nematic liquid crystal. *Science*, 303(5658):652–655, 2004.

[63] Ronald G. Larson. *The Structure and Rheology of Complex Fluids*. Oxford University Press, 1999.

[64] Eric Lauga and Thomas R Powers. The hydrodynamics of swimming microorganisms. *Reports on Progress in Physics*, 72(9):096601, aug 2009.

[65] D.C. Lay. *Linear Algebra and Its Applications*. Addison Wesley world student edition. Addison-Wesley, 2003.

[66] Myung Han Lee, Clayton P. Lapointe, Daniel H. Reich, Kathleen J. Stebe, and Robert L. Leheny. Interfacial hydrodynamic drag on nanowires embedded in thin oil films and protein layers. *Langmuir*, 25(14):7976–7982, July 2009.

[67] Myung Han Lee, Clayton P. Lapointe, Daniel H. Reich, Kathleen J. Stebe, and Robert L. Leheny. Interfacial hydrodynamic drag on nanowires embedded in thin oil films and protein layers. *Langmuir*, 25(14):7976–7982, 2009.

[68] Linnea M. Lemma, Stephen J. DeCamp, Zhihong You, Luca Giomi, and Zvonimir Dogic. Statistical properties of autonomous flows in 2d active nematics. *Soft Matter*, 15:3264–3272, 2019.

[69] Linnea M. Lemma, Michael M. Norton, Stephen J. DeCamp, S. Ali Aghvami, Seth Fraden, Michael F. Hagan, and Zvonimir Dogic. Multiscale dynamics in active nematics, 2020.

[70] Alex J. Levine, T. B. Liverpool, and F. C. MacKintosh. Dynamics of rigid

and flexible extended bodies in viscous films and membranes. *Phys. Rev. Lett.*, 93:038102, Jul 2004.

[71] Alex J. Levine, T. B. Liverpool, and F. C. MacKintosh. Dynamics of rigid and flexible extended bodies in viscous films and membranes. *Phys. Rev. Lett.*, 93:038102, Jul 2004.

[72] Alex J. Levine and T. C. Lubensky. One- and two-particle microrheology. *Phys. Rev. Lett.*, 85:1774–1777, Aug 2000.

[73] He Li, Xia-qing Shi, Mingji Huang, Xiao Chen, Minfeng Xiao, Chenli Liu, Hugues Chaté, and H. P. Zhang. Data-driven quantitative modeling of bacterial active nematics. *Proceedings of the National Academy of Sciences*, 116(3):777–785, 2019.

[74] Oliver Lieleg, Marina Caldara, Regina Baumgärtel, and Katharina Ribbeck. Mechanical robustness of pseudomonasaeruginosa biofilms. *Soft Matter*, 7:3307–3314, 2011.

[75] Bruce E. Logan. Exoelectrogenic bacteria that power microbial fuel cells. *Nature Reviews Microbiology*, 7(5):375–381, May 2009.

[76] Héctor Matías López, Jérémie Gachelin, Carine Douarche, Harold Auradou, and Eric Clément. Turning bacteria suspensions into superfluids. *Phys. Rev. Lett.*, 115:028301, Jul 2015.

[77] F.C. MacKintosh and C.F. Schmidt. Microrheology. *Current Opinion in Colloid Interface Science*, 4(4):300 – 307, 1999.

[78] Claudio Maggi, Matteo Paoluzzi, Luca Angelani, and Roberto Di Leonardo. Memory-less response and violation of the fluctuation-dissipation theorem in colloids suspended in an active bath. *Scientific Reports*, 7(1):17588, December 2017.

[79] Claudio Maggi, Matteo Paoluzzi, Nicola Pellicciotta, Alessia Lepore, Luca Angelani, and Roberto Di Leonardo. Generalized energy equipartition in harmonic oscillators driven by active baths. *Phys. Rev. Lett.*, 113:238303, Dec 2014.

[80] M. C. Marchetti, J. F. Joanny, S. Ramaswamy, T. B. Liverpool, J. Prost, Madan Rao, and R. Aditi Simha. Hydrodynamics of soft active matter. *Rev. Mod. Phys.*, 85:1143–1189, Jul 2013.

[81] M. C. Marchetti, J. F. Joanny, S. Ramaswamy, T. B. Liverpool, J. Prost, Madan Rao, and R. Aditi Simha. Hydrodynamics of soft active matter. *Rev. Mod. Phys.*, 85:1143–1189, Jul 2013.

[82] D. Marenduzzo, E. Orlandini, M. E. Cates, and J. M. Yeomans. Steady-state hydrodynamic instabilities of active liquid crystals: Hybrid lattice boltzmann simulations. *Phys. Rev. E*, 76:031921, Sep 2007.

[83] Berta Martníez-Prat, Jordi Ignés-Mullol, Jaume Casademunt, and Francesc

Sagués. Selection mechanism at the onset of active turbulence. *Nature Physics*, 15:362–366, 2019.

[84] T. G. Mason, K. Ganesan, J. H. van Zanten, D. Wirtz, and S. C. Kuo. Particle tracking microrheology of complex fluids. *Phys. Rev. Lett.*, 79:3282–3285, Oct 1997.

[85] Xavier Michalet. Mean square displacement analysis of single-particle trajectories with localization error: Brownian motion in an isotropic medium. *Phys. Rev. E*, 82:041914, Oct 2010.

[86] Vijay Narayan, Sriram Ramaswamy, and Narayanan Menon. Long-lived giant number fluctuations in a swarming granular nematic. *Science*, 317(5834):105–108, 2007.

[87] Vijay Narayan, Sriram Ramaswamy, and Narayanan Menon. Long-lived giant number fluctuations in a swarming granular nematic. *Science*, 317(5834):105–108, 2007.

[88] Daniel Needleman and Zvonimir Dogic. Active matter at the interface between materials science and cell biology. *Nature Reviews Materials*, 2(9):17048, 2017.

[89] Daniel Needleman and Zvonimir Dogic. Active matter at the interface between materials science and cell biology. *Nature Reviews Materials*, 2(9):17048, July 2017.

[90] NiepaSciRep2017. Films of bacteria at interfaces (fbi): Remodeling of fluid interfaces by pseudomonas aeruginosa. *Scientific Reports*, 7(1):17864, December 2017.

[91] Daiki Nishiguchi, Ken H. Nagai, Hugues Chaté, and Masaki Sano. Long-range nematic order and anomalous fluctuations in suspensions of swimming filamentous bacteria. *Phys. Rev. E*, 95:020601, Feb 2017.

[92] Akiyoshi Ohashi and Hideki Harada. A novel concept for evaluation of biofilm adhesion strength by applying tensile force and shear force. *Water Science and Technology*, 34(5-6):201–211, 09 1996.

[93] Marzhana Omarova, Lauren T. Swientoniewski, Igor Kevin Mkam Tsengam, Diane A. Blake, Vijay John, Alon McCormick, Geoffrey D. Bothun, Srinivasa R. Raghavan, and Arijit Bose. Biofilm formation by hydrocarbon-degrading marine bacteria and its effects on oil dispersion. *ACS Sustainable Chem. Eng.*, 7(17):14490–14499, September 2019.

[94] Achini Opathalage, Michael M. Norton, Michael P. N. Juniper, Blake Langeslay, S. Ali Aghvami, Seth Fraden, and Zvonimir Dogic. Self-organized dynamics and the transition to turbulence of confined active nematics. *Proceedings of the National Academy of Sciences*, 116(11):4788–4797, 2019.

[95] A. Ortega and J. Garcıa de la Torre. Hydrodynamic properties of rodlike

and disklike particles in dilute solution. *The Journal of Chemical Physics*, 119(18):9914–9919, 2003.

[96] Benjamin Outram. *Liquid Crystals*. 2053-2563. IOP Publishing, 2018.

[97] Jérémie Palacci, Cécile Cottin-Bizonne, Christophe Ybert, and Lydéric Bocquet. Sedimentation and effective temperature of active colloidal suspensions. *Phys. Rev. Lett.*, 105:088304, Aug 2010.

[98] Alison E. Patteson, Arvind Gopinath, Prashant K. Purohit, and Paulo E. Arratia. Particle diffusion in active fluids is non-monotonic in size. *Soft Matter*, 12:2365–2372, 2016.

[99] Walter F. Paxton, Kevin C. Kistler, Christine C. Olmeda, Ayusman Sen, Sarah K. St. Angelo, Yanyan Cao, Thomas E. Mallouk, Paul E. Lammert, and Vincent H. Crespi. Catalytic nanomotors: autonomous movement of striped nanorods. *Journal of the American Chemical Society*, 126(41):13424–13431, 2004. PMID: 15479099.

[100] Yi Peng, Lipeng Lai, Yi-Shu Tai, Kechun Zhang, Xinliang Xu, and Xiang Cheng. Diffusion of ellipsoids in bacterial suspensions. *Phys. Rev. Lett.*, 116:068303, Feb 2016.

[101] Brandon W. Peterson, Yan He, Yijin Ren, Aidan Zerdoum, Matthew R. Libera, Prashant K. Sharma, Arie-Jan van Winkelhoff, Danielle Neut, Paul Stoodley,

Henny C. van der Mei, and Henk J. Busscher. Viscoelasticity of biofilms and their recalcitrance to mechanical and chemical challenges. *FEMS Microbiology Reviews*, 39(2):234–245, 02 2015.

[102] Emmanuel L. C. VI M. Plan, Julia M. Yeomans, and Amin Doostmohammadi. Active matter in a viscoelastic environment. *Phys. Rev. Fluids*, 5:023102, Feb 2020.

[103] Lingjuan Qi and Gordon F. Christopher. Role of flagella, type iv pili, biosurfactants, and extracellular polymeric substance polysaccharides on the formation of pellicles by pseudomonas aeruginosa. *Langmuir*, 35(15):5294–5304, April 2019.

[104] S Ramaswamy, R. Aditi Simha, and J Toner. Active nematics on a substrate: Giant number fluctuations and long-time tails. *Europhysics Letters (EPL)*, 62(2):196–202, apr 2003.

[105] Sriram Ramaswamy. The mechanics and statistics of active matter. *Annual Review of Condensed Matter Physics*, 1(1):323–345, 2010.

[106] Sriram Ramaswamy. The mechanics and statistics of active matter. *Annual Review of Condensed Matter Physics*, 1(1):323–345, 2010.

[107] Sriram Ramaswamy. The mechanics and statistics of active matter. *Annual Review of Condensed Matter Physics*, 1(1):323–345, 2010.

[108] A. R. Rice, M. A. Hamilton, and A. K. Camper. Movement, replication, and emigration rates of individual bacteria in a biofilm. *Microbial Ecology*, 45(2):163–172, February 2003.

[109] David P. Rivas, Tyler N. Shendruk, Robert R. Henry, Daniel H. Reich, and Robert L. Leheny. Driven topological transitions in active nematic films. *Soft Matter*, 16:9331–9338, 2020.

[110] J. Rovner and Daniel L. Leheny. *The Static and Dynamic Properties of Colloidal Inclusions in Nematic Liquid Crystals*. PhD thesis, The Johns Hopkins University, 2013.

[111] Joel B. Rovner, Dan S. Borgnia, Daniel H. Reich, and Robert L. Leheny. Elastic and hydrodynamic torques on a colloidal disk within a nematic liquid crystal. *PRE*, 86(4):041702, October 2012.

[112] Joel B. Rovner, Clayton P. Lapointe, Daniel H. Reich, and Robert L. Leheny. Anisotropic stokes drag and dynamic lift on cylindrical colloids in a nematic liquid crystal. *Phys. Rev. Lett.*, 105:228301, Nov 2010.

[113] P.A. Rühs, L. Böcker, R.F. Inglis, and P. Fischer. Studying bacterial hydrophobicity and biofilm formation at liquid–liquid interfaces through interfacial rheology and pendant drop tensiometry. *Colloids and Surfaces B: Biointerfaces*, 117:174 – 184, 2014.

[114] Patrick A. Rühs, Lukas Böni, Gerald G. Fuller, R. Fredrik Inglis, and Peter Fischer. In-situ quantification of the interfacial rheological response of bacterial biofilms to environmental stimuli. *PLOS ONE*, 8(11):1–9, 11 2013.

[115] P G Saffman and M Delbrück. Brownian motion in biological membranes. *Proceedings of the National Academy of Sciences*, 72(8):3111–3113, 1975.

[116] David Saintillan. Rheology of active fluids. *Annual Review of Fluid Mechanics*, 50(1):563–592, 2018.

[117] Tim Sanchez, Daniel T. N. Chen, Stephen J. DeCamp, Michael Heymann, and Zvonimir Dogic. Spontaneous motion in hierarchically assembled active matter. *Nature*, 491(7424):431–434, 2012.

[118] Thierry Savin and Patrick S. Doyle. Static and dynamic errors in particle tracking microrheology. *Biophysical Journal*, 88(1):623 – 638, 2005.

[119] Thuan Beng Saw, Amin Doostmohammadi, Vincent Nier, Leyla Kocgozlu, Sumesh Thampi, Yusuke Toyama, Philippe Marcq, Chwee Teck Lim, Julia M. Yeomans, and Benoit Ladoux. Topological defects in epithelia govern cell death and extrusion. *Nature*, 544(7649):212–216, 2017.

[120] Christian Scholz, Michael Engel, and Thorsten Pöschel. Rotating robots move collectively and self-organize. *Nature Communications*, 9(1):931, 2018.

[121] Suraj Shankar, Sriram Ramaswamy, M. Cristina Marchetti, and Mark J. Bowick. Defect unbinding in active nematics. *Phys. Rev. Lett.*, 121:108002, Sep 2018.

[122] T. Shaw, M. Winston, C. J. Rupp, I. Klapper, and P. Stoodley. Commonality of elastic relaxation times in biofilms. *Phys. Rev. Lett.*, 93:098102, Aug 2004.

[123] T. Shaw, M. Winston, C. J. Rupp, I. Klapper, and P. Stoodley. Commonality of elastic relaxation times in biofilms. *Phys. Rev. Lett.*, 93:098102, Aug 2004.

[124] Tyler N. Shendruk, Kristian Thijssen, Julia M. Yeomans, and Amin Doostmohammadi. Twist-induced crossover from two-dimensional to three-dimensional turbulence in active nematics. *Phys. Rev. E*, 98:010601, Jul 2018.

[125] R. Aditi Simha and Sriram Ramaswamy. Hydrodynamic fluctuations and instabilities in ordered suspensions of self-propelled particles. *Phys. Rev. Lett.*, 89:058101, 2002.

[126] Manuel Simões, Lúcia C. Simões, and Maria J. Vieira. A review of current and emergent biofilm control strategies. *LWT - Food Science and Technology*, 43(4):573 – 583, 2010.

[127] Andrey Sokolov, Mario M. Apodaca, Bartosz A. Grzybowski, and Igor S. Aranson. Swimming bacteria power microscopic gears. *Proceedings of the National Academy of Sciences*, 107(3):969–974, 2010.

[128] Andrey Sokolov and Igor S. Aranson. Reduction of viscosity in suspension of swimming bacteria. *Phys. Rev. Lett.*, 103:148101, Sep 2009.

[129] Andrey Sokolov and Igor S. Aranson. Physical properties of collective motion in suspensions of bacteria. *Phys. Rev. Lett.*, 109:248109, Dec 2012.

[130] Andrey Sokolov, Igor S. Aranson, John O. Kessler, and Raymond E. Goldstein. Concentration dependence of the collective dynamics of swimming bacteria. *Phys. Rev. Lett.*, 98:158102, Apr 2007.

[131] Andrey Sokolov, Ali Mozaffari, Rui Zhang, Juan J. de Pablo, and Alexey Snezhko. Emergence of radial tree of bend stripes in active nematics. *Phys. Rev. X*, 9:031014, Jul 2019.

[132] Anton Souslov, Benjamin C. van Zuiden, Denis Bartolo, and Vincenzo Vitelli. Topological sound in active-liquid metamaterials. *Nature Physics*, 13:1091 – 1094, 2017.

[133] Todd M. Squires and Thomas G. Mason. Fluid mechanics of microrheology. *Annual Review of Fluid Mechanics*, 42(1):413–438, 2010.

[134] P. Stoodley, R. Cargo, C. J. Rupp, S. Wilson, and I. Klapper. Biofilm material properties as related to shear-induced deformation and detachment phenomena. *Journal of Industrial Microbiology and Biotechnology*, 29(6):361–367, December 2002.

[135] Paul Stoodley, Zbigniew Lewandowski, John D. Boyle, and Hilary M. Lappin-Scott. Structural deformation of bacterial biofilms caused by short-term fluctuations in fluid shear: An in situ investigation of biofilm rheology. *Biotechnology and Bioengineering*, 65(1):83–92, 1999.

[136] S. C. Takatori and J. F. Brady. Towards a thermodynamics of active matter. *Phys. Rev. E*, 91:032117, Mar 2015.

[137] Sho C. Takatori, Raf De Dier, Jan Vermant, and John F. Brady. Acoustic trapping of active matter. *Nature Communications*, 7(1):10694, March 2016.

[138] Amanda J. Tan, Eric Roberts, Spencer A. Smith, Ulyses Alvarado Olvera, Jorge Arteaga, Sam Fortini, Kevin A. Mitchell, and Linda S. Hirst. Topological chaos in active nematics. *Nature Physics*, 15(10):1033–1039, 2019.

[139] Monica Tanase, Laura Ann Bauer, Anne Hultgren, Daniel M. Silevitch, Li Sun, Daniel H. Reich, Peter C. Searson, and Gerald J. Meyer. Magnetic alignment of fluorescent nanowires. *Nano Lett.*, 1(3):155–158, March 2001.

[140] Xingzhou Tang and Jonathan V. Selinger. Orientation of topological defects in 2d nematic liquid crystals. *Soft Matter*, 13:5481–5490, 2017.

[141] Sumesh P. Thampi, Ramin Golestanian, and Julia M. Yeomans. Velocity correlations in an active nematic. *Phys. Rev. Lett.*, 111:118101, Sep 2013.

[142] Sumesh P. Thampi, Ramin Golestanian, and Julia M. Yeomans. Active nematic materials with substrate friction. *Phys. Rev. E*, 90:062307, Dec 2014.

[143] Sumesh P. Thampi, Ramin Golestanian, and Julia M. Yeomans. Vorticity, defects and correlations in active turbulence. *Philosophical Transactions of the Royal Society A: Mathematical, Physical and Engineering Sciences*, 372(2029):20130366, 2014.

[144] Sumesh P. Thampi, Ramin Golestanian, and Julia M. Yeomans. Vorticity, defects and correlations in active turbulence. *Philosophical Transactions of the Royal Society A: Mathematical, Physical and Engineering Sciences*, 372(2029):20130366, 2014.

[145] W. Thielicke and E. J. Stamhuis. Pivlab - time-resolved digital particle image velocimetry tool for matlab (version: 2.00), 2014.

[146] M. Mercedes Tirado, Carmen López Martínez, and José García de la Torre. Comparison of theories for the translational and rotational diffusion coefficients of rod-like macromolecules. application to short dna fragments. *The Journal of Chemical Physics*, 81(4):2047–2052, 1984.

[147] Maria M. Tirado and José García de la Torre. Translational friction coefficients of rigid, symmetric top macromolecules. application to circular cylinders. *The Journal of Chemical Physics*, 71(6):2581–2587, 1979.

[148] Brett W Towler, Cory J Rupp, AL B Cunningham, and Paul Stoodley. Viscoelastic properties of a mixed culture biofilm from rheometer creep analysis. *Biofouling*, 19(5):279–285, 2003. PMID: 14650082.

[149] Miguel Trejo, Carine Douarche, Virginie Bailleux, Christophe Poulard, Sandrine Mariot, Christophe Regeard, and Eric Raspaud. Elasticity and wrinkled morphology of bacillus subtilis pellicles. *Proceedings of the National Academy of Sciences*, 110(6):2011–2016, 2013.

[150] Liana Vaccari, Daniel B. Allan, Nima Sharifi-Mood, Aayush R. Singh, Robert L. Leheny, and Kathleen J. Stebe. Films of bacteria at interfaces: three stages of behaviour. *Soft Matter*, 11:6062–6074, 2015.

[151] Liana Vaccari, Mehdi Molaei, Tagbo H.R. Niepa, Daeyeon Lee, Robert L. Leheny, and Kathleen J. Stebe. Films of bacteria at interfaces. *Advances in Colloid and Interface Science*, 247:561 – 572, 2017. Dominique Langevin Festschrift: Four Decades Opening Gates in Colloid and Interface Science.

[152] Richard M. Venable, Helgi I. Ingólfsson, Michael G. Lerner, B. Scott Perrin, Brian A. Camley, Siewert J. Marrink, Frank L. H. Brown, and Richard W. Pastor. Lipid and peptide diffusion in bilayers: The saffman–delbrück model and periodic boundary conditions. *The Journal of Physical Chemistry B*, 121(15):3443–3457, 2017. PMID: 27966982.

[153] Tamás Vicsek, András Czirók, Eshel Ben-Jacob, Inon Cohen, and Ofer Shochet.

Novel type of phase transition in a system of self-driven particles. *Phys. Rev. Lett.*, 75:1226–1229, Aug 1995.

[154] Gaszton Vizsnyiczai, Giacomo Frangipane, Claudio Maggi, Filippo Saglimbeni, Silvio Bianchi, and Roberto Di Leonardo. Light controlled 3d micromotors powered by bacteria. *Nature Communications*, 8(1):15974, 2017.

[155] Arthur J. Vromans and Luca Giomi. Orientational properties of nematic disclinations. *Soft Matter*, 12:6490–6495, 2016.

[156] Arthur J. Vromans and Luca Giomi. Orientational properties of nematic disclinations. *Soft Matter*, 12:6490–6495, 2016.

[157] T A Waigh. Microrheology of complex fluids. *Reports on Progress in Physics*, 68(3):685–742, feb 2005.

[158] Stephanie C. Weber, Andrew J. Spakowitz, and Julie A. Theriot. Bacterial chromosomal loci move subdiffusively through a viscoelastic cytoplasm. *Phys. Rev. Lett.*, 104:238102, Jun 2010.

[159] James N. Wilking, Thomas E. Angelini, Agnese Seminara, Michael P. Brenner, and David A. Weitz. Biofilms as complex fluids. *MRS Bulletin*, 36(5):385–391, 2011.

[160] L. G. Wilson, V. A. Martinez, J. Schwarz-Linek, J. Tailleur, G. Bryant, P. N.

Pusey, and W. C. K. Poon. Differential dynamic microscopy of bacterial motility. *Phys. Rev. Lett.*, 106:018101, Jan 2011.

[161] Hugo Wioland, Francis G. Woodhouse, Jörn Dunkel, John O. Kessler, and Raymond E. Goldstein. Confinement stabilizes a bacterial suspension into a spiral vortex. *PRL*, 110(26):268102, June 2013.

[162] Cynthia Wu, Ji Youn Lim, Gerald G. Fuller, and Lynette Cegelski. Disruption of escherichia coli amyloid-integrated biofilm formation at the air-liquid interface by a polysorbate surfactant. *Langmuir*, 29(3):920–926, January 2013.

[163] Cynthia Wu, Ji Youn Lim, Gerald G. Fuller, and Lynette Cegelski. Quantitative analysis of amyloid-integrated biofilms formed by uropathogenic escherichia coli at the air-liquid interface. *Biophysical Journal*, 103(3):464 – 471, 2012.

[164] Yusuf Ilker Yaman, Esin Demir, Roman Vetter, and Askin Kocabas. Emergence of active nematics in chaining bacterial biofilms. *Nature Communications*, 10(1):2285, 2019.

[165] Ou Yang, Yi Peng, Zhengyang Liu, Chao Tang, Xinliang Xu, and Xiang Cheng. Dynamics of ellipsoidal tracers in swimming algal suspensions. *Phys. Rev. E*, 94:042601, Oct 2016.

[166] Zhihong You, Daniel J. G. Pearce, Anupam Sengupta, and Luca Giomi. Geom-

etry and mechanics of microdomains in growing bacterial colonies. *Phys. Rev. X*, 8:031065, Sep 2018.

[167] Rui Zhang, Nitin Kumar, Jennifer L. Ross, Margaret L. Gardel, and Juan J. de Pablo. Interplay of structure, elasticity, and dynamics in actin-based nematic materials. *Proceedings of the National Academy of Sciences*, 115(2):E124–E133, 2018.

[168] Étienne Fodor and M. Cristina Marchetti. The statistical physics of active matter: From self-catalytic colloids to living cells. *Physica A: Statistical Mechanics and its Applications*, 504:106 – 120, 2018. Lecture Notes of the 14th International Summer School on Fundamental Problems in Statistical Physics.

Vita

David Rivas received his BS degree in physics from the University of Maryland, Baltimore County (UMBC) in 2014. During his time as an undergraduate, he worked on modeling deceleration of jets in active galactic nuclei under the supervision of Dr. Markos Georganopolous. He then attended Johns Hopkins university as a PhD student where he discovered a keen interest in soft condensed matter, particularly active matter, which was the focus of his thesis research under the supervision of Dr. Robert Leheny.